ΕΘΝΙΚΟ ΜΕΤΣΟΒΙΟ ΠΟΛΥΤΕΧΝΕΙΟ

ΣΧΟΛΗ ΕΦΑΡΜΟΣΜΕΝΩΝ ΜΑΘΗΜΑΤΙΚΩΝ ΚΑΙ ΦΥΣΙΚΩΝ ΕΠΙΣΤΗΜΩΝ

ΔΙΠΛΩΜΑΤΙΚΗ ΕΡΓΑΣΙΑ

Μελέτη Προσομοίωσης Δέσμης Ηλεκτρονίων για Ακτινοθεραπεία Φαινομένου FLASH

ΜΕΛΙΝΑ ΜΟΝΙΑΚΗ

ΕΠΙΒΛΕΠΩΝ:

Ε. Ν. ΓΑΖΗΣ, ΟΜΟΤΙΜΟΣ ΚΑΘΗΓΗΤΗΣ Ε.Μ.Π.

ΑΘΗΝΑ, ΣΕΠΤΕΜΒΡΙΟΣ 2023

ΕΘΝΙΚΟ ΜΕΤΣΟΒΙΟ ΠΟΛΥΤΕΧΝΕΙΟ

ΣΧΟΛΗ ΕΦΑΡΜΟΣΜΕΝΩΝ ΜΑΘΗΜΑΤΙΚΩΝ ΚΑΙ ΦΥΣΙΚΩΝ ΕΠΙΣΤΗΜΩΝ

ΔΙΠΛΩΜΑΤΙΚΗ ΕΡΓΑΣΙΑ

Μελέτη Προσομοίωσης Δέσμης Ηλεκτρονίων για Ακτινοθεραπεία Φαινομένου FLASH

ΜΕΛΙΝΑ ΜΟΝΙΑΚΗ

ΕΠΙΒΛΕΠΩΝ:

Ε. Ν. ΓΑΖΗΣ, ΟΜΟΤΙΜΟΣ ΚΑΘΗΓΗΤΗΣ Ε.Μ.Π.

ΤΡΙΜΕΛΗΣ ΕΠΙΤΡΟΠΗ

Ε. Ν. ΓΑΖΗΣ, ΟΜΟΤΙΜΟΣ ΚΑΘΗΓΗΤΗΣ Ε.Μ.Π.

Θ. ΑΛΕΞΟΠΟΥΛΟΣ, ΚΑΘΗΓΗΤΗΣ Ε.Μ.Π.

Α. ΓΕΩΡΓΑΚΙΛΑΣ, ΚΑΘΗΓΗΤΗΣ Ε.Μ.Π.

ΑΘΗΝΑ, ΣΕΠΤΕΜΒΡΙΟΣ 2023

NATIONAL TECHNICAL UNIVERSITY OF ATHENS

SCHOOL OF APPLIED MATHEMATICAL AND PHYSICAL SCIENCES

DIPLOMA THESIS

Simulation Study of the Electron Beam for FLASH Radiation Therapy

MELINA MONIAKI

SUPERVISOR:

Prof. Evangelos Gazis

Athens, September 2023

NATIONAL TECHNICAL UNIVERSITY OF ATHENS

SCHOOL OF APPLIED MATHEMATICAL AND PHYSICAL SCIENCES

DIPLOMA THESIS

Simulation Study of the Electron Beam for FLASH Radiation Therapy

MELINA MONIAKI

SUPERVISOR:

Prof. Evangelos Gazis

Committee:

Prof. Evangelos Gazis

Prof. Theodoros Alexopoulos

Prof. Alexandros Georgakilas

Athens, September 2023

Acknowledgements

As I conclude this thesis, I am deeply appreciative of the individuals that have been significant in its completion.

First, I would like to express my deepest gratitude to my supervisor, Prof. E. Gazis for his support, guidance and valuable insights throughout my thesis preparation. His expertise has been instrumental in shaping this study.

I also want to express my deepest gratitude to my family and friends for their love and encouragement. Your sacrifices and unwavering faith in my abilities have been the driving force behind my success.

Περίληψη

Η συνεχής αύξηση των περιστατικών του καρκίνου τα τελευταία χρόνια έχει επιφέρει την ανάγκη για προηγμένες μεθόδους θεραπείας. Η ραδιοθεραπεία αποτελεί μία από τις βασικές μεθόδους καταπολέμησης του καρκίνου, με την ραδιοθεραπεία Flash να αντιπροσωπεύει μια καινοτόμο προσέγγιση, καθώς μπορεί να προσφέρει εξαιρετικά υψηλό ρυθμό δόσης σε ελάχιστο χρόνο, που φτάνει τα αρκετά Gray ανά δευτερόλεπτο. Αυτό το χαρακτηριστικό οδηγεί στην εξουδετέρωση των καρκινικών κυττάρων, προκαλώντας ταυτόχρονα ελάχιστη βλάβη στον υγιή ιστό.

Στην παρούσα διπλωματική εργασία μελετάμε την ραδιοθεραπεία Flash δημιουργώντας έναν applicator ηλεκτρονίων με το πακέτο προσομοίωσης Fluka. Υπολογίζουμε την δόση των ηλεκτρονίων και μελετάμε τα χαρακτηριστικά της δέσμης για διαφορετικές ενέργειες ηλεκτρονίων, αλλάζοντας τα υλικά του applicator καθώς και τη γεωμετρία του.

Λέξεις Κλειδιά

Ραδιοθεραπεία, Flash RT, FLUKA, applicator ηλεκτρονίων

Abstract

The continuous increase of cancer incidents in recent years, has brought the need for advanced treatment methods. Radiotherapy is one of the main methods of fighting cancer. Flash radiotherapy represents an innovative approach to radiotherapy as it can deliver an extremely high dose rate, reaching several Grays per second. This characteristic leads to the damage of cancer cells while causing minimal damage to healthy tissue.

In this thesis we study Flash radiotherapy by creating an electron applicator with the Fluka simulation package. We calculate the dose and beam characteristics for different electron energies by changing the applicator materials and applicator geometry.

Keywords

Radiotherapy, Flash RT, FLUKA, electron applicator

Contents

APPENDIX

List of Figures

List of Tables

1. Introduction

The field of medicine faced limited options for treating various diseases, both malignant and benign, until the discovery of X-rays in 1895 by Wilhelm Conrad Röntgen. Just one year after their discovery, Emil Herman Grubbe used X-rays to treat a patient with breast cancer, even before fully understanding the physical properties and biological effects of X-rays.

In the same year, Antoine Henri Becquerel initiated the study of radioactivity and natural sources of radiation. In 1898, the discovery of radium as a potent source of radiation was discovered by Maria Sklodowsksa-Curie and her husband Pierre Curie and three years later Becquerel and Curie reported on the physiologic effects of radium rays.

By the turn of the century, an increasing number of studies began to explore the therapeutic potential of X-rays and radium in medicine. At this stage, skin cancers were the most commonly treated conditions due to the limited penetration of radiation into tissues. In the 1910s, a pivotal development occurred with the creation of a new device by Coolidge. This device emitted higher-energy X-rays, enabling the treatment of deeper-seated cancers. However, it is important to note that during this period, the knowledge about the properties and mechanisms of action of radiotherapy was limited. Consequently, the effectiveness of cancer treatment was overshadowed by significant side effects. This prompted physicians to embark on new research endeavors aimed at gaining a better understanding of these treatments.

As time progressed, researchers made important discoveries related to radioactive isotopes, various types of radiation, and radiation techniques. They began unraveling the nature of radiations, their modes of action, and the relationship between the timing and dosage of radiation in terms of cell survival. It wasn't until the 1920s that physicians comprehended the advantages of administering the total radiation dose in fractionated sessions rather than a single treatment session. This approach proved to be more effective in cancer control while minimizing side effects.

In 1928, the International Commission on Radiological Protection (ICRP) was established, marking a significant milestone in addressing radioprotection concerns.

Furthermore, in 1932, the introduction of an ionizing chamber enabled physicians to measure radiation doses more accurately, specifically the first dose unit known as the Röntgen unit.

From the 1930s to the 1950s, scientific progress in treating deep-seated cancers continued to advance. This period, often referred to as the Orthovoltage era, saw the utilization of radium-based interstitial irradiation (brachytherapy) and the development of supervoltage X-ray tubes, capable of delivering energies ranging from 50 kV to 200 kV. Brachytherapy allowed operators to treat tumors without an external beam source, reducing the impact on surrounding healthy tissue. Additionally, this era marked the introduction of electron beam therapy, providing a valuable option for delivering higher and variable energies to address deeper tumors.

The following three decades, known as the Megavoltage era, were characterized by ongoing efforts to develop more innovative radiotherapeutic devices for treating cancers deep within tissues. Innovations included the introduction of Cobalt teletherapy, which produced high-energy γ-rays, and more potent electron linear accelerators (electron linacs) that delivered megavoltage X-rays. These advancements allowed for the administration of higher doses of energy, facilitating the treatment of deeper tumors with greater skin sparing. To manage these radiation sources and minimize the risk of excessive radiation in surrounding tissues, innovative multi-field plans of irradiation were designed. During this period, radiotherapy emerged as a recognized medical discipline, leading to the establishment of the first radiologist associations. As evidence continued to accumulate, confirming the efficacy of radiation therapy in improving the survival of patients with various types of cancers, innovative devices with computerized controls were introduced to medical practice.

However, a new era in the history of radiation therapy began to unfold in the 1970s and 1980s, marked by the introduction of innovative devices capable of delivering proton beams. Although the first clinical use of proton beams dated back to 1954, it was not until the late 1970s that computer-assisted accelerators for protons were successfully applied to treat a wide range of tumors. The key advantage of using ion beams was their precise controllability, making them a superior tool for cancer therapy and the treatment of challenging benign diseases.

Another significant milestone in radiotherapy was reached by the end of the 1990s with the introduction of more sophisticated computers, which enabled the development of 3D conformal radiotherapy devices (Stereotactic radiation therapy). These devices enhanced the efficacy and safety of treatments, particularly for patients. As the new millennium began, Stereotactic radiation therapy gained prominence, especially for the treatment of metastatic tumors. Additionally, adaptive radiotherapy (ART) emerged as a special form of image-guided radiotherapy (IGRT), allowing for treatment technique replanning and optimization during the course of radiotherapy when clinically relevant. [1]

2. Tumor Radiotherapy

Radiation is a physical agent, which is used to destroy cancer cells. The radiation used is called ionizing radiation because it forms electrically charged particles (ions) and transfers energy to the cells of the tissues it passes through. This energy deposition has the potential to either kill cancer cells or induce genetic changes resulting in cancer cell death.

High-energy radiation damages the genetic material (DNA) of cells, inhibiting their ability to divide and proliferate. While radiation affects both normal and cancer cells, the goal of radiation therapy is to maximize the radiation dose to cancer cells while minimizing exposure to adjacent normal cells or those in the radiation's path. Normal cells possess a higher capacity for self-repair and maintaining their normal function compared to cancer cells. Cancer cells, on the other hand, are less efficient in repairing radiation-induced damage, resulting in differential cancer cell killing.

There are two methods employed to administer radiation to the cancer site. The first method is external beam radiation, where high-energy rays (photons, protons, or particle radiation) are directed towards the tumor location from outside the body. This approach is widely used in clinical practice.

The second method is internal radiation or brachytherapy, which involves delivering radiation from radioactive sources placed inside the body.

2.1 Photon radiation (x-rays and gamma rays)

The discover of X-rays was made in 1895 by W. C. Roentgen. This discovery opened the door to using radiation for treating diseases like cancer. The evolution of radiation therapy can be traced through significant milestones, such as the treatment of skin cancer by T. Stenbeck and T. Sjogren in 1900 and the pioneering attempt to treat leukemia by Senn in 1903. Despeignes began using radiotherapy, introducing radiotherapy for stomach cancer patients in 1896, achieving notable improvements and pain relief. The quest for accurate dosimetry emerged in 1902 when Guido Holzknecht of Austria proposed Roentgen-based dosimetry using a chromoradiometer. The subsequent introduction of ionization chambers in 1928, during the first Association of International Radiology conference in Stockholm, marked a significant step in radiation therapy dosimetry. However, early radiation therapy was characterized by low-energy X-rays with limited penetration power, lacking precise dosage concepts and tumor localization procedures. It was only in the mid-20th century that sophisticated dosimetry systems began to take shape.

The advent of Co-60 beam therapy emitting megavoltage gamma rays in the 1950s to 1960s ushered in a new era of research and development in radiation therapy. This era, often referred to as the first radiotherapy period, laid the foundation for the sophisticated dosimetry and treatment planning systems in use today. [2]

2.2 Hadron Therapy

2.2.1 Proton Beam Therapy

Proton beam therapy (PBT) is a type of radiation therapy (RT). The appropriate application of PBT has led to fewer adverse effects and higher therapeutic efficacy compared with conventional RT using X-ray beams. Protons are heavy charged particles, ~800 times the mass of electrons. The large mass and acceleration applied gives each proton a specific momentum that is mostly dissipated after traveling a defined distance, and then slowed down by interactions with the target, which causes a sharp rise in energy deposition at the end of the path of the proton, followed by no further dose delivery, which is referred to as the Bragg peak. This individual physical property provides superior dosimetric advantages over photons or electrons. Therefore, rather than traversing the target, protons are stopped at an energy-dependent depth in the target and have no exit dose, which completely spares the downstream normal tissue. Proton beams are generated by a cyclotron or synchrotron, and then accelerated to the desired target. [3]

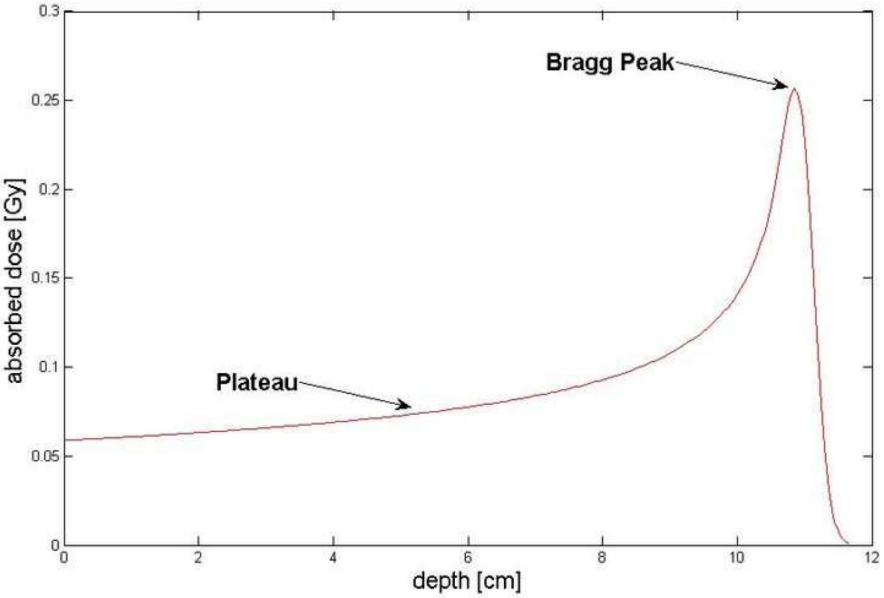

Figure 1. The Bragg curve: the absorbed dose of a monoenergetic proton pencil beam as function of the penetration depth. The dose is low in the plateau region and maximal at the end of the proton track, leading to the so-called Bragg peak. [4]

2.2.2 Carbon Ion Radiotherapy

Carbon ion radiotherapy (CIRT) has various advantages compared with X- ray radiotherapy (XRT). It has higher biological effectiveness than XRT and has already shown promising results for the treatment of resistant tumors like sarcoma, adenocarcinoma, and other.

Furthermore, because of its characteristic Bragg peak, it can deliver a localized high dose to the target while minimizing the dose delivered to organs at risk (OARs). The beam delivery technique and the distance between the target and OARs dictate the degree of complications and whether tumor control can be achieved. Therefore, it is important to establish constraints based on dose–volume histogram parameters so that treatment plans can be optimized for each patient. [5]

In addition to this, carbon ion radiotherapy offers several advantages over conventional photon-based external beam radiation, including superior dose distribution, higher linear energy transfer (LET), and a greater relative biological effectiveness (RBE). The elevated RBE is a consequence of a distinct DNA damage pattern characterized by concentrated lesions that overwhelm the DNA repair capacity of cancerous cells. These physical and radiobiological attributes equip heavy ions with potent tumor-killing capabilities while potentially minimizing damage to normal tissues. Consequently, CIRT holds promise for treating challenging tumors, such as those that are hypoxic, resistant to radiation, or deeply embedded. [6]

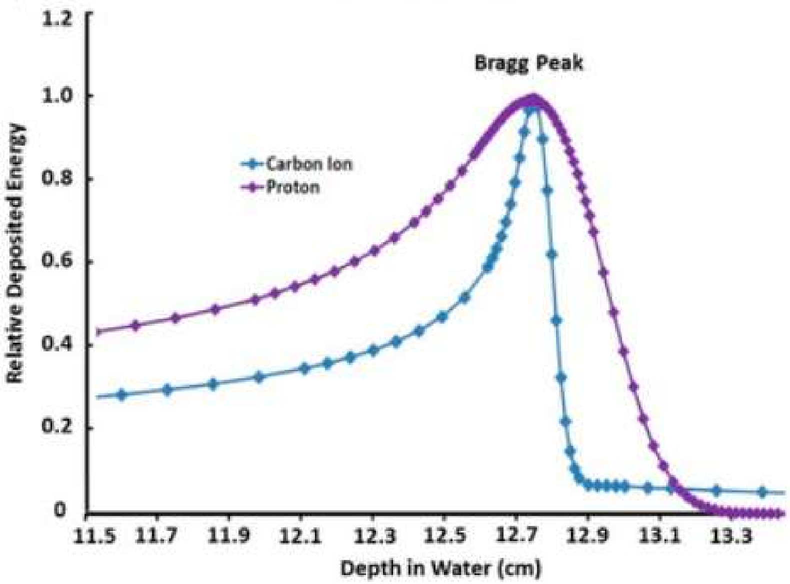

Figure 2. Percentage depth dose curves comparing carbon ion to proton beams. [6]

2.3 Electron Therapy

Electron therapy, or electron beam therapy, is a form of radiotherapy which is used to treat primarily superficial tumors. Electron beams are rapidly attenuated by soft tissue and thus can only treat to a depth of a few centimeters (typically 0-3 cm), compared to megavoltage x-rays which are much more penetrating. Suitable targets include cutaneous cancer, total skin irradiation (mycosis fungoides) and keloid scarring.

Electron therapy is performed with a medical linear accelerator by withdrawing the x-ray target from the beam path. Unlike photons, electrons are widely scattered by air before reaching the patient. This necessitates the use of 'electron applicators' which are specially designed diaphragms which collimate the electron beam at the skin surface. [7]

2.3.1 Very High Energy Electron Therapy (VHEE)

Very High Energy Electron (VHEE) radiotherapy offers promising advantages for the treatment of deep-seated tumors. The precise dose deposition capabilities of VHEE beams, with energies exceeding 50 MeV, enable effective reach into deep tumor regions, surpassing the limitations of clinical electron beams. Theoretical studies suggest that VHEEs can achieve comparable or superior target coverage while minimizing damage to critical structures, thus reducing the risk of harming healthy tissues adjacent to the tumor site. Furthermore, VHEEs exhibit enhanced resilience to tissue inhomogeneities, making them a potentially reliable treatment option in anatomically diverse regions. The optimization of focused VHEE beams addresses the challenges associated with depth-dose profiles, enabling concentrated dose delivery to a well-defined volumetric element within the body while minimizing entrance and exit doses. Magnetic focusing techniques show promise in reducing lateral scattering and improving dose deposition for VHEE beams. [8]

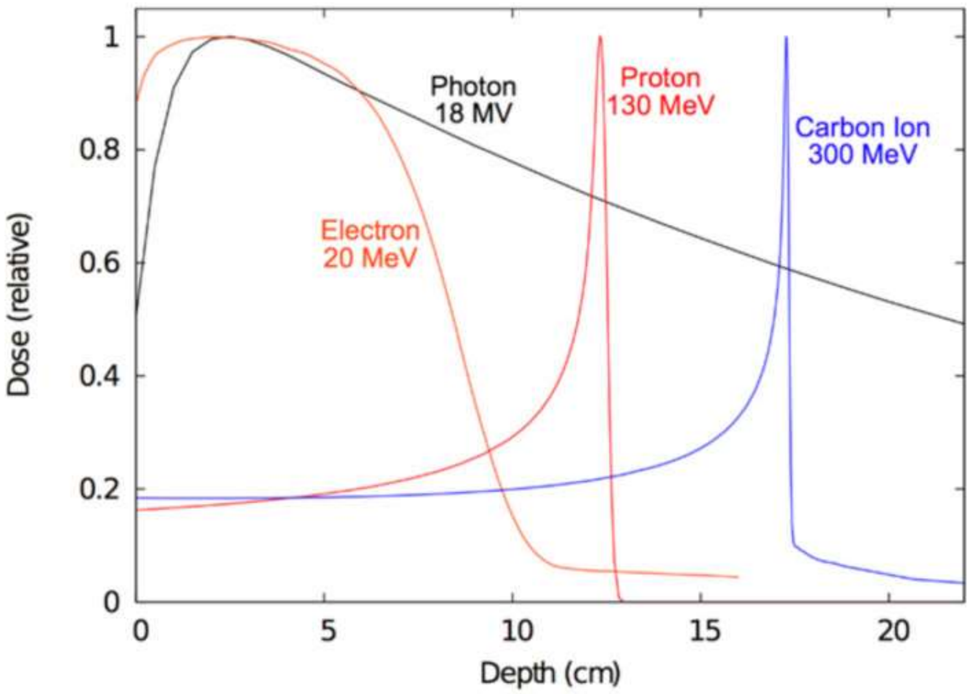

Figure 3. Depth dose curves for radiotherapy. Dose distributions as a function of depth in water shown for various clinical radiation beams. [9]

2.3.2 Flash Radiotherapy (FLASH-RT)

FLASH radiotherapy (FLASH-RT) is a promising cancer irradiation treatment, currently under investigation, which reduces the toxicity on the healthy tissues while keeping the same efficiency in the tumor cure as in conventional treatments.

In the early 1960s, some experiments demonstrated that a very-high-dose rate in ultra-short radiation pulses increased cell survival, that is, it spares healthy tissues, compared to conventional (CONV) treatments. After three decades, this phenomenon was again investigated and confirmed by Vincent Favaudon and their team. In FLASH RT, the entire dose is delivered in a very short time. The definition of the FLASH regime demands the specification of different inter-dependent temporal parameters such as pulse repetition frequency (PRF), pulse number (np), pulse width (tp), dose per pulse (Dp), in-peak dose rate ($\dot{D}p$), average dose rate ($\bar{\dot{D}}$), and the total irradiation time (ti).

Typically, the FLASH effect was observed with an irradiation time of ti < 100 ms an average dose rate $\bar{\dot{D}}$ >100 Gy/s, an in-peak dose-rate of $\dot{D}p > 10^6$, and a pulse repetition frequency PRF > 100 Hz. It must be noted that these are not threshold values, and to the best of our current knowledge, there is no well-defined limit for the instantaneous dose rate, but only an empirical demonstration that sparing normal tissue can be achieved. In addition, the FLASH electron pulse usually provides a dose > 1 Gy, which is three orders of magnitude greater than a conventional electron pulse (<1 mGy/pulse). [10]

These parameters are shown in Figure 4.

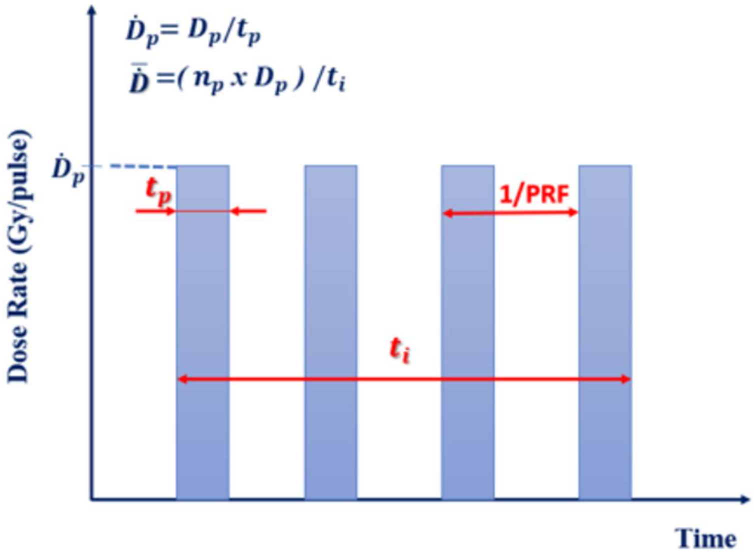

Figure 4. Typical time structure of electron beam parameters. [10]

Figure 5 presents a side-by-side comparison of temporal beam characteristics of FLASH and CONV radiation therapy. [11]

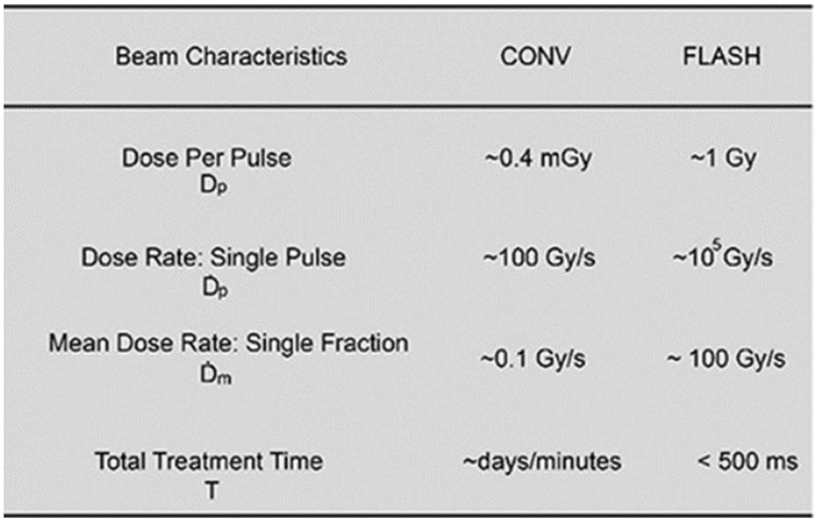

Beam Characteristics	CONV	FLASH
Dose Per Pulse D_p	~0.4 mGy	~1 Gy
Dose Rate: Single Pulse $\dot{D}_p$	~100 Gy/s	~10^5 Gy/s
Mean Dose Rate: Single Fraction $\dot{D}_m$	~0.1 Gy/s	~ 100 Gy/s
Total Treatment Time T	~days/minutes	< 500 ms

Figure 5. Typical temporal beam characteristics for conventional (CONV) and FLASH using electrons. [11]

3. Phantoms in Medical and Health physics

One of the most common methods of treating cancer is the use of external beam radiotherapy, with approximately half of all cancer patients receiving radiotherapy at some point during their course of treatment. The quality of radiation therapy treatments is checked with dose measurements in phantoms, which are defined as inanimate surrogates for a human body or anatomic region of interest with the purpose to mimic human tissue for a specific procedure or experiment. Phantoms can be divided into two categories: computational phantoms and physical phantoms. [12]

3.1 Computational Phantoms for Dose Calculations

Computational phantoms play a crucial role in assessing both internal and external radiation doses. These phantoms can represent the human body with a high level of detail regarding anatomical geometry and tissue composition. They find significant application in radiotherapy dose calculations. One of the key advantages of using these computational anthropomorphic phantoms in radiation therapy is their ability to be tailored to match the specific anatomy of individual patients, thereby enhancing the accuracy of dose calculations for particular organs or regions of interest. [12]

3.2 Physical Phantoms for Dose Measurements

In the field of radiation oncology, phantoms serve a crucial purpose in conducting diverse radiation dose measurements. These phantoms exhibit variations in their composition, shape, and intended function, depending on their specific roles. To ensure the quality of medical linear accelerators, scanning water tanks and water equivalent plastic slabs are extensively employed for quality assurance.

In the context of radiation therapy quality assurance, a range of dosimeters such as film, diodes, and ionization chambers, along with tissue substitute phantoms, are utilized to verify the accurate delivery of prescribed therapeutic doses. Furthermore, to study methods for treating moving tumors, organ motion phantoms are used to replicate periodic organ motion. This enables researchers to investigate and develop effective treatments for moving tumors. [12]

3.3 Physical Anthropomorphic Phantoms

Anthropomorphic phantoms imitate both the internal and external anatomical features of the human body. Their primary objective is to replicate the radiation interaction properties of human tissues, although they often fall short of achieving complete equivalence.

Physical anthropomorphic phantoms serve as a medium to assess radiation distributions within a human-like anatomy. These phantoms find widespread application in various areas, including the validation of novel therapeutic techniques and investigations where anatomical characteristics play a crucial role. By utilizing these phantoms, researchers can explore and study scenarios where human-like structures and features are of potential significance. [12]

3.4 Water as a Phantom Material

Water has physical and radiological properties that are very similar to those of human soft tissue. The effective atomic number of water closely approximates the effective atomic number of human tissue. The similarity ensures that the radiation interactions in water are representative of what happens in human tissue. In addition to this, water is readily available and can be easily shaped and sized while maintaining its density with a reasonable degree of accuracy and it is a cost-effective option. Moreover, water phantoms proved to be valuable for acquiring beam profiles and measuring radiation doses and they played a crucial role in the commissioning and quality assurance testing of linear accelerator machines and treatment planning systems. [13]

3.5 PMMA as phantom material

In the realm of electron radiotherapy, selecting the right phantom material is crucial for precise dose measurements and effective treatment planning. Polymethyl methacrylate (PMMA), commonly known as acrylic or Plexiglas, emerges as a promising alternative to water in specific contexts, particularly low-energy electron beam dosimetry. This section discusses the merits of PMMA as a water substitute and its preference over water in certain radiotherapy scenarios.

PMMA exhibits advantages that make it a compelling water substitute. Its density closely approximates that of water, rendering it suitable for crafting water-equivalent phantoms, a prerequisite for accurate dose measurements. Notably, PMMA demonstrates a comparable electron range to water for low-energy electron beams, particularly those under 10 MeV. This property is pivotal, given the profound influence of material electron density and stopping power on low-energy electron behavior.

Additionally, PMMA showcases the potential to mitigate electron scattering effects due to its electron density's proximity to water's. This trait is especially advantageous for accurate dose measurements in low-energy electron beam dosimetry.

Practically, PMMA offers accessibility, moldability for shaping into desired phantom geometries, and cost-effectiveness. These practical attributes enhance its suitability as a phantom material, particularly where water is not the primary choice.

Situations favoring PMMA over water include low-energy electron beam dosimetry. In contexts involving electron beams below around 10MeV, PMMA's water-equivalent properties enable accurate dose measurements comparable to water. Additionally, PMMA's moldability proves advantageous in designing phantoms with intricate geometries.

While PMMA boasts significant advantages, it's important to recognize its limitations. It might not replicate water's attributes across all energy ranges. For higher-energy electron and photon beams, water remains the reference medium due to its superior water-equivalence properties. In conclusion, PMMA presents a promising alternative to water in electron radiotherapy, especially in the low-energy spectrum. Its ability to mimic water-equivalent properties and practical versatility contributes to refining dose measurements and enhancing treatment planning precision. [14]

4. Dosimetry

Electron dosimetry stands at the forefront of modern radiation therapy, playing a pivotal role in delivering precise and targeted radiation doses to cancerous tissues while minimizing the impact on surrounding healthy organs. As a specialized field within medical physics, electron dosimetry focuses on the measurement and calculation of electron beam characteristics, enabling clinicians to design tailored treatment plans tailored to each patient's unique anatomy and tumor location. With its ability to harness the distinctive properties of electron beams, electron dosimetry has revolutionized cancer treatment, enhancing treatment efficacy, and optimizing patient outcomes.

4.1 Depth Dose Characteristics of Electron Beams

The electron beam central axis depth dose curve usually exhibits a higher surface dose compared to megavoltage photon beams. The dose increases to a maximum at a certain depth known as the electron beam depth of dose maximum (zmax). Beyond zmax, the dose decreases rapidly and levels off at a lower dose component called the bremsstrahlung tail. These characteristics provide clinical advantages over conventional X-ray modalities in treating superficial tumors.

High-energy linacs typically generate electron beams with energies from 4 to 25 MeV. Although electron beams are almost monoenergetic when they leave the accelerator, interactions with various structures (such as the accelerator exit window, scattering foils, monitor chambers, collimators, and air) cause the beam's electron energy spectrum to broaden. This leads to bremsstrahlung production, contributing to the bremsstrahlung tail in the electron beam percentage depth dose (PDD) distribution.

Upon initial contact with the patient, the clinical electron beam has an incident mean energy lower than the electron energy inside the accelerator.

The percentage depth dose (PDD) represents the ratio of the dose at a specific point on the central axis of an electron beam to the maximum dose on the central axis, multiplied by 100. This PDD value is usually measured for the nominal treatment distance, which is the distance between the accelerator exit window and the patient's skin, and it depends on field size and electron beam energy.

The maximum range Rmax is defined as the depth at which extrapolation of the tail of the central-axis depth dose curve meets the bremsstrahlung background, as shown in the next figure (Figure 6). It is the largest penetration depth of electrons in the absorbing medium. The maximum range has the drawback of not giving a well-defined measurement point.

The practical range R_p is defined as the depth at which the tangent plotted through the steepest section of the electron depth dose curve intersects with the extrapolation line of the background due to bremsstrahlung.

The depths R_{90} and R_{50} are defined as depths on the electron percentage depth dose curve at which the percentage depth doses beyond zmax attain values of 90% and 50%, respectively.

The depth Rq is defined as the depth where the tangent through the dose inflection point intersects the maximum dose level. [15]

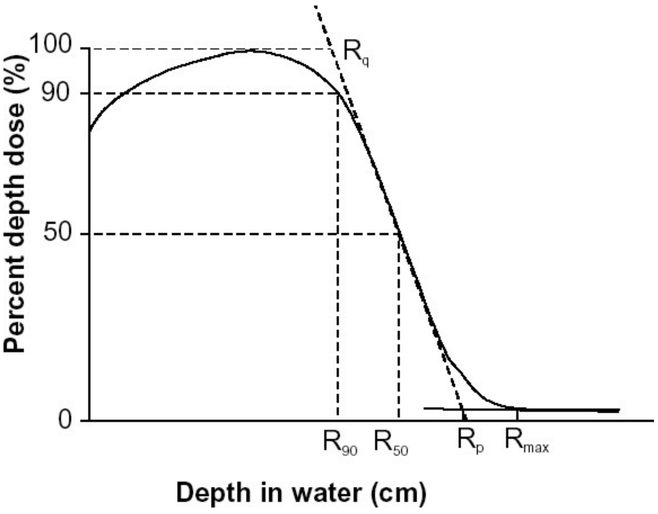

Figure 6. Typical electron beam percentage depth dose curve illustrating the definition of R_q, R_p, R_{max}, R_{50} and R_{90}. [15]

4.2 Transverse Dose Profile

In electron radiotherapy, the transverse dose profile refers to the distribution of radiation dose delivered by an electron beam in the plane perpendicular to the beam's central axis. It represents how the dose is distributed across the patient's body or treatment field at a specific depth along the beam's path.

The transverse dose profile is a crucial parameter in treatment planning, as it directly affects the coverage of the target area (tumor) and the sparing of nearby healthy tissues. Clinicians use this information to ensure that the prescribed dose is accurately delivered to the tumor while minimizing radiation exposure to critical structures.

The shape of the transverse dose profile depends on various factors, including the initial energy of the electron beam, the beam collimation, the beam scattering, and the presence of any beam modifiers. For a well-defined and uniform dose distribution, the transverse dose profile should ideally have a flat and symmetrical shape, ensuring that the target area receives the intended dose.

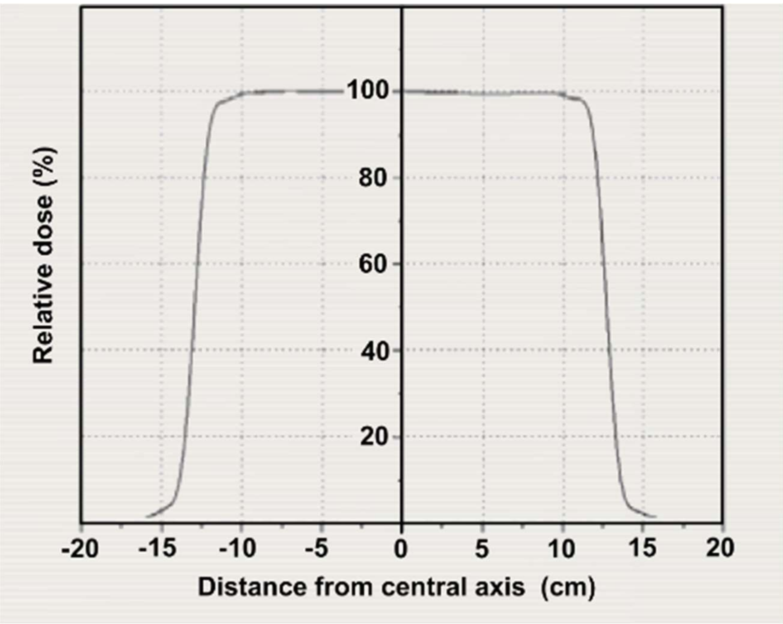

Figure 7 Dose profile measured at a depth of dose maximum zmax for an electron beam. [16]

5. Monte Carlo Simulation

Monte Carlo simulation is a type of simulation that relies on repeated random sampling and statistical analysis to compute the results. This method of simulation is very closely related to random experiments, experiments for which the specific result is not known in advance.

The Monte Carlo method is widely used in various fields, including physics, engineering, finance, computer science, and statistics. [17]

5.1 Fluka

The FLUKA code is a general-purpose Monte Carlo code for the interaction and transport of hadrons, leptons, and photons from keV (with the exception of neutrons, tracked down to thermal energies) to cosmic ray energies in any material.

It has been built with the aim of including the best physics models in terms of completeness and precision, through a microscopic approach where each step has sound physics bases. Reliability is pursued by comparing with particle production data at single interaction level. No tuning on integral data, like calorimeter resolutions, thick target yields etc., is performed. Therefore, final predictions are obtained with minimal free parameters, fixed for all energies and target/projectile combinations. Results in complex problems as well as scaling laws and properties come out naturally from the underlying physics models and the basic conservation laws are fulfilled a priori. Moreover, the microscopic approach preserves correlations within interactions and among the particle shower components, and it provides predictions where no experimental data is available. Powerful biasing techniques are built-in to allow to critically reduce computing time when needed. Transport in magnetic field is also performed.

FLUKA has a wide range of applications, spanning accelerator design and shielding, radiation protection, particle physics, dosimetry, detector simulation, hadron therapy. [18]

5.2 Flair

Flair is an advanced user-friendly interface for FLUKA to facilitate the editing of FLUKA input files, execution of the code and visualization of the output files. It is based entirely on Python and Tkinter.

Features:

- input editor front-end interface for easy and almost error-free editing as well as validation of the input file during editing
- interactive geometry editor, allowing to edit bodies and regions in a visual/graphical way with immediate debugging information.
- advanced layer mechanism for graphically displaying any information from the input file on top of the geometry:
    - lattices and voxel display 2D and 3D
    - density, biasing, thresholds, ...

    - technical drawing superposition
    - interactive USRBIN plotting and surface mapping.
    - real time 3D ray-tracing rendering, with shadows, edges, clipping and projection bodies.
    - customizable multiple palettes
- debugging, compiling, running and monitoring of the status during a run.
- back-end interface for post-processing of the output files and plot generation through an interface with gnuplot and 3D photo-realistic images.
- materials library and geometrical objects, for easier editing, storing and sharing among other users and projects.
- python API for manipulating the input files, post-processing of the results and interfacing to gnuplot.
- import/export to various formats:
    - MCNP
    - GDML
    - Povray
    - DXF
    - bitmap images

[19]

5.3 Monte Carlo Simulation for FLASH-RT

5.3.1 Description of the Applicator

The simulation geometry and beam characteristics was based on the study of Lucia Giuliano et al. (2023). [10] In the next chapters we will refer to this applicator as applicator A-1.

In the simulation, the electron beam exits from the linac and goes through a 55 µm thick titanium window that seals the linac vacuum. The source-to-surface distance (SSD) is 60 cm.

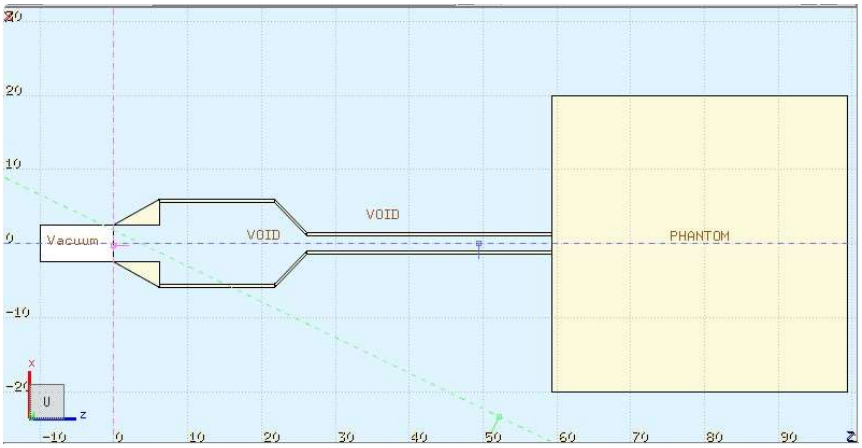

Figure 8. Two-dimensional visualization of FLUKA simulation geometry for the A-1 applicator. The beam travels in the z direction.

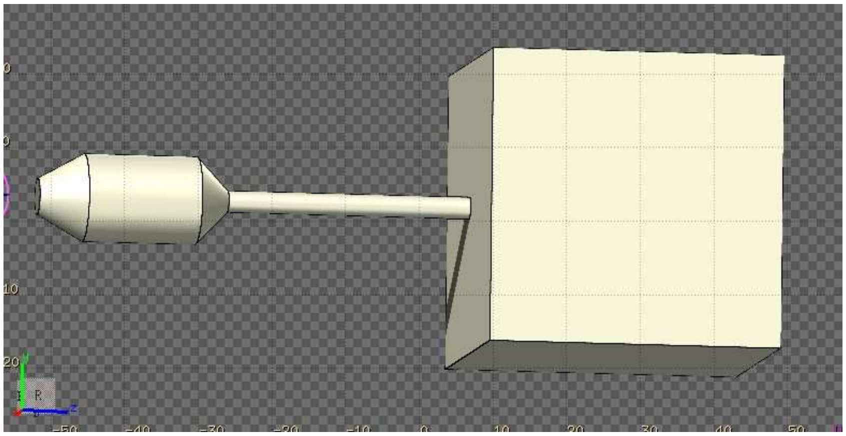

Figure 9. Three-dimentional visualization of FLUKA simulation geometry for the A-1 applicator.

The A-1 applicator was modeled using three PMMA cylinders with outer diameters of 50 mm, 120 mm, and 30 mm, having 5 mm wall thickness and lengths of 64 mm, 157 mm, 334.0 mm, and one truncated cone 45 mm long with the larger and smaller circular base of 120 mm and 30 mm diameter, respectively. A PMMA phantom 40 x 40 x 40 cm^3 was placed at the exit of the applicator. The electron beam arriving on the titanium window is a Gaussian distributed electron profile with full-width of half-maximum (FWHM) on the x and y planes of 3.4 mm and a negligible mean angular spread. The energy cut-offs for the transport and production of both electrons and photons were set to EMFCUT = 10keV (kinetic energy). Particles with an energy below this threshold are not transported further and their energy is locally deposited. The expected dose per electron was evaluated in the PMMA phantom. In order to score the energy deposition, the 40 x 40 x20 cm^3 phantom was divided into 201 x 201 x 200 voxels of size 2 x 2 x 1 mm^3. [10]

6. Results

6.1 PMMA applicator with PMMA phantom

6.1.1 Dose Distribution Plots

In this chapter, we have investigated the 2D dose distribution, using a range of electron energies, including 5, 7, and 9 MeV, as well as higher energies of 50 and 100 MeV. It can be deduced, that as the energy of the electrons increases, so does the depth of beam penetration. Notably, the 50 MeV and 100 MeV electron beams exhibit significantly greater depth, as well as minimal beam loss outside the applicator.

The importance of exploring higher energy electron beams lies in our quest to assess their potential suitability for treating deep-seated tumors.

5 MeV

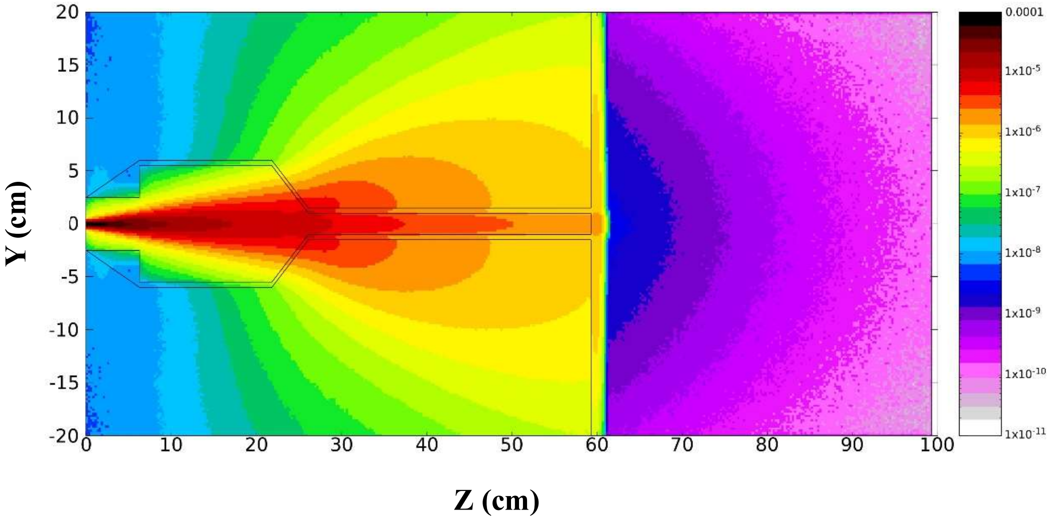

Figure 10. 2D dose distribution for 5 MeV electrons beam inside a 40x40x40 cm^3 *PMMA phantom, passing via an applicator structure of 60 cm lenght.*

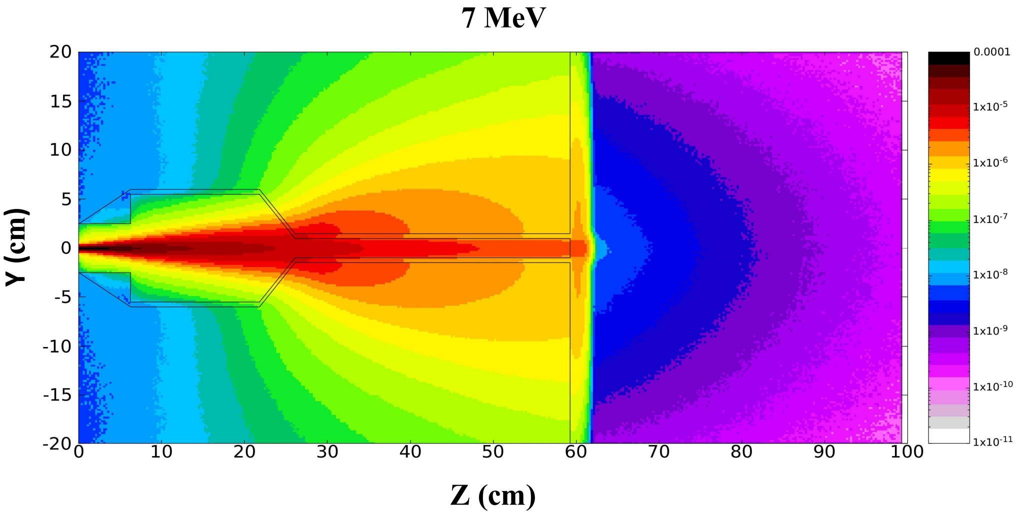

Figure 11. 2D dose distribution for 7 MeV electrons beam inside a 40x40x40 cm^3 PMMA phantom, passing via an applicator structure of 60 cm lenght.

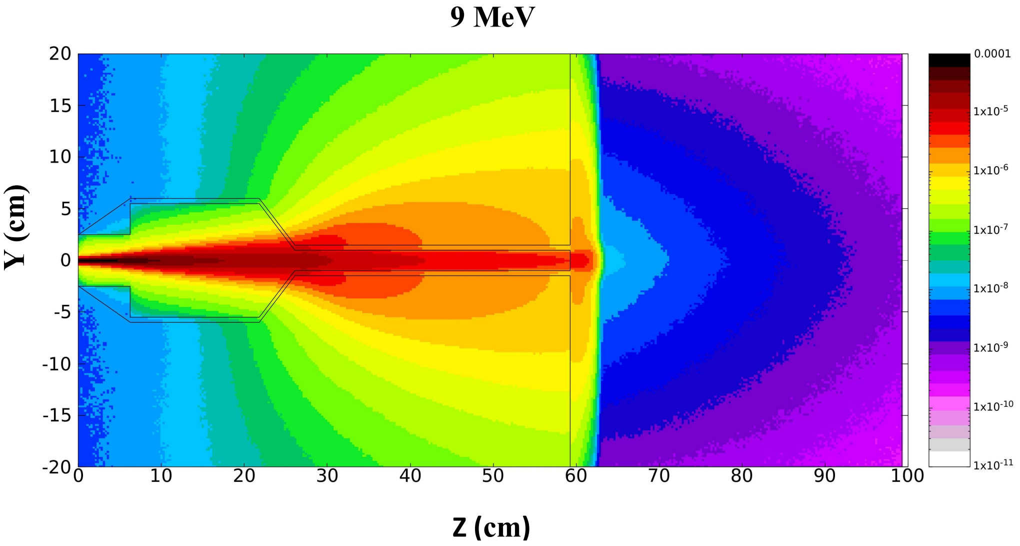

Figure 12. 2D dose distribution for 9 MeV electrons beam inside a 40x40x40 cm^3 PMMA phantom, passing via an applicator structure of 60 cm lenght.

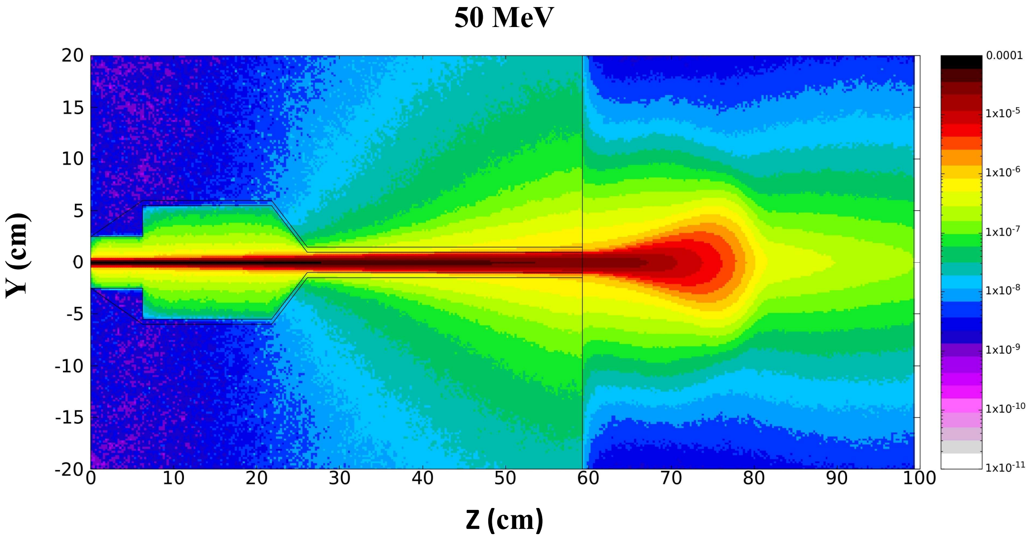

Figure 13. 2D dose distribution for 50 MeV electrons beam inside a 40x40x40 cm³ PMMA phantom, passing via an applicator structure of 60 cm lenght.

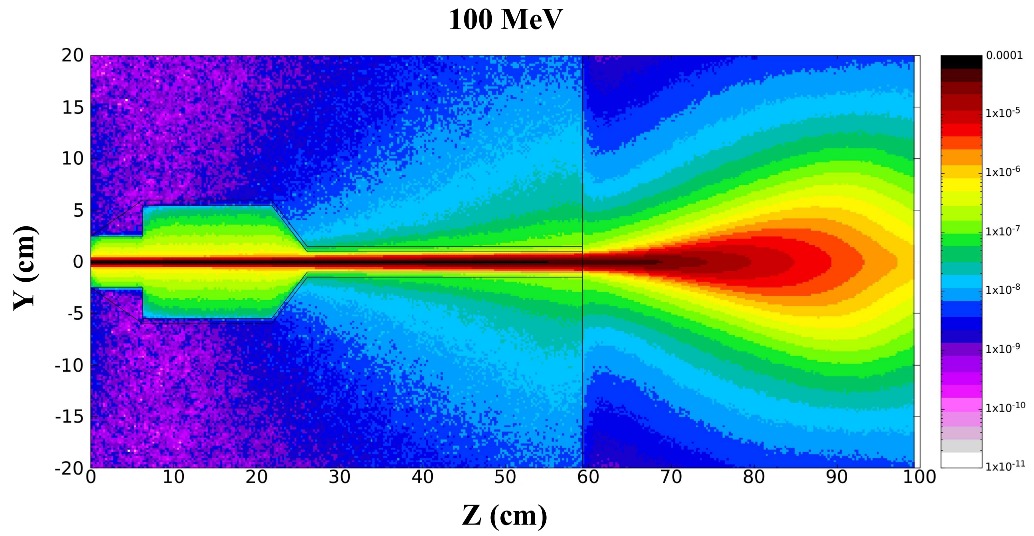

Figure 14. 2D dose distribution for 100 MeV electrons beam inside a 40x40x40 cm³ PMMA phantom, passing via an applicator structure of 60 cm lenght.

6.1.2 Dose to Depth Curves (Gy versus cm)

In this chapter, an examination of beam dosimetry within the phantom is conducted through the analysis of the depth to dose curve. Simulation results for the 5 MeV, 7 MeV and 9 MeV electron beam are presented in the following figures, which report the data of the dose measured along the beam axis as a function of the depth within the PMMA phantom. Additionally, the flash effect parameters for the 5,7 and 9 MeV electron beams are calculated and are in agreement with the flash effect conditions.

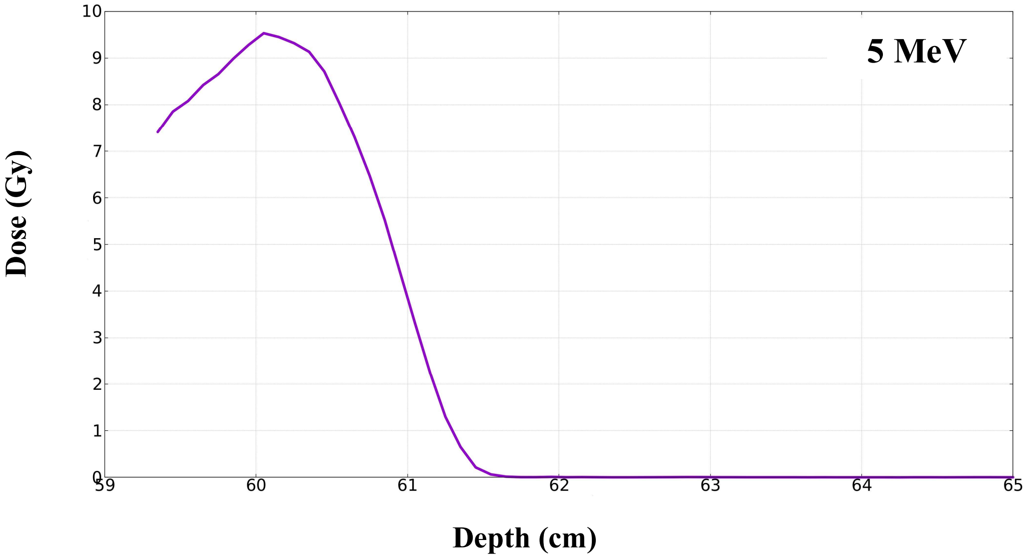

Figure 15. Central axis Dose to Depth curve obtained for the 5 MeV electrons beam for the PMMA applicator inside a 40x40x40 cm³ PMMA phantom.

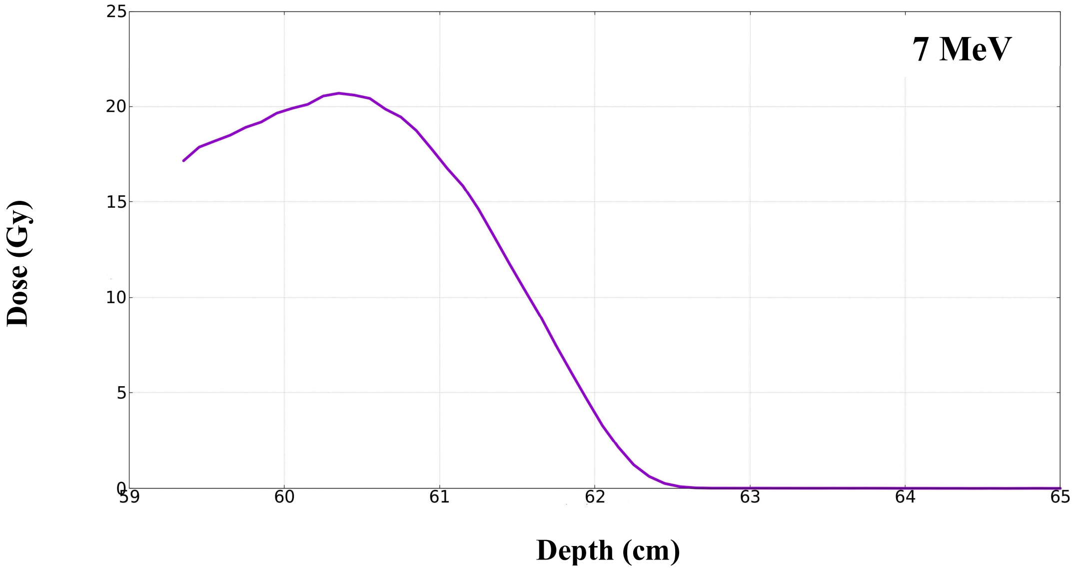

Figure 16. Central axis Dose to Depth curve obtained for the 7 MeV electrons beam for the PMMA applicator inside a 40x40x40 cm³ PMMA phantom.

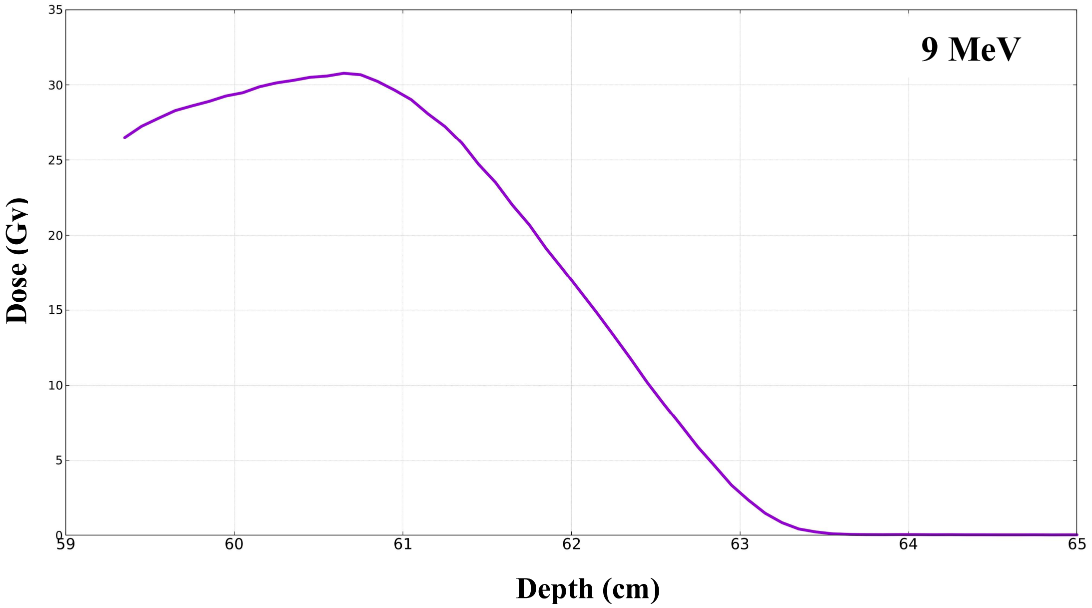

Figure 17. Central axis Dose to Depth curve obtained for the 9 MeV electrons beam for the PMMA applicator inside a 40x40x40 cm^3 PMMA phantom.

The following table (Table 1) reports the dose per pulse, the maximum instantaneous dose rate with a pulse duration of 4 μs and the average dose rate calculated with the pulse repetition frequency of 250 Hz for the 5,7 and 9 MeV electron beam. Together they define the FLASH regime.

Table 1.Dose per pulse, instanteneous dose rate and average dose rate measurments (uncertainty below 1%), obtained for the 5 MeV, 7 MeV and 9 MeV electron beams for a pulse duration of 4 μs and maximun peak beam current of 120 mA for the 7 MeV and 9 MeV beam and 108 mA for the 5 MeV beam. The average dose rate is calculated with the repetition frequency of 250 Hz.

Energy (MeV)	**Maximum peak beam current (mA)**	**Dose per pulse (Gy)**	**Instantaneous Dose rate (Gy/s)**	**Average Dose Rate (Gy/s)**
5	108	9.5	2.38×10^6	2375
7	120	20.7	5.18×10^6	5175
9	120	30.8	7.7×10^6	7700

Flash Effect Conditions

6.1.3 Percentage Depth Dose (PDD) curves

The following figure (Figure 18) reports the percentage depth dose curve measured along the central axis of the beam for the 5 MeV, 7 MeV, 9 MeV, 50 MeV and 100 MeV electrons beam.

Data were normalized to their maximum dose value.

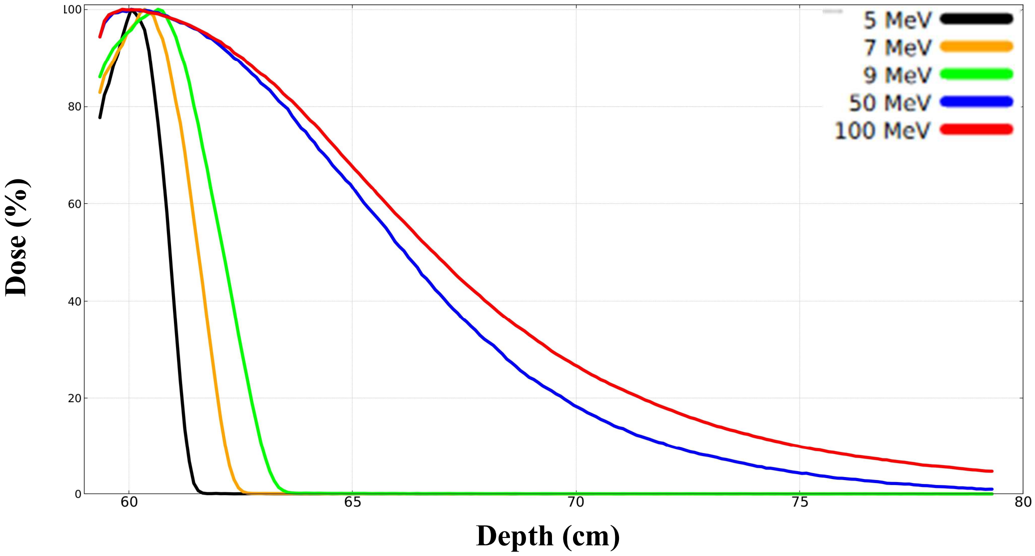

Figure 18. Central axis PDD curves in a 40 x 40 x 40 cm^3 PMMA phantom obtained for the 5 MeV (black line), 7 MeV (orange line), 9 MeV (green line), 50 MeV (blue line) and 100 MeV (red line) electron beams.

Table 2. Dose measurements (uncertainty below 1%), range and depth of the maximum dose of different energies for a PMMA applicator inside a 40 x 40 x 40 cm^3 PMMA phantom.

Beam Energy (MeV)	**Range ± δRange = 1 (mm)**	**Depth of max. ± δDepth = 0.5 (mm)**	**Dose ($\frac{GeV}{g}$)**
5	22	7.5	2.21×10^{-5}
7	32	10.5	4.31×10^{-5}
9	42	13.5	6.41×10^{-5}
50	196	7.5	8.95×10^{-4}
100	216	5.5	2.78×10^{-3}

6.1.4 Dose Profile versus phantom depth

In order to determine the way the beam is distributed within the phantom, we have made the beam profile plots along the central axis of the beam. The depths R_{100}, R_{80} and R_{50} are defined as depths on the electron percentage depth dose curve at which the percentage depth doses attain values of 100%, 80% and 50%, respectively.

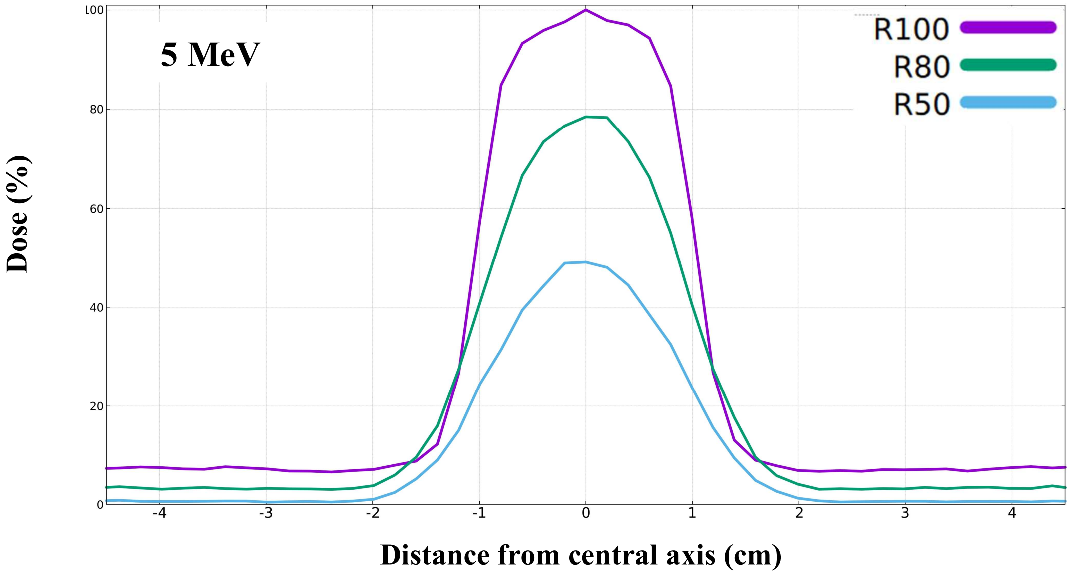

Figure 15. Dose profile in the PMMA phantom obtained for the 5 MeV electrons beam, obtained at a phantom depth of 7.5 mm (R100), 13.5 mm (R80), 16.5 mm (R50) .

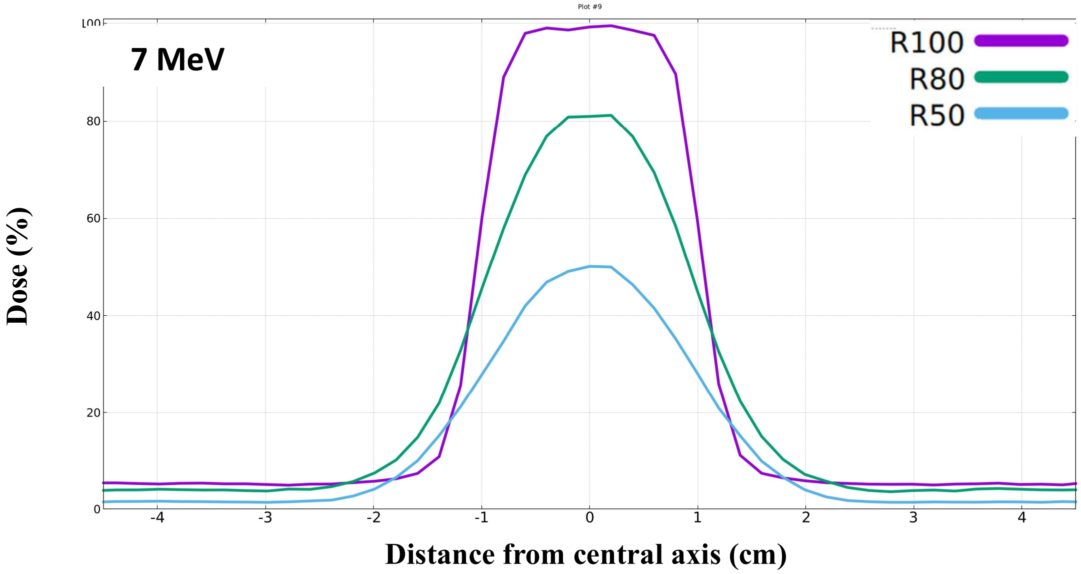

Figure 19. Dose profile in the PMMA phantom obtained for the 7 MeV electrons beam, obtained at a phantom depth of 10.5 mm (R100), 17.5 mm (R80), 22.5 mm (R50) .

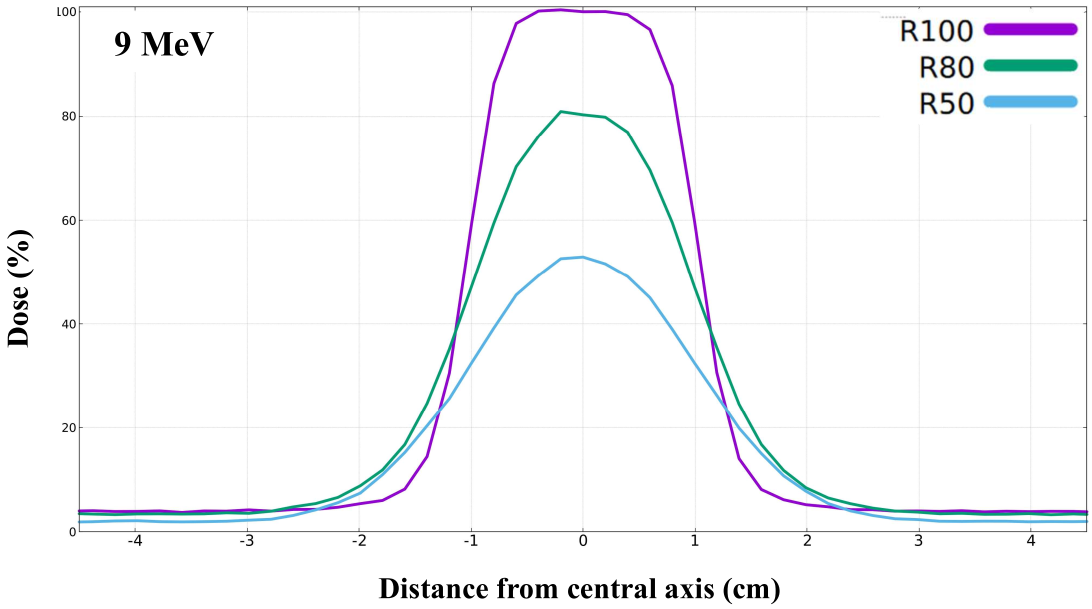

Figure 20. Dose profile in the PMMA phantom obtained for the 9 MeV electrons beam, obtained at a phantom depth of 13.5 mm (R100), 21.5 mm (R80), 27.5 mm (R50).

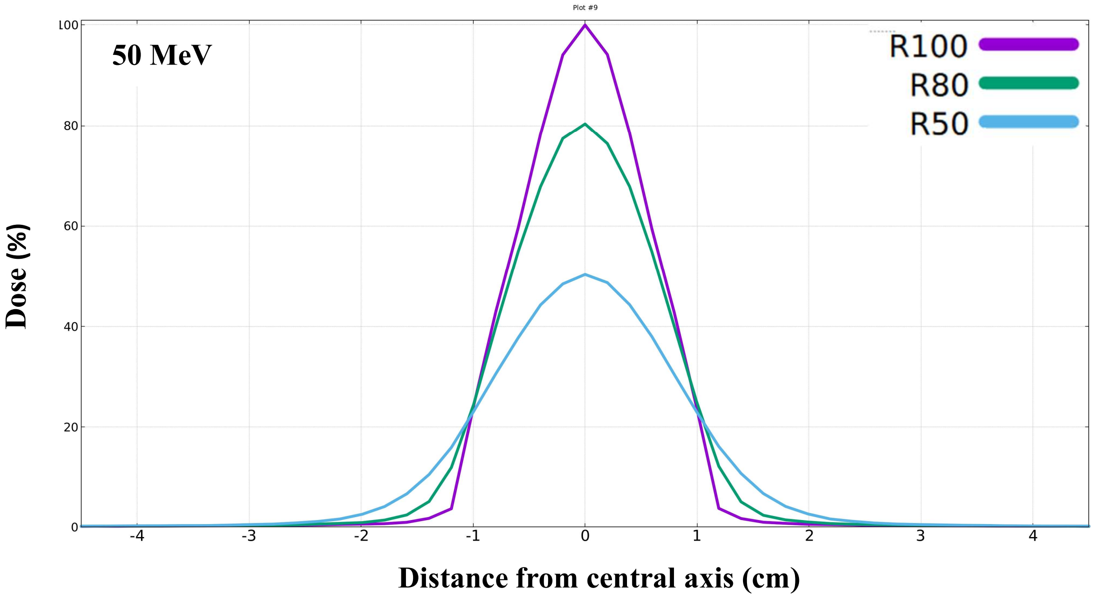

Figure 21. Dose profile in the PMMA phantom obtained for the 50 MeV electrons beam, obtained at a phantom depth of 7.5 mm (R100), 41.5 mm (R80), 68.5 mm (R50).

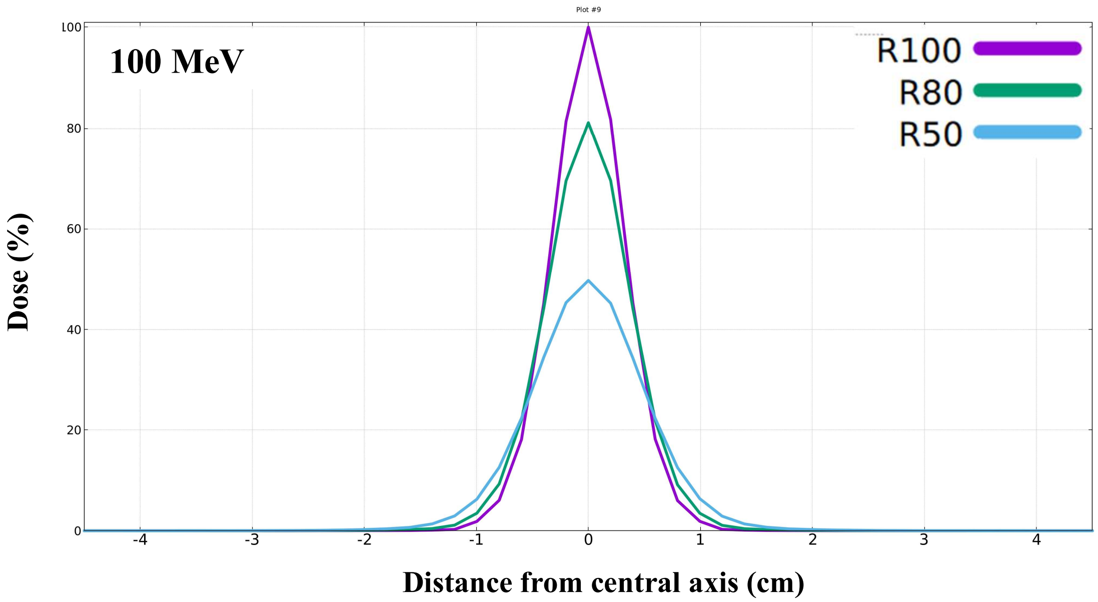

Figure 22. Dose profile in the PMMA phantom obtained for the 100 MeV electrons beam, obtained at a phantom depth of 5.5 mm (R100), 43.5 mm (R80), 75.5 mm (R50).

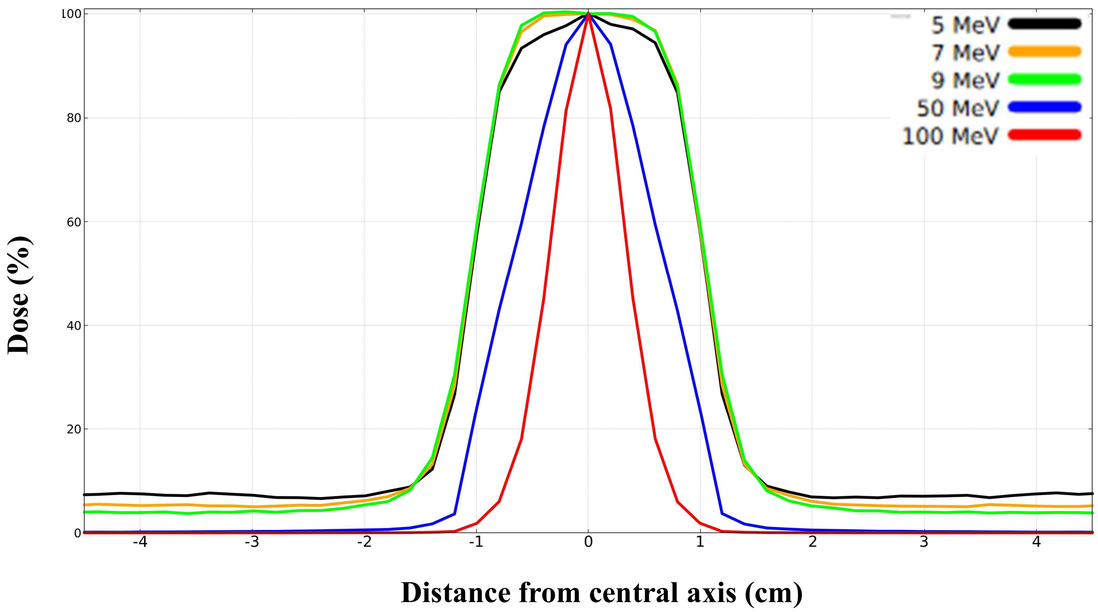

Figure 23. Comparative figure of the dose profile in the PMMA phantom obtained for the 5 MeV (black line), 7 MeV (orange line), 9 meV (green line), 50 MeV (blue line) and 100 MeV (red line) electron beams. The figure shows the profiles obtained at the depth of maximun dose value (R100).

The results obtained from the analysis of the dose profile figures have been presented in the following table. Lower energy electron beams (5,7 and 9 MeV) present a more sharp drop off the beam. Higher energy electron beams (50,100 MeV) penetrate deeper into the PMMA phantom and since R_{80} is used as a therapeutic range, that makes them potentially more suitable for the treatment of deep-seated tumors.

Table 3. Phantom depths on the electron percentage depth dose curve at which the percentage depth doses attain values of 100% (R100), 80% (R80) and 50% (R50), obtained for various electron beam energies in a PMMA phantom.

	Phantom Depth (mm) ± 0.5 mm				
	5 MeV	**7 MeV**	**9 MeV**	**50 MeV**	**100 MeV**
R50	16.5	22.5	27.5	68.5	75.5
R80	13.5	17.5	21.5	41.5	43.5
R100	7.5	10.5	13.5	7.5	5.5

6.2 PMMA applicator with WATER phantom

Using the same PMMA applicator we changed the phantom material to water. The following figures show the PDD curves for 5Mev, 7Mev, 9MeV, 50MeV and 100 MeV energies.

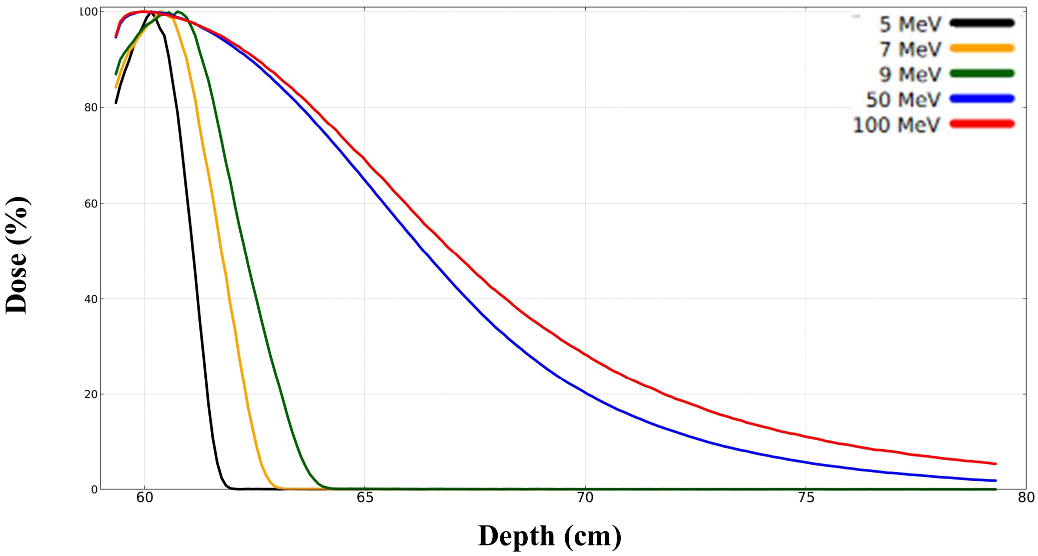

Figure 24. Central axis PDD curves in Water phantom obtained for the 5 MeV (black line), 7 MeV (orange line), 9 MeV (green line), 50 MeV (blue line) and 100 MeV (red line) electron beams.

Table 4. Dose per pulse, instanteneous dose rate and average dose rate measurments (uncertainty below 1%), obtained for the 5 MeV, 7 MeV and 9 MeV electron beams for a pulse duration of 4 µs and maximun peak beam current of 120 mA for the 7 MeV and 9 MeV beam and 108 mA for the 5 MeV beam. The average dose rate is calculated with the repetition frequency of 250 Hz.

Energy (MeV)	Maximum peak beam current (mA)	Dose per pulse (Gy)	Instantaneous Dose rate (Gy/s)	Average Dose Rate (Gy/s)
5	108	9.6	2.40×10^{6}	2400
7	120	21.0	5.25×10^{6}	5250
9	120	31.4	7.85×10^{6}	7850

Table 5. Dose measurements (uncertainty below 1%) of different energies for a PMMA applicator inside a Water phantom.

Beam Energy (MeV)	Range ± δRange=0.1 (mm)	Depth of max. ± δDepth = 0.5 (mm)	Dose ($\frac{GeV}{g}$)
5	26	8.5	2.22×10^{-5}
7	36	10.5	4.38×10^{-5}
9	46	14.5	6.53×10^{-5}
50	219	7.5	9.23×10^{-4}
100	229	6.5	2.84×10^{-3}

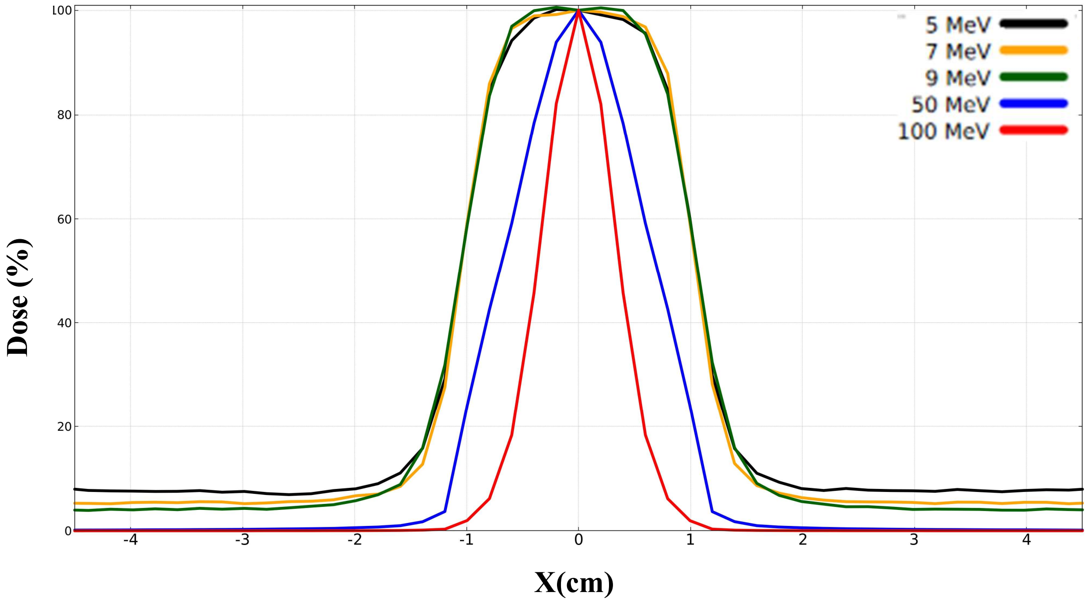

Figure 25. Comparative figure of the dose profile in the Water phantom, obtained for the 5 MeV (black line), 7 MeV (orange line), 9 meV (green line), 50 MeV (blue line) and 100 MeV (red line) electron beams. The figure shows the profiles obtained at the depth of maximun dose value (R100).

Table 6. Phantom depths on the electron percentage depth dose curve at which the percentage depth doses attain values of 100% (R100), 80% (R80) and 50% (R50), obtained for various electron beam energies in a Water phantom.

	Phantom Depth (mm) ± 0.5 mm				
	5 MeV	**7 MeV**	**9 MeV**	**50 MeV**	**100 MeV**
R50	17.5	24.5	29.5	70.5	76.5
R80	14.5	18.5	22.5	42.5	45.5
R100	8.5	10.5	14.5	6.5	6.5

6.3 Comparison of the PMMA and Water Phantom

In this chapter, a comparison of the PMMA and Water as phantom materials has been made, by studying the PDD plots.

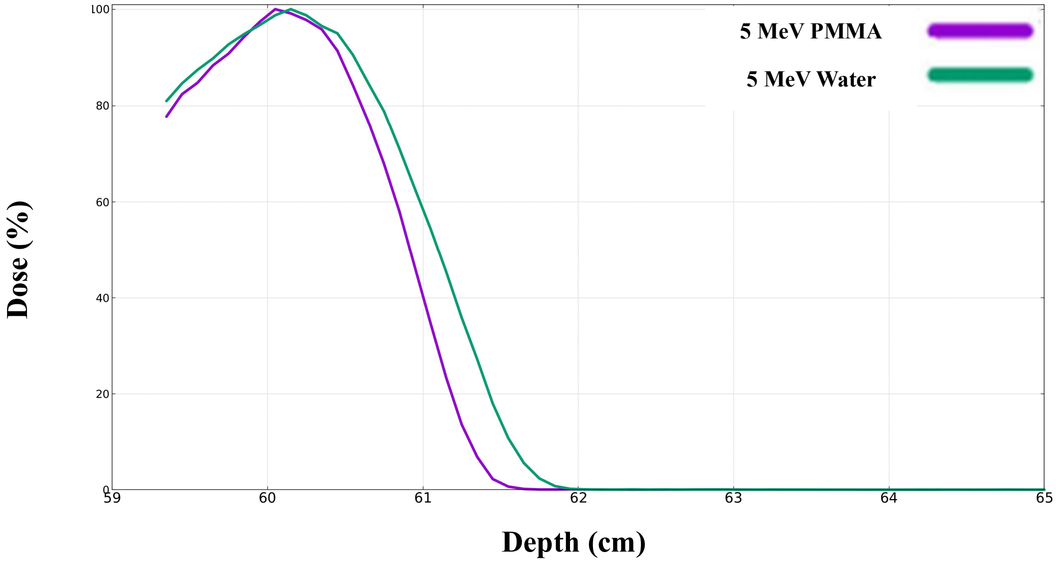

Figure 26. Central axis PDD curves obtained for the 5 MeV electrons beam inside a PMMA (purple line) and a Water (green line) 40x40x40 cm^3 phantom.

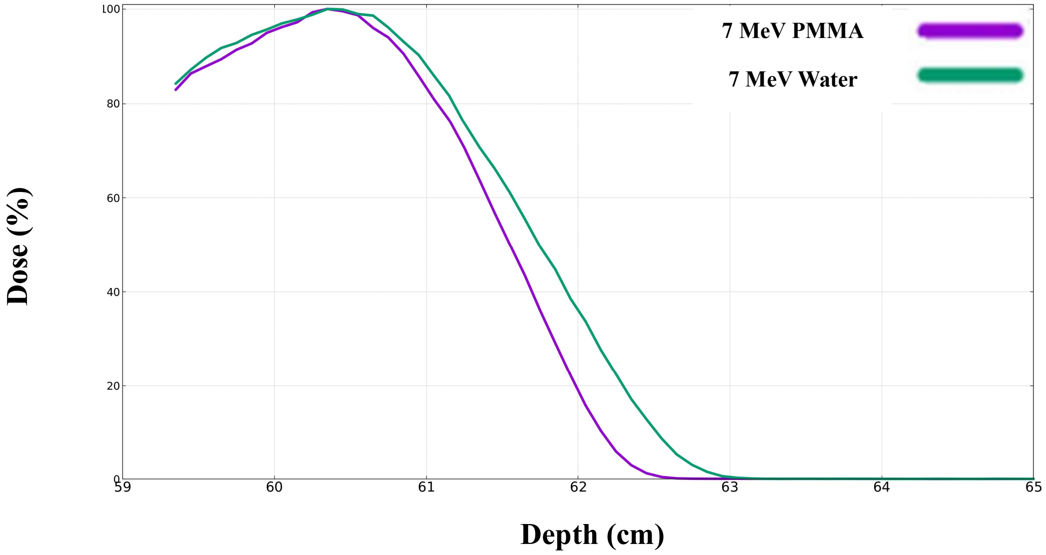

Figure 27. Central axis PDD curves obtained for the 7 MeV electrons beam inside a PMMA (purple line) and a Water (green line) 40x40x40 cm^3 phantom.

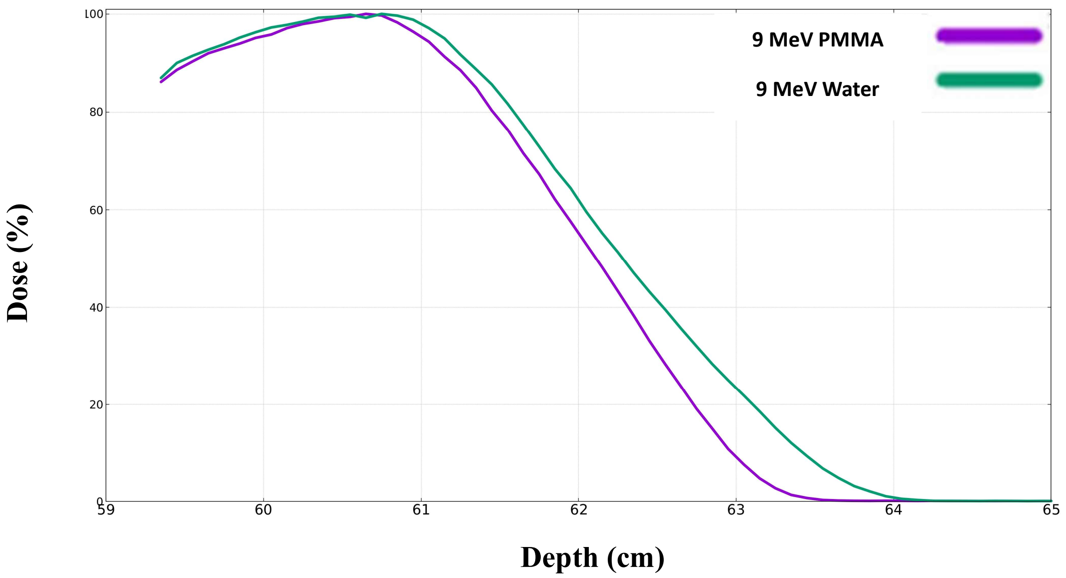

Figure 28. Central axis PDD curves obtained for the 9 MeV electrons beam inside a PMMA (purple line) and a Water (green line) 40x40x40 cm^3 phantom.

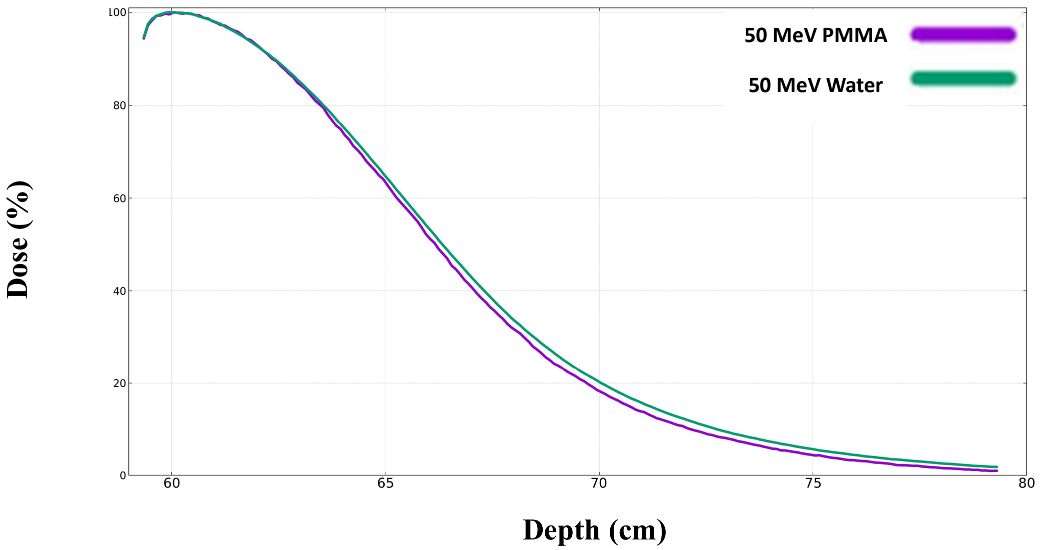

Figure 29. Central axis PDD curves obtained for the 50 MeV electrons beam inside a PMMA (purple line) and a Water (green line) 40x40x40 cm^3 phantom.

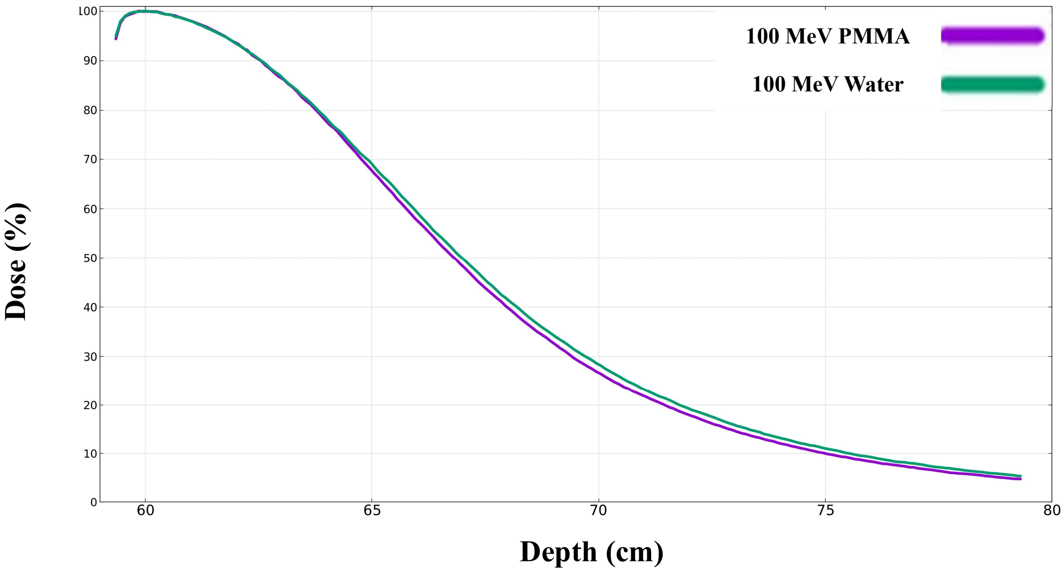

Figure 30. Central axis PDD curves obtained for the 100 MeV electrons beam inside a PMMA (purple line) and a Water (green line) 40x40x40 cm^3 phantom.

Based on the previous plots, it can be deduced that at all electron energies, PMMA shows great similarities with water as a phantom material. All maximum dose measurements show that the range of the electrons and the dose are slightly bigger inside the water phantom than the PMMA phantom.

Table 7. Comparison of dose measurements (uncertainty below 1%) of different energies for a PMMA applicator inside a PMMA and a Water phantom.

Beam Energy (MeV)	**Range ± δRange=0.1 (mm)**		**Depth of max. ± δDepth = 0.5 (mm)**		**Dose ($\frac{GeV}{g}$)**	
	PMMA	Water	PMMA	Water	PMMA	Water
5	22	26	7.5	8.5	2.21 x 10^{-5}	2.22 x 10^{-5}
7	32	36	10.5	10.5	4.31 x 10^{-5}	4.38 x 10^{-5}
9	42	46	13.5	14.5	6.41 x 10^{-5}	6.53 x 10^{-5}
50	196	219	7.5	7.5	8.95 x 10^{-4}	9.23 x 10^{-4}
100	216	229	5.5	6.5	2.78 x 10^{-3}	2.84 x 10^{-3}

6.4 Applicator Geometry

A pivotal aspect of electron therapy lies in the understanding of how an applicator design influence dose distribution. This study will focus specifically on the variations in dose profiles and flash effect conditions of a 7 MeV electron beam. In Table 8 we present the diameters of the applicator cylinders for all three applicators that are used in this study (A-1, A-2, A-3).

Table 8. Diameters of the first (d1), second (d2) and third (d3) cylinder for the A-1, A-2 and A-3 applicator.

	cylinder diameters (mm)		
	d1	**d2**	**d3**
A-1	50	120	30
A-2	50	85	30
A-3	50	120	60

6.4.1 Diameter variation of the second applicator cylinder

The A-1 applicator was modified by reducing the diameter of the second cylinder from 120 mm to 85 mm (applicator A-2), while maintaining the same SSD of 60 cm.

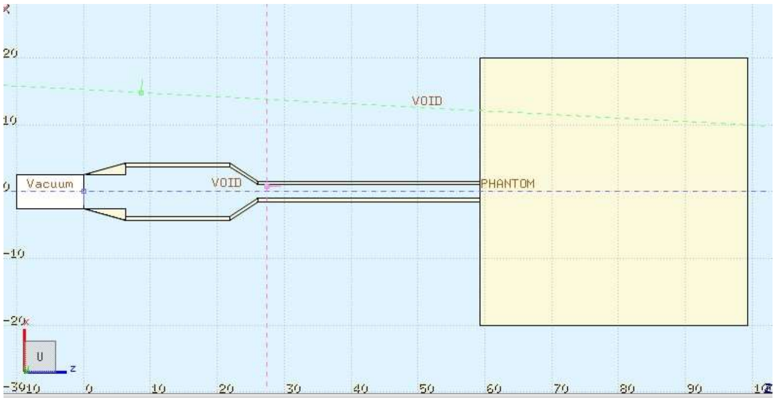

Figure 31. Two-dimensional visualization of FLUKA simulation geometry used for the A-2 applicator. The beam travels in the z direction.

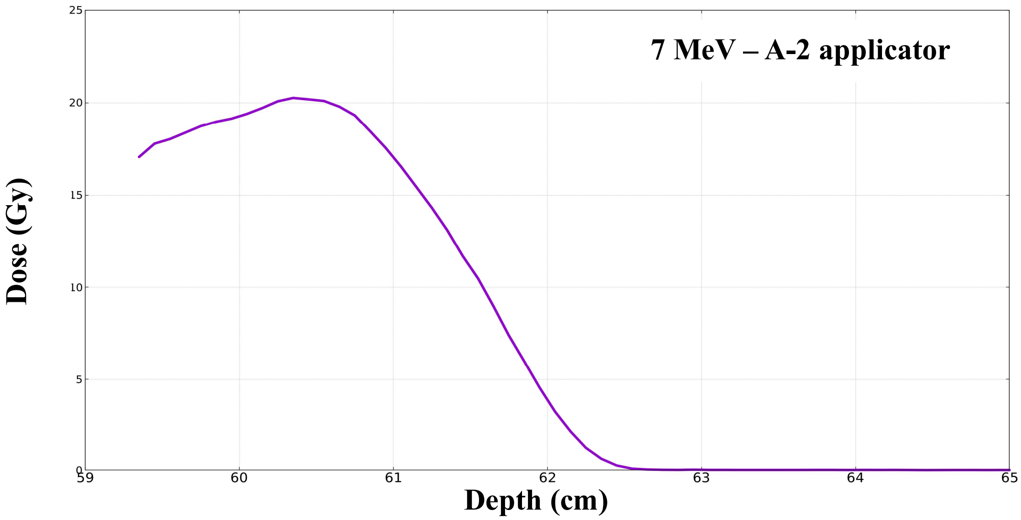

Figure 32. Dose to Depth curve obtained for the 7 MeV electrons beam for the A-2 applicator inside a 40x40x40 cm^3 PMMA phantom.

By making this geometry modification, it is apparent that no significant differences have been observed in the dose measurement and flash effects parameters, as presented in the following table (Table 9).

Table 9. Dose per pulse, instanteneous dose rate and average dose rate measurments, obtained for the 7 MeV electrons beam for the A-2 applicator inside the PMMA phantom. The pulse duration is 4 µs and the maximun peak beam current is 120 mA. The average dose rate is calculated with the repetition frequency of 250 Hz.

Energy (MeV)	Dose per pulse (Gy)	Instantaneous Dose rate (Gy/s)	Average Dose Rate (Gy/s)
7	20.3	5.08 x 10^6	5075

6.4.1.1 Dose Distribution Plots

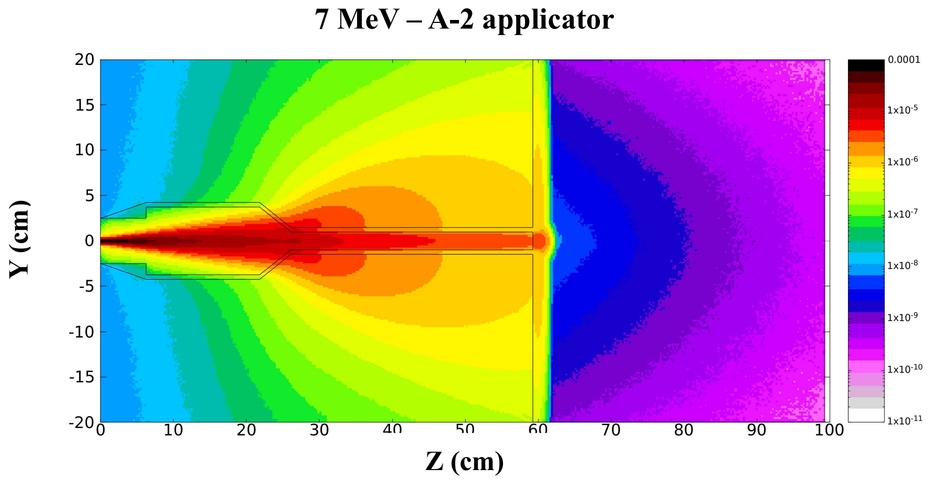
7 MeV – A-2 applicator

Figure 33. 2D dose distribution for 7 MeV electrons beam for the A-2 applicator inside a 40x40x40 cm^3 PMMA phantom.

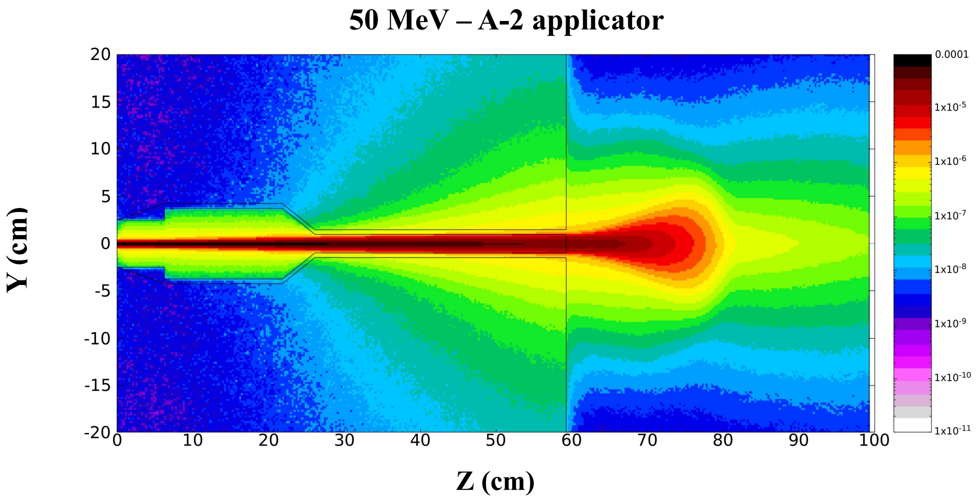
50 MeV – A-2 applicator

Figure 34. 2D dose distribution for 50 MeV electrons beam for the A-2 applicator inside a 40x40x40 cm^3 PMMA phantom.

6.4.1.2 Dose Profiles of the A-2 applicator and comparison with the A-1 applicator

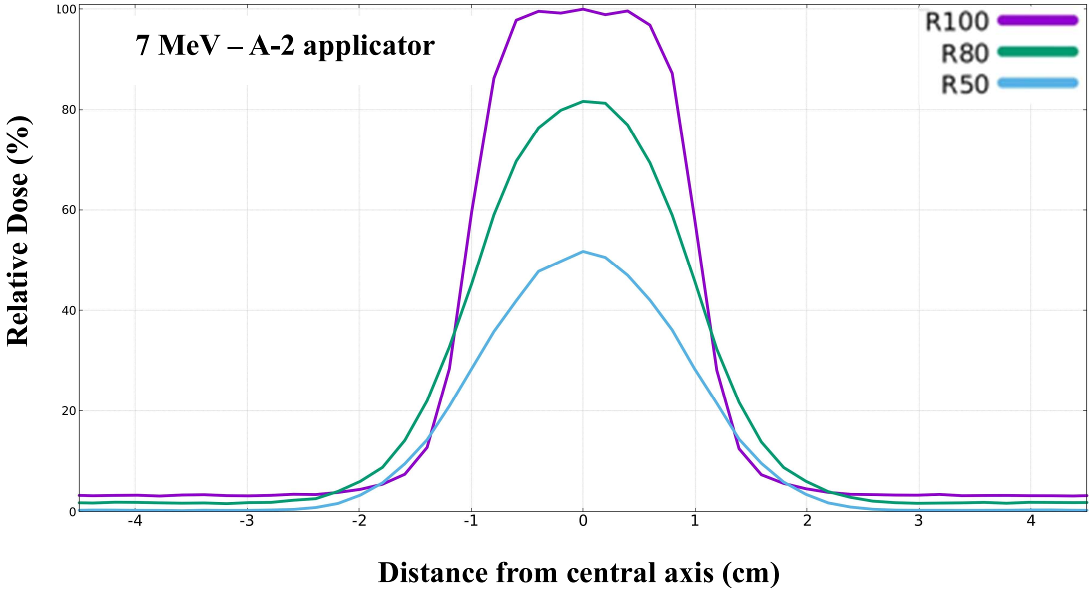

Figure 35. Dose profile of the A-2 applicator in the PMMA phantom obtained for the 7 MeV electrons beam. The figure shows the profiles obtained at a phantom depth of 10.5 mm (R100), 17.5 mm (R80), 22.5 mm (R50).

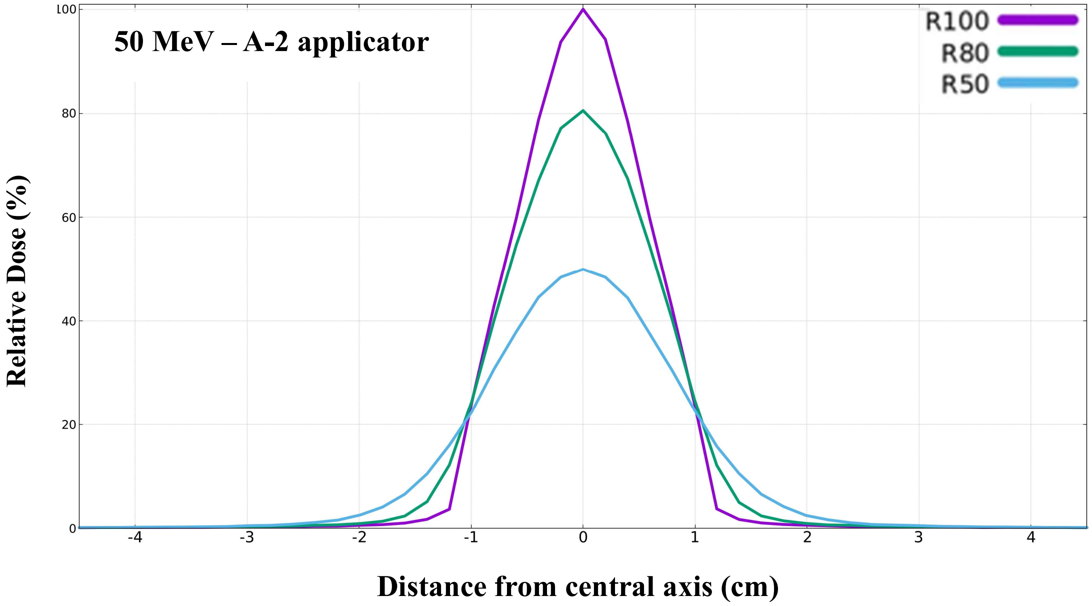

Figure 36. Dose profile of the A-2 applicator in the PMMA phantom obtained for the 50 MeV electrons beam. The figure shows the profiles obtained at a phantom depth of 7.5 mm (R100), 41.5 mm (R80), 68.5 mm (R50).

In the next figure (Figure 37), we observe that for the A-2 applicator the dose drops lower at the central axis beam profile figures. However, the beam is maintaining the same flatness and symmetry.

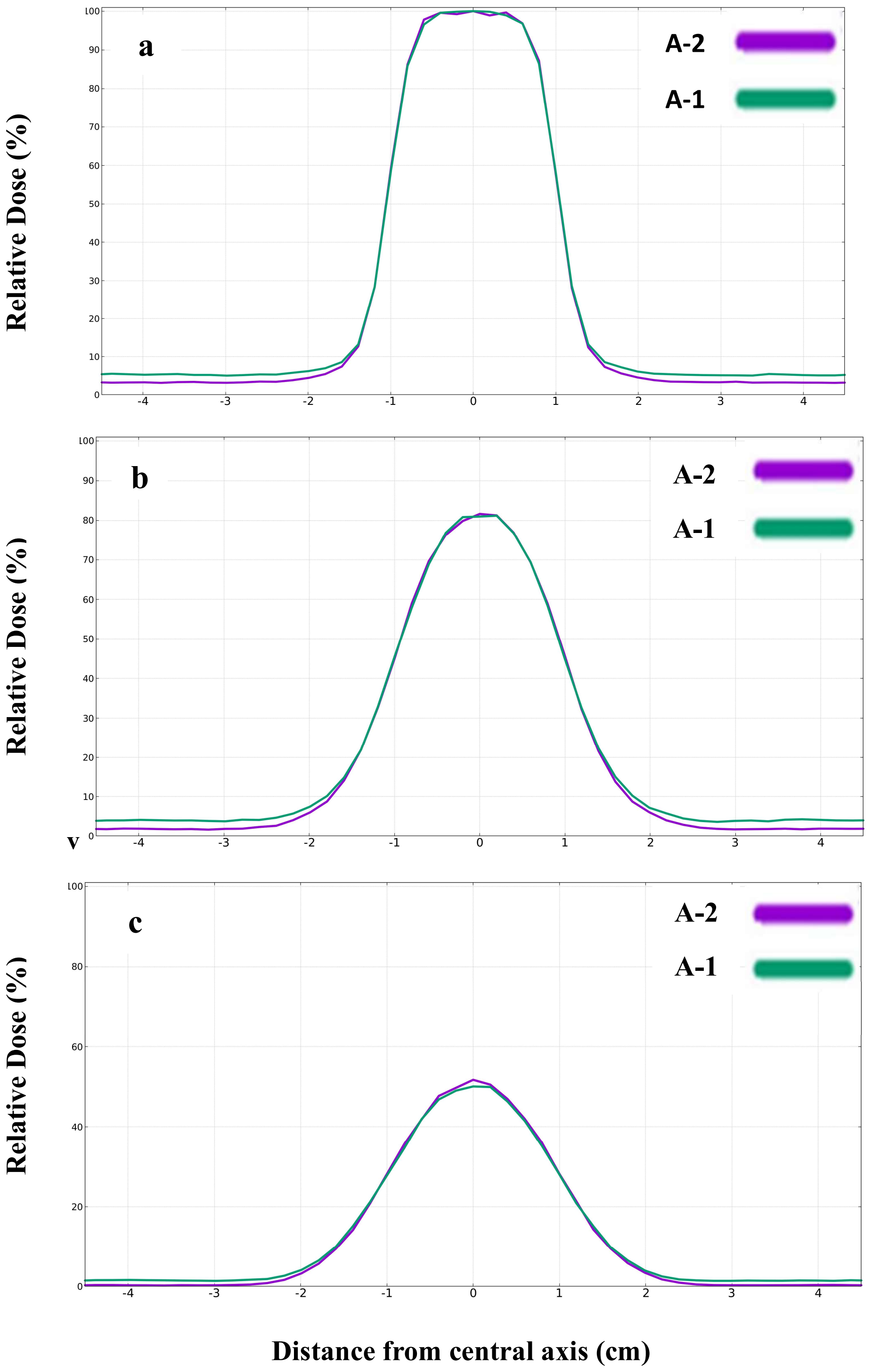

*Figure 37. Dose profile in the PMMA phantom obtained for the 7 MeV electrons beam for the A-1 (green line) and the A-2 (purple line) applicator inside the PMMA phantom. The figure shows the profiles obtained at the depths on the electron percentage depth dose curve at which the percentage depth doses attain value of 100% (R100) [**a**] , 80% (R80) [**b**] and 50% (R50) [**c**].*

6.4.2 Diameter variation of the third applicator cylinder

In this chapter, the A-1 applicator was modified by increasing the diameter of the third cylinder from 30 mm to 60 mm (applicator A-3), while maintaining the same SSD of 60 cm (Figure 37).

Figure 38. Two-dimensional visualization of FLUKA simulation geometry used for the A-3 applicator. The beam travels in the z direction.

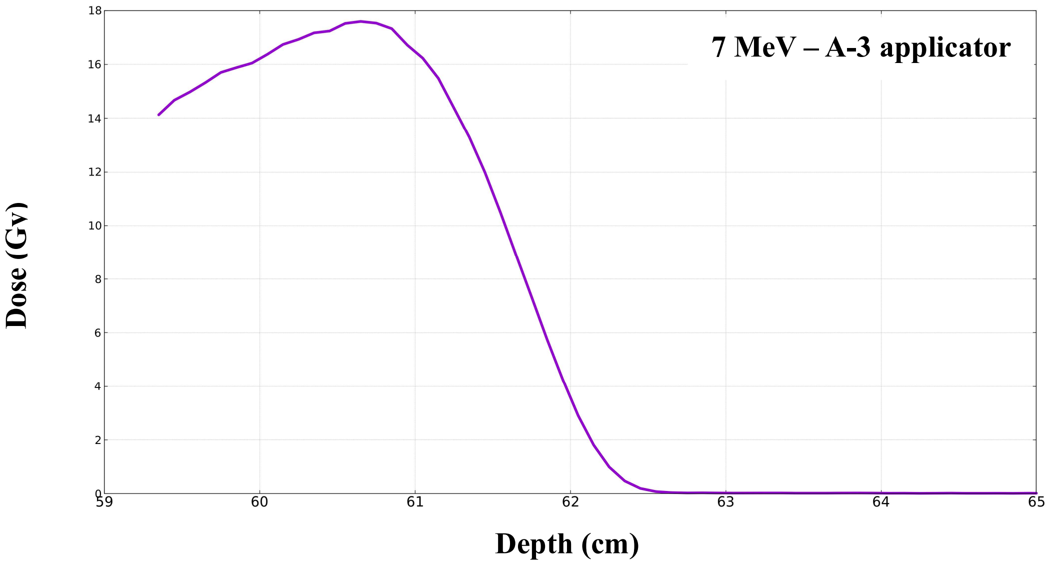

Figure 39. Dose to Depth curve obtained for the 7 MeV electrons beam for the A-3 applicator inside a 40x40x40 cm^3 PMMA phantom.

Table 10. Dose per pulse, instanteneous dose rate and average dose rate measurments, obtained for the 7 MeV electrons beam for the A-3 applicator inside the PMMA phantom. The pulse duration is 4 µs and the maximun peak beam current is 120 mA. The average dose rate is calculated with the repetition frequency of 250 Hz.

Energy (MeV)	Dose per pulse (Gy)	Instantaneous Dose rate (Gy/s)	Average Dose Rate (Gy/s)
7	17.6	4.40×10^6	4400

6.4.2.1 Dose Distribution Plots

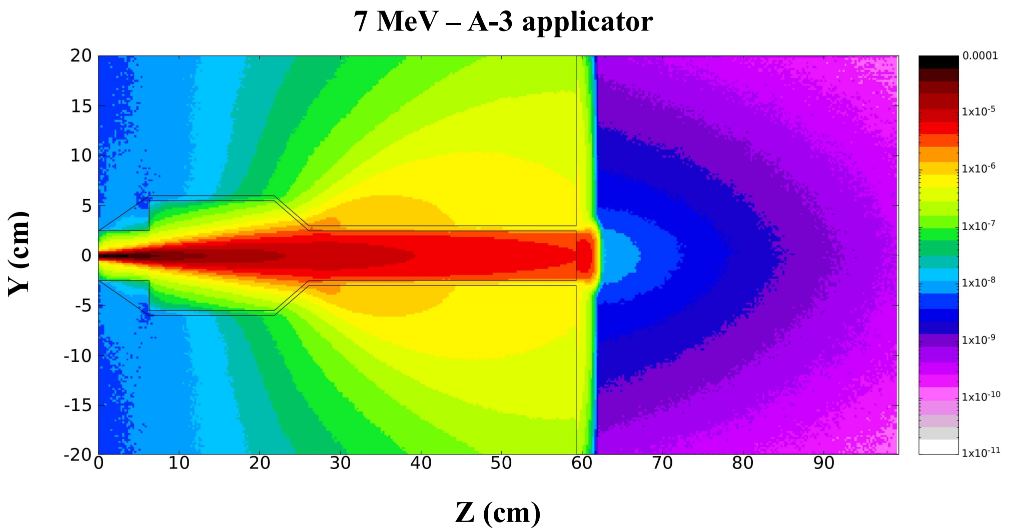

Figure 40. 2D dose distribution for 7 MeV electrons beam for the A-3 applicator inside a PMMA phantom.

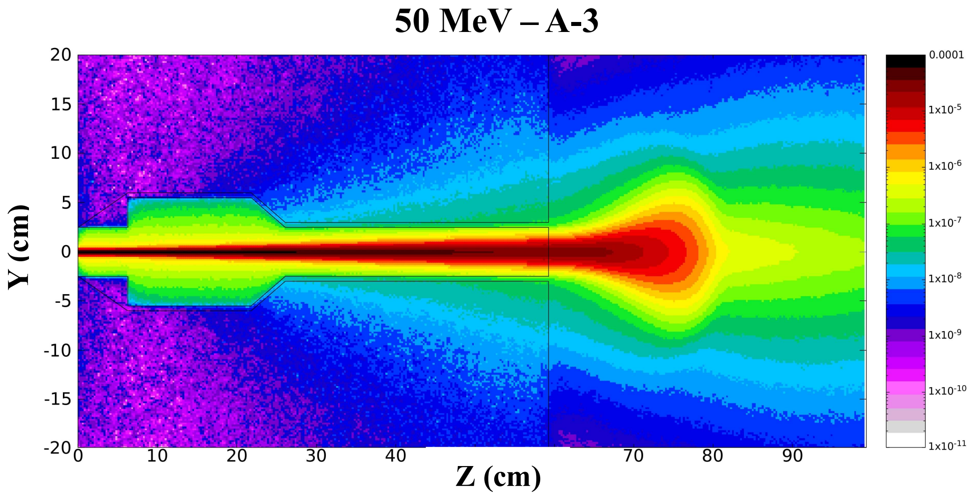

Figure 41. 2D dose distribution for 50 MeV electrons beam for the A-3 applicator inside a PMMA phantom.

6.5.2.2. Transverse Dose Profiles of the A-3 applicator and comparison with the A-1 applicator

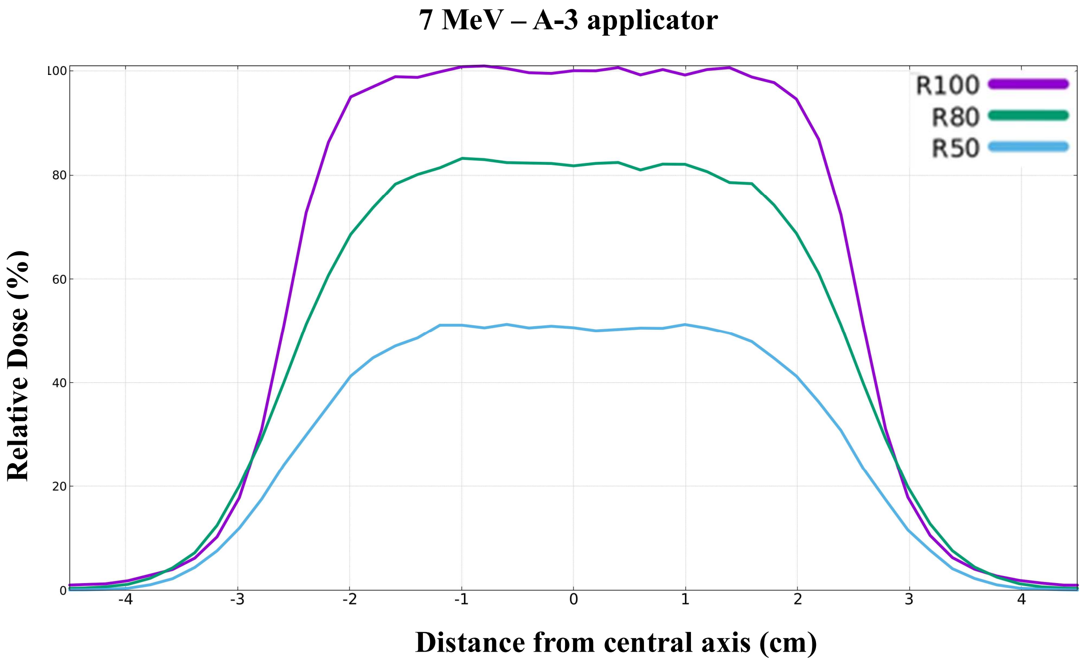

Figure 42. Dose profile of the A-3 applicator in the PMMA phantom obtained for the 7 MeV electron beam. The figure shows the profiles obtained at a phantom depth of 13.5 mm (R100), 19.5 mm (R80), 23.5 mm (R50).

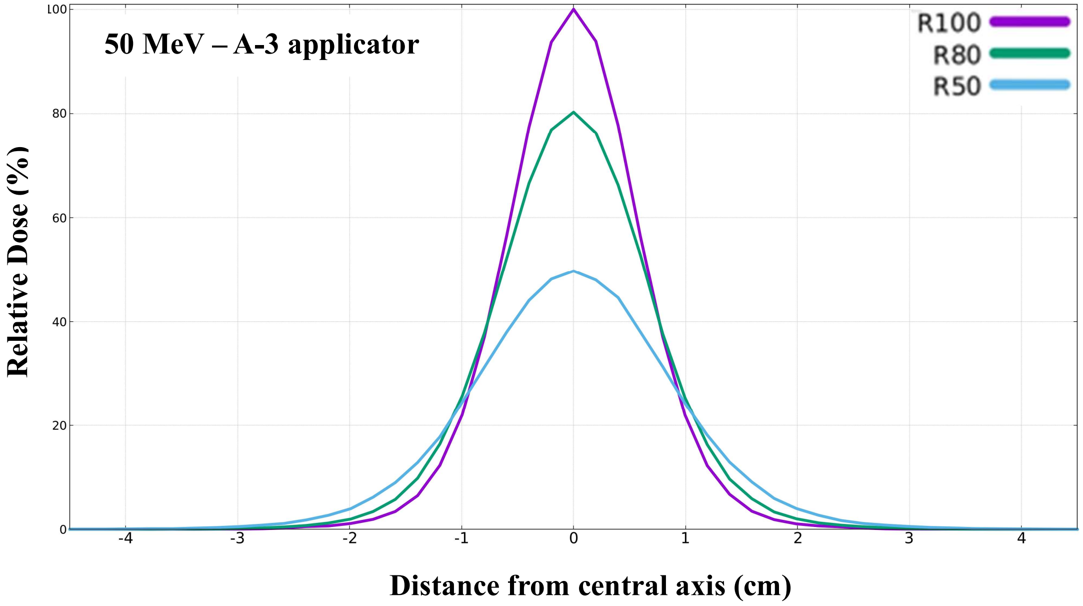

Figure 43. Dose profile of the A-3 applicator in the PMMA phantom obtained for the 50 MeV electron beam. The figure shows the profiles obtained at a phantom depth of 7.5 mm (R100), 40.5 mm (R80), 67.5 mm (R50).

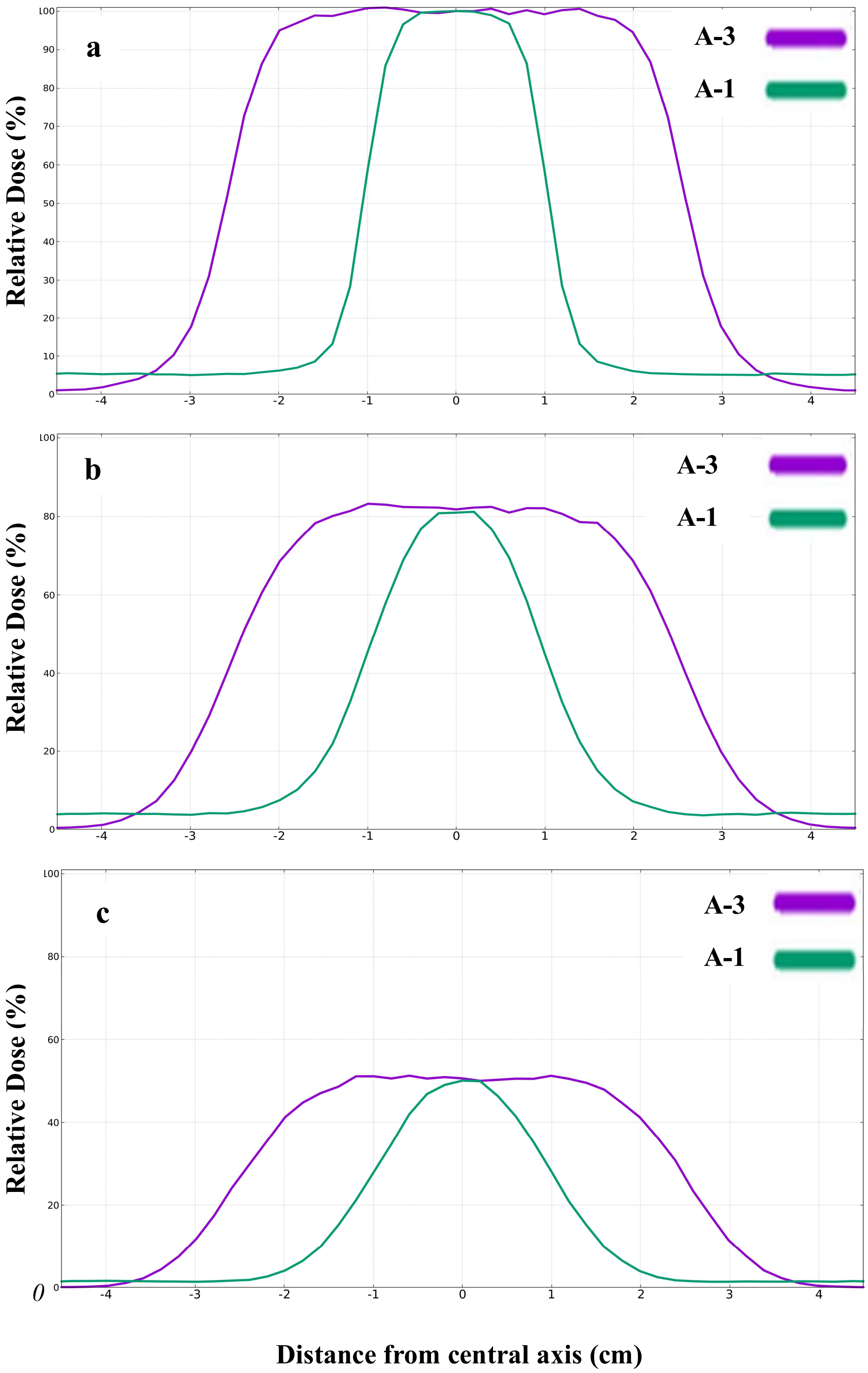

*Figure 44. Comparative figure of the dose profile obtained for the 7 MeV electrons beam for the A-1 (green line) and the A-3 applicator (purple line) inside the PMMA phantom. The figure shows the profiles obtained at the depths on the electron percentage depth dose curve at which the percentage depth doses attain value of 100% (R100) [**a**] , 80% (R80) [**b**] and 50% (R50) [**c**].*

By alternating the diameter of the third cylinder, we can observe a greater beam flatness (Figure 43). Beam flatness is a fundamental aspect of radiation therapy quality control and ensuring a flat and uniform dose distribution is essential for maximizing treatment efficacy.

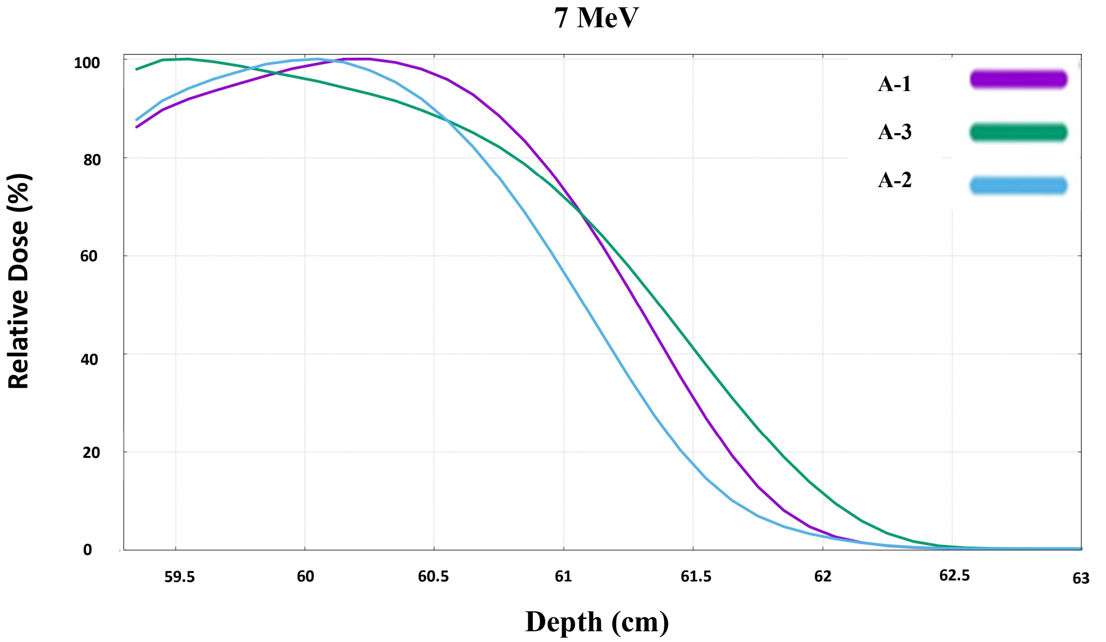

Figure 45. Comparative figure of dose distribution across the whole phantom for a 7 MeV electrons beam inside a 40x40x40 cm^3 PMMA phantom for different applicator geometries.

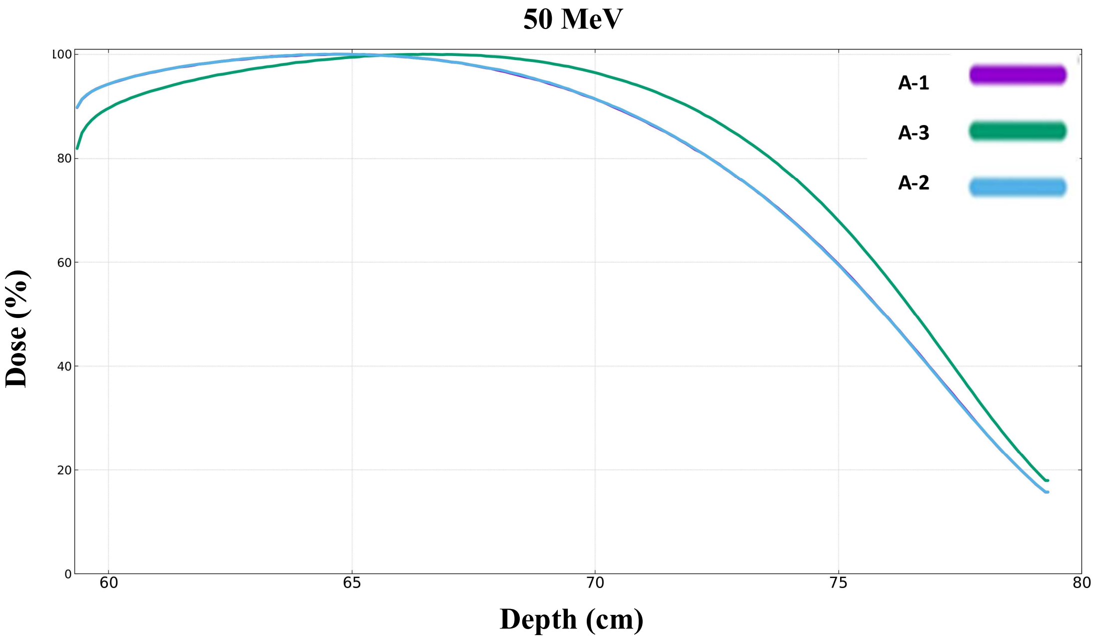

Figure 46. Comparative figure of dose distribution across the whole phantom for a 50 MeV electrons beam inside a 40x40x40 cm^3 PMMA phantom for different applicator geometries.

6.5 Applicator Materials

We changed the material of the applicator cylinders to aluminum, copper and iron, ignoring bremsstrahlung effects, in order to study more heavy metals.

6.5.1 Aluminum

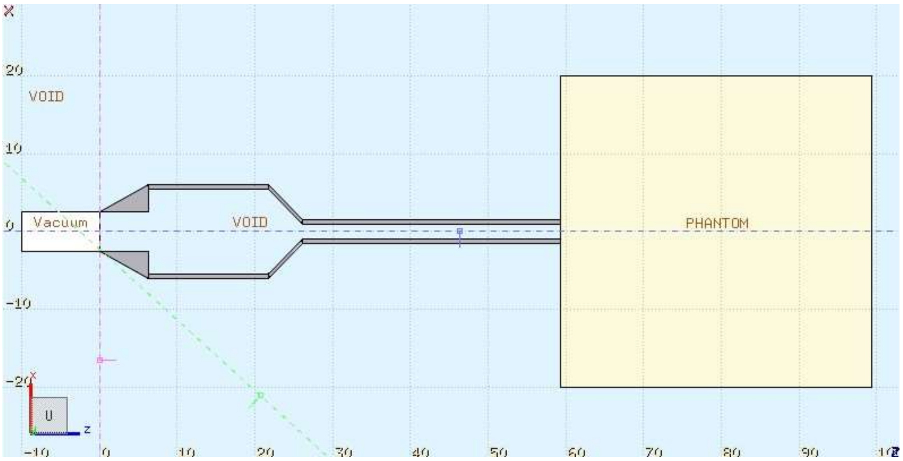

Figure 47. Two-dimensional visualization of FLUKA simulation geometry for the aluminium applicator. The beam travels in the z direction.

6.5.1.1 Aluminum with PMMA phantom

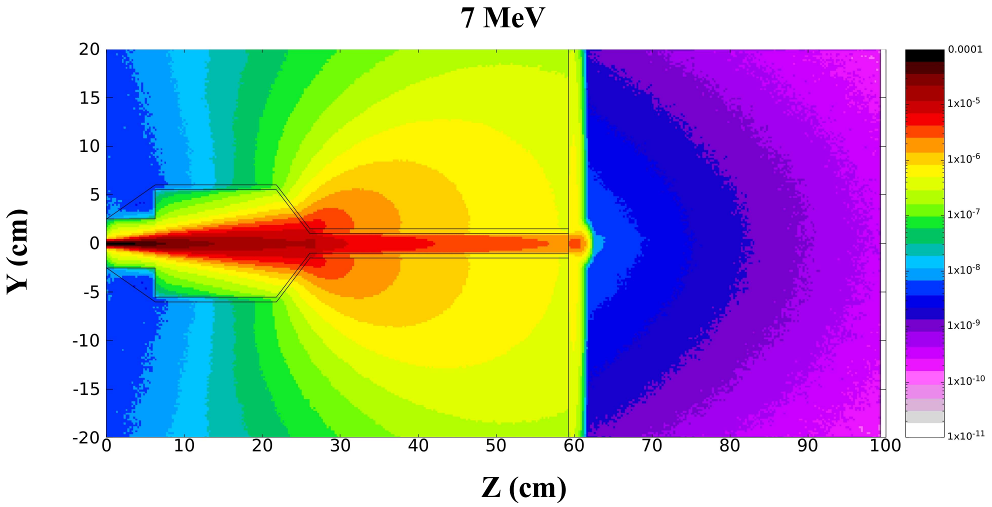

Figure 48. 2D dose distribution for 7 MeV electrons beam for the aluminum applicator inside a 40x40x40 cm^3 PMMA phantom.

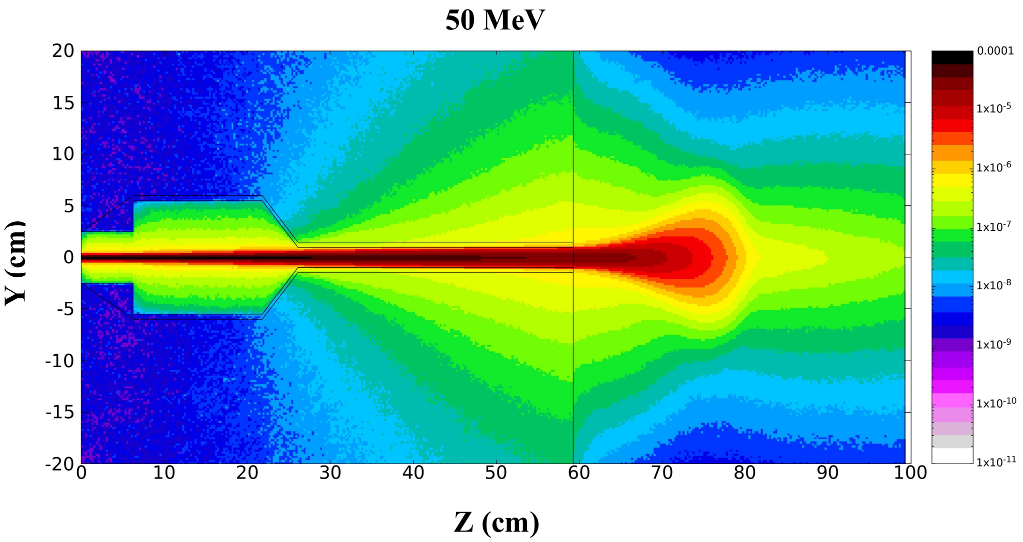

Figure 49. 2D dose distribution for 50 MeV electrons beam for the aluminum applicator inside a 40x40x40 cm^3 PMMA phantom.

The measured dose at the central axis of the beam in the phantom is 4.22 x 10^{-5} $\frac{GeV}{g}$ for the 7 MeV and 9.05 x 10^{-4} $\frac{GeV}{g}$ for the 50 MeV for the aluminium applicator, which is lower than that of the PMMA applicator for the 7 MeV beam and bigger for the 50 MeV beam (4.31 x 10^{-5} $\frac{GeV}{g}$ for the 7 MeV and 8.95 x 10^{-4} $\frac{GeV}{g}$ for the 50 MeV for the PMMA applicator). All dose measurements have uncertainty below 1%.

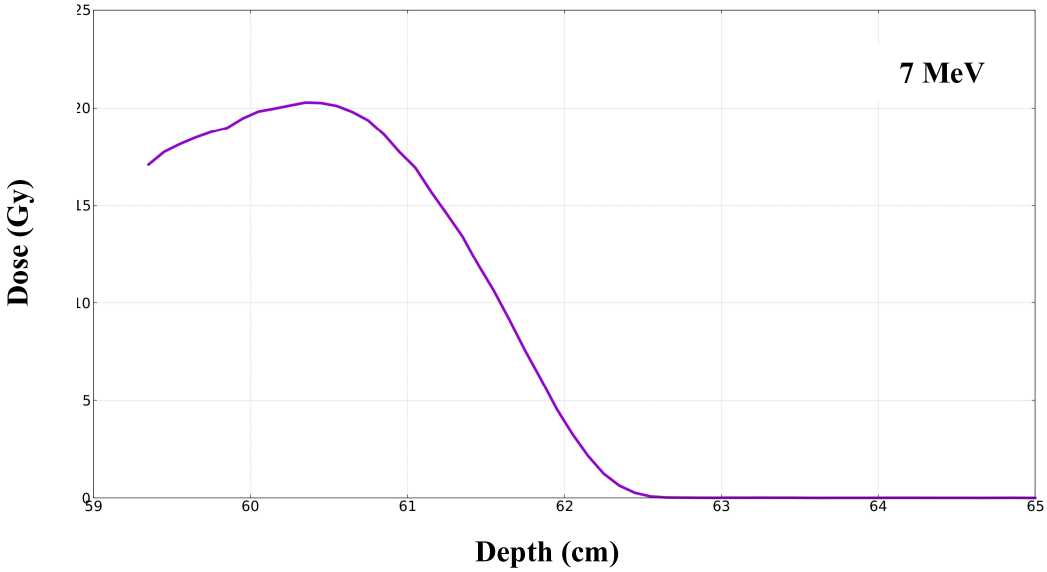

Figure 50. Dose to Depth curve obtained for the 7 MeV electrons beam for the aluminum applicator inside a 40x40x40 cm^3 PMMA phantom.

We notice that all dose parameter calculations for the aluminium applicator (Table 11), agree with flash effect conditions.

Table 11. Dose per pulse, instanteneous dose rate and average dose rate measurments (uncertainty below 1%), obtained for the 7 MeV electrons beam for the aluminium applicator inside the PMMA phantom. The pulse duration is 4 µs and the maximun peak beam current is 120 mA. The average dose rate is calculated with the repetition frequency of 250 Hz.

Energy (MeV)	**Dose per pulse (Gy)**	**Instantaneous Dose rate (Gy/s)**	**Average Dose Rate (Gy/s)**
7	20.3	5.08×10^6	5068

6.5.1.2 Aluminum with Water phantom

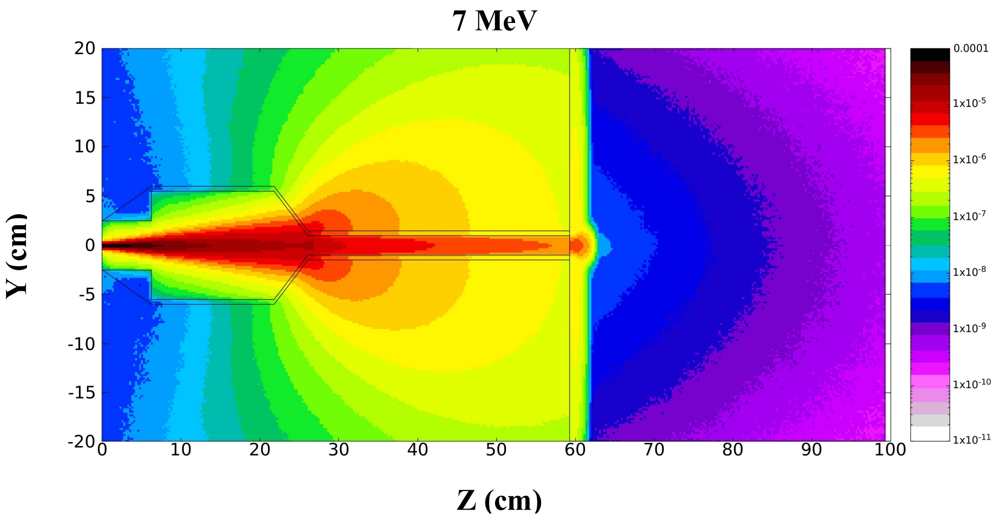

Figure 51. 2D dose distribution for 7 MeV electrons beam for the aluminum applicator inside a 40x40x40 cm^3 Water phantom.

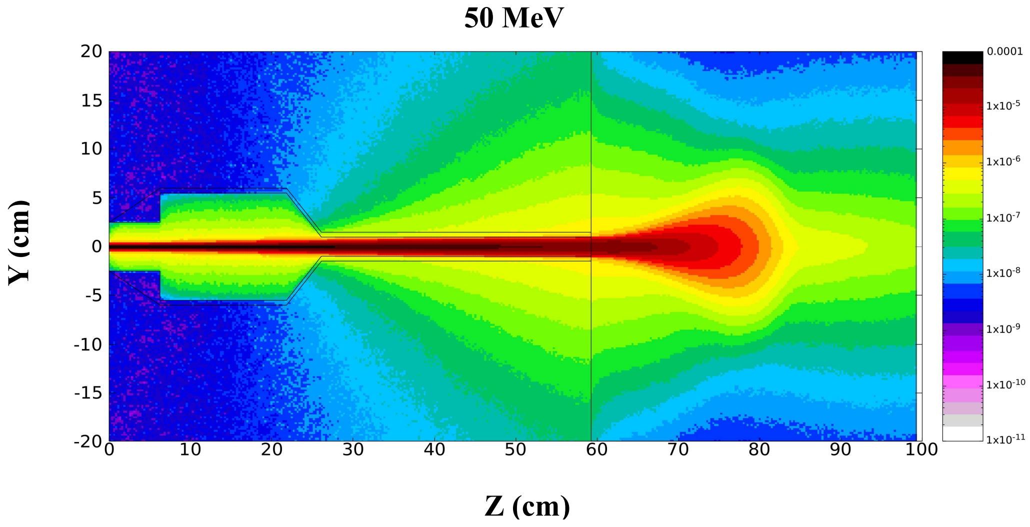

Figure 52. 2D dose distribution for 50 MeV electrons beam for the aluminum applicator inside a 40x40x40 cm^3 Water phantom.

Dose in water for the aluminium applicator is $4.29 \times 10^{-5} \frac{GeV}{g}$ for the 7 MeV and $9.38 \times 10^{-4} \frac{GeV}{g}$ for the 50 MeV electron beam both with uncertainty below 1 %. Dose is bigger in the water than the PMMA phantom, as predicted in the previous chapters.

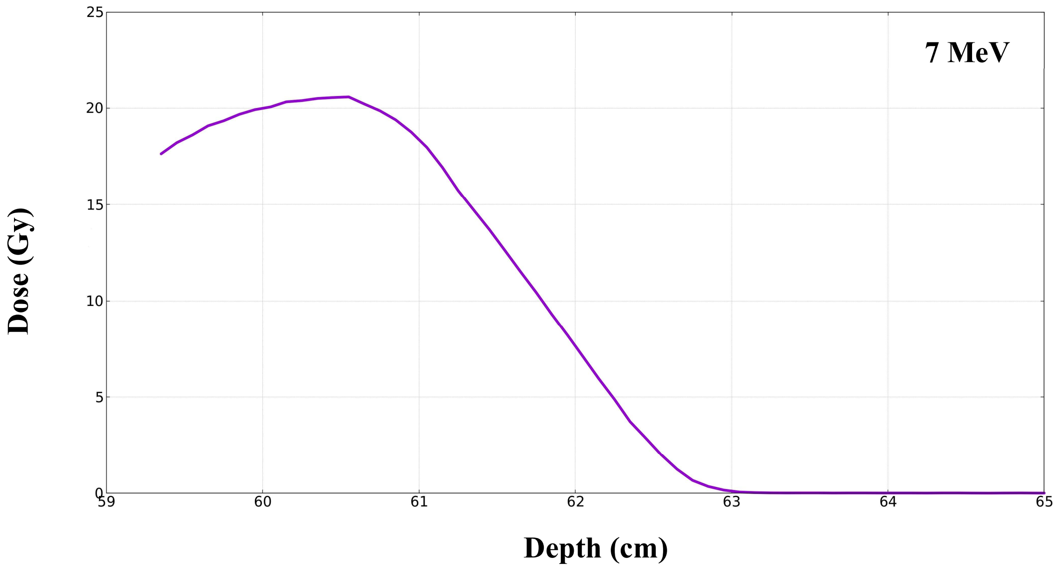

Figure 53. Dose to Depth curve obtained for the 7 MeV electrons beam for the aluminum applicator inside a 40x40x40 cm^3 Water phantom.

The following table (Table 12) reports the measured dose and calculated dose parameters for the flash effect for the aluminium applicator inside the water phantom, which is in good agreement with the flash conditions.

Table 12. Dose per pulse, instanteneous dose rate and average dose rate measurments, obtained for the 7 MeV electrons beam for the aluminium applicator inside the Water phantom. The pulse duration is 4 μs and the maximun peak beam current is 120 mA. The average dose rate is calculated with the repetition frequency of 250 Hz.

Energy (MeV)	Dose per pulse (Gy)	Instantaneous Dose rate (Gy/s)	Average Dose Rate (Gy/s)
7	20.6	5.15×10^6	5150

6.5.2 Copper

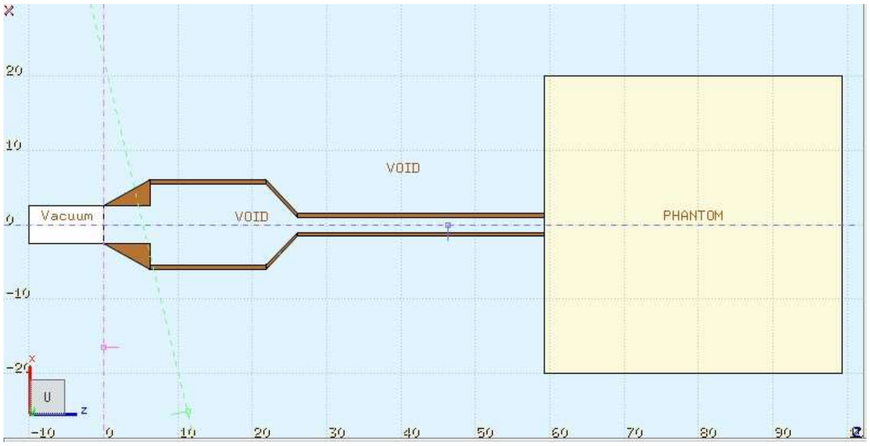

Figure 54. Two-dimensional visualization of FLUKA simulation geometry for the aluminium applicator. The beam travels in the z direction.

6.5.2.1 Copper with PMMA phantom

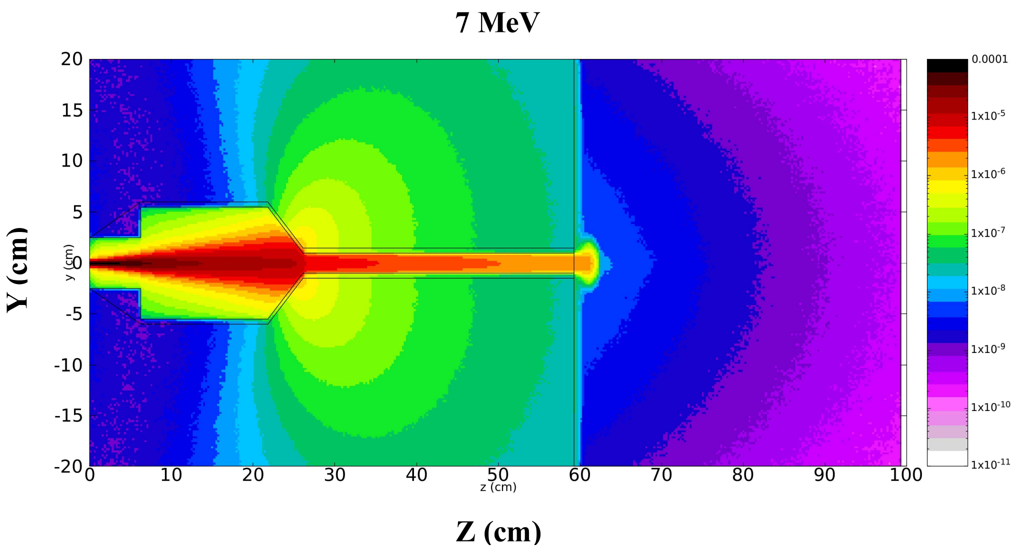

Figure 55. 2D dose distribution for 7 MeV electrons beam for the copper applicator inside a 40x40x40 cm^3 PMMA phantom.

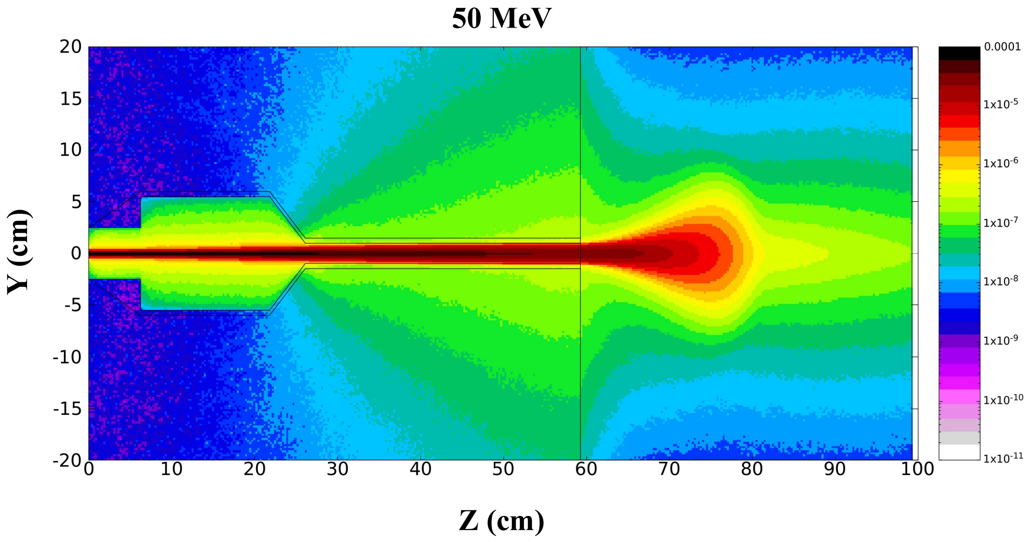

Figure 56. 2D dose distribution for 50 MeV electrons beam for the copper applicator inside a 40x40x40 cm^3 PMMA phantom.

The measured dose at the central axis of the beam in the phantom is 4.08 x $10^{-5}\,\frac{GeV}{g}$ for the 7 MeV and 9.06 x $10^{-4}\,\frac{GeV}{g}$ for the 50 MeV for the copper applicator, which is lower than that of the PMMA applicator for the 7 MeV beam and bigger for the 50

MeV beam (4.31 x $10^{-5}\frac{GeV}{g}$ for the 7 MeV and 8.95 x $10^{-4}\frac{GeV}{g}$ for the 50 MeV for the PMMA applicator). All dose measurements have uncertainty below 1%.

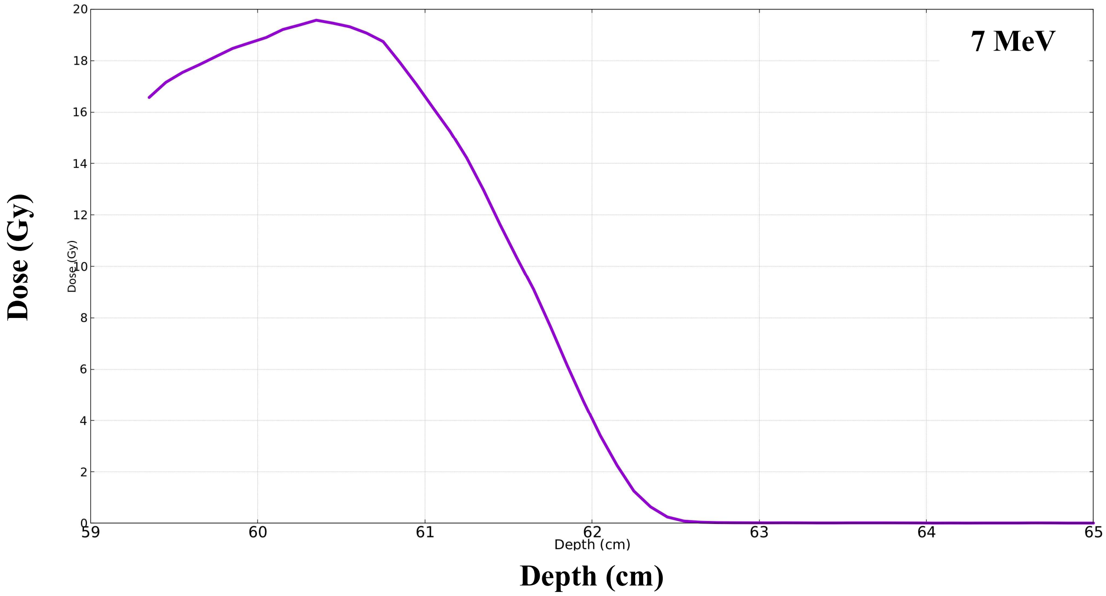

Figure 57. Depth to Dose curve obtained for the 7 MeV electrons beam for the copper applicator inside a 40x40x40 cm³ PMMA phantom.

We notice that all dose parameter calculations for the copper applicator (Table 13), agree with flash effect conditions.

Table 13. Dose per pulse, instanteneous dose rate and average dose rate measurments, obtained for the 7 MeV electrons beam for the copper applicator inside the PMMA phantom. The pulse duration is 4 μs and the maximun peak beam current is 120 mA. The average dose rate is calculated with the repetition frequency of 250 Hz.

Energy (MeV)	Dose per pulse (Gy)	Instantaneous Dose rate (Gy/s)	Average Dose Rate (Gy/s)
7	19.6	4.90 x 10^6	4900

6.5.2.2 Copper with Water phantom

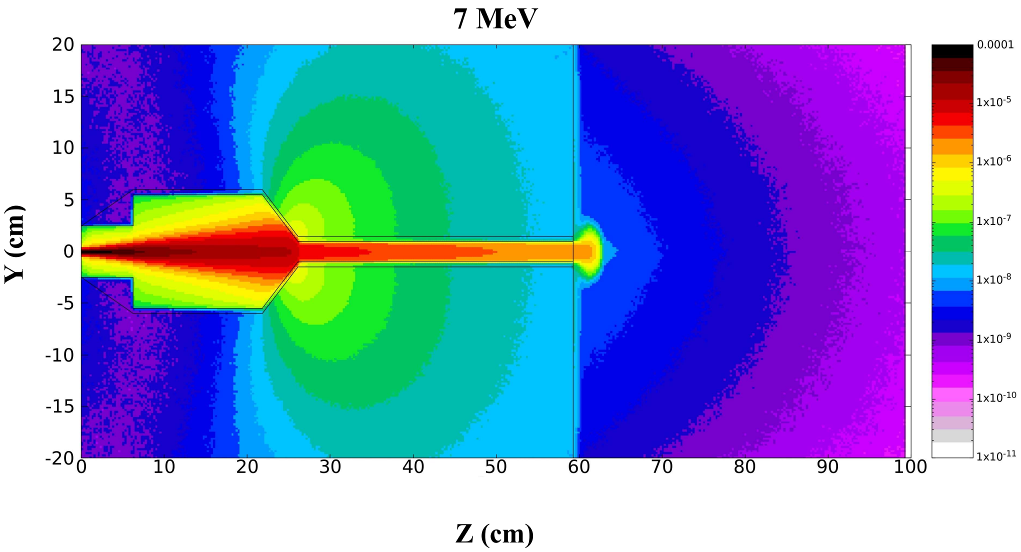

Figure 58. 2D dose distribution for 7 MeV electrons beam for the copper applicator inside a 40x40x40 cm^3 Water phantom.

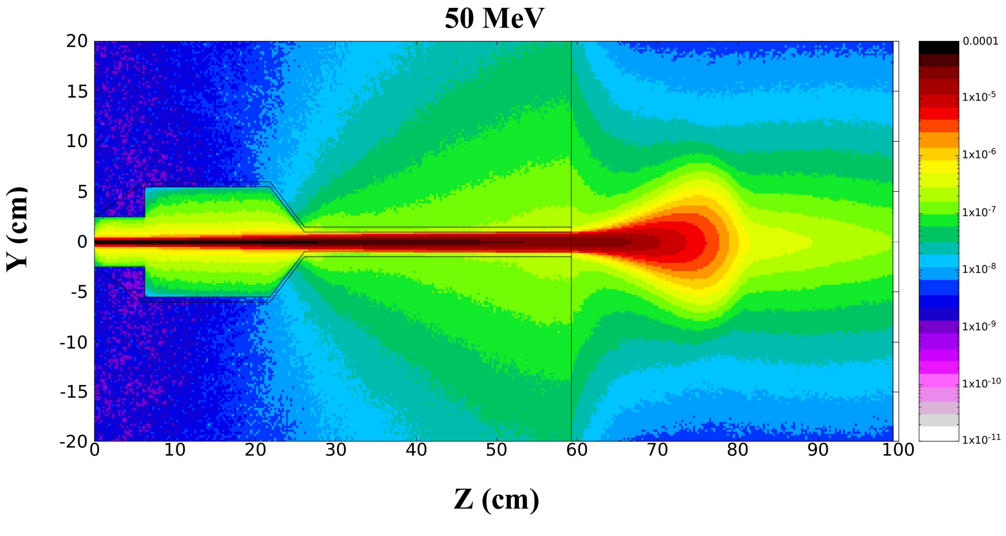

Figure 59. 2D dose distribution for 50 MeV electrons beam for the copper applicator inside a 40x40x40 cm^3 Water phantom.

Dose in water for the copper applicator is 4.15 x $10^{-5}\frac{GeV}{g}$ for the 7 MeV and 9.38 x $10^{-4}\frac{GeV}{g}$ for the 50 MeV electron beam both with uncertainty below 1 %. Dose is bigger in the water than the PMMA phantom, as predicted in the previous chapters.

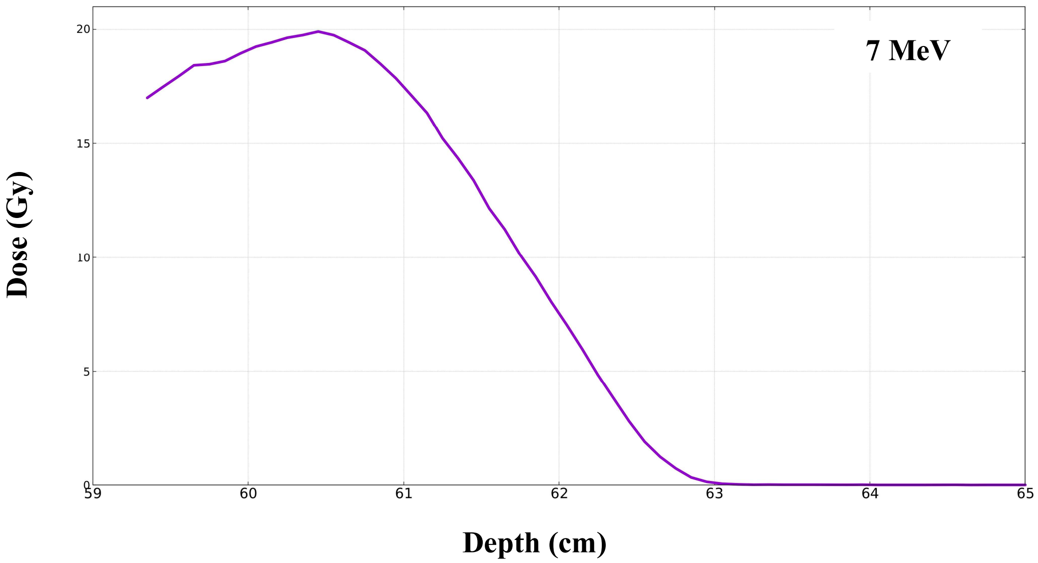

Figure 60. Depth to Dose curve obtained for the 7 MeV electrons beam for the copper applicator inside a 40x40x40 cm^3 Water phantom.

We notice that all dose parameter calculations for the copper applicator (Table 14), agree with flash effect conditions.

Table 14. Dose per pulse, instanteneous dose rate and average dose rate measurments, obtained for the 7 MeV electrons beam for the copper applicator inside the Water phantom. The pulse duration is 4 µs and the maximun peak beam current is 120 mA. The average dose rate is calculated with the repetition frequency of 250 Hz.

Energy (MeV)	**Dose per pulse (Gy)**	**Instantaneous Dose rate (Gy/s)**	**Average Dose Rate (Gy/s)**
7	19.9	4.98 x 10^6	4975

6.5.3 Iron

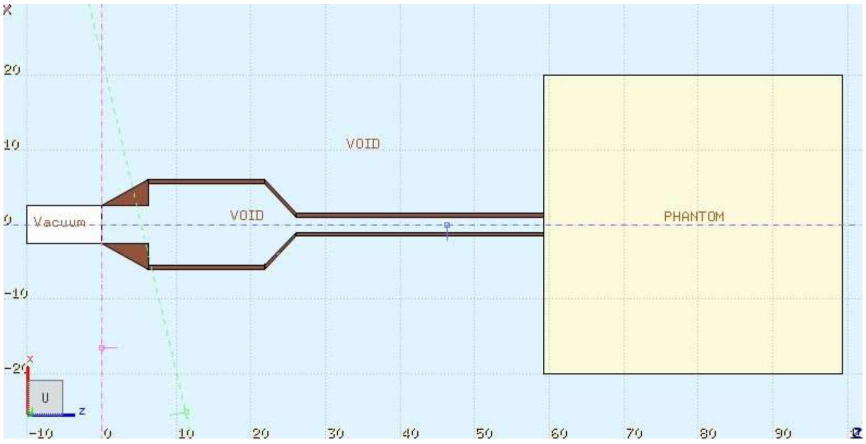

Figure 61. Two-dimensional visualization of FLUKA simulation geometry for the iron applicator. The beam travels in the z direction.

6.5.3.1 Iron with PMMA phantom

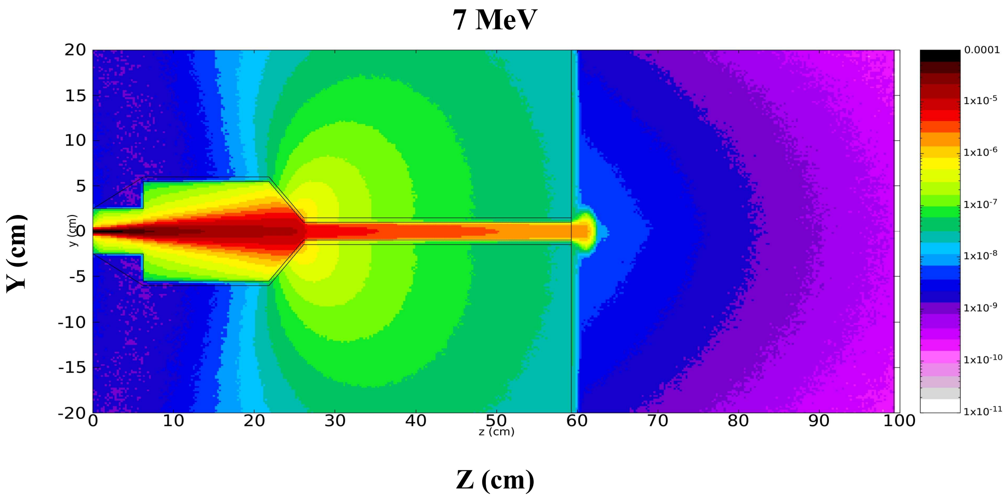

Figure 62. 2D dose distribution for 7 MeV electrons beam for the iron applicator inside a 40x40x40 cm^3 PMMA phantom.

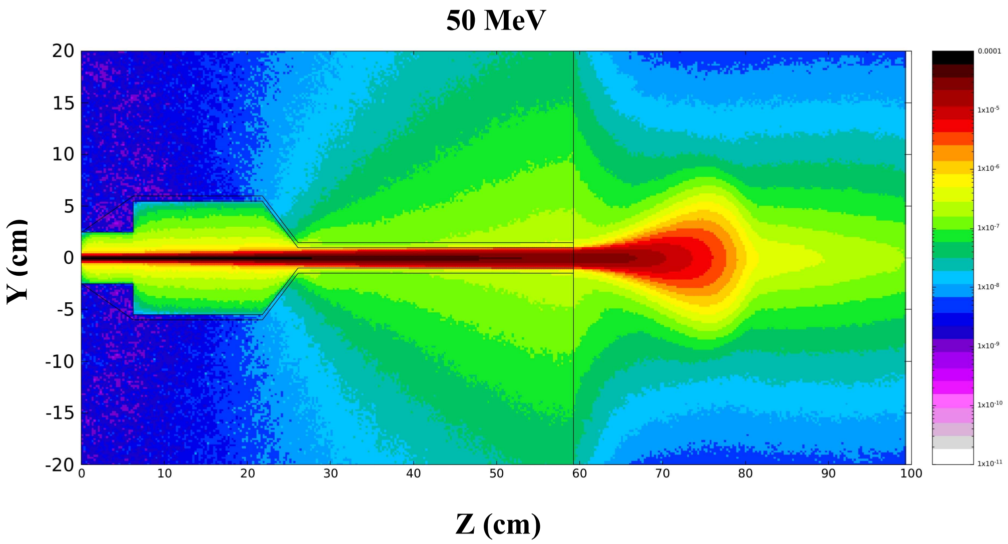

Figure 63. 2D dose distribution for 50 MeV electrons beam for the iron applicator inside a 40x40x40 cm^3 PMMA phantom.

The measured dose at the central axis of the beam in the phantom is 4.08 x $10^{-5}\frac{GeV}{g}$ for the 7 MeV and 9.10 x $10^{-4}\frac{GeV}{g}$ for the 50 MeV for the iron applicator, which is lower than that of the PMMA applicator for the 7 MeV beam and bigger for the 50 MeV beam (4.31 x $10^{-5}\frac{GeV}{g}$ for the 7 MeV and 8.95 x $10^{-4}\frac{GeV}{g}$ for the 50 MeV for the PMMA applicator). All dose measurements have uncertainty below 1%. In addition to this, copper and iron exhibit substantial similarities owing to their similar atomic numbers ($Z = 29$ for copper and $Z = 26$ for iron). This likeness is particularly evident when considering the 7 MeV electron beam, where the measurements are identical.

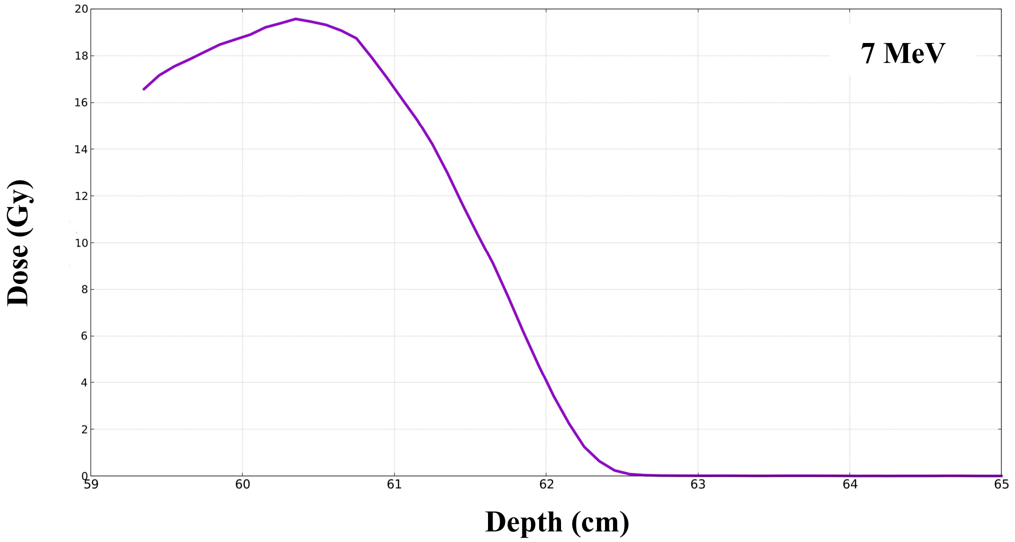

Figure 64. Dose to Depth curve obtained for the 7 MeV electrons beam for the iron applicator inside a 40x40x40 cm^3 PMMA phantom.

We observe that all the calculations of dose parameters for the iron applicator inside a PMMA phantom (as shown in Table 15) align with the conditions associated with the flash effect.

Table 15. Dose per pulse, instanteneous dose rate and average dose rate measurments, obtained for the 7 MeV electrons beam for the iron applicator inside the PMMA phantom. The pulse duration is 4 µs and the maximun peak beam current is 120 mA. The average dose rate is calculated with the repetition frequency of 250 Hz.

Energy (MeV)	**Dose per pulse (Gy)**	**Instantaneous Dose rate (Gy/s)**	**Average Dose Rate (Gy/s)**
7	19.6	4.90×10^6	4900

6.5.3.2 Iron with Water phantom

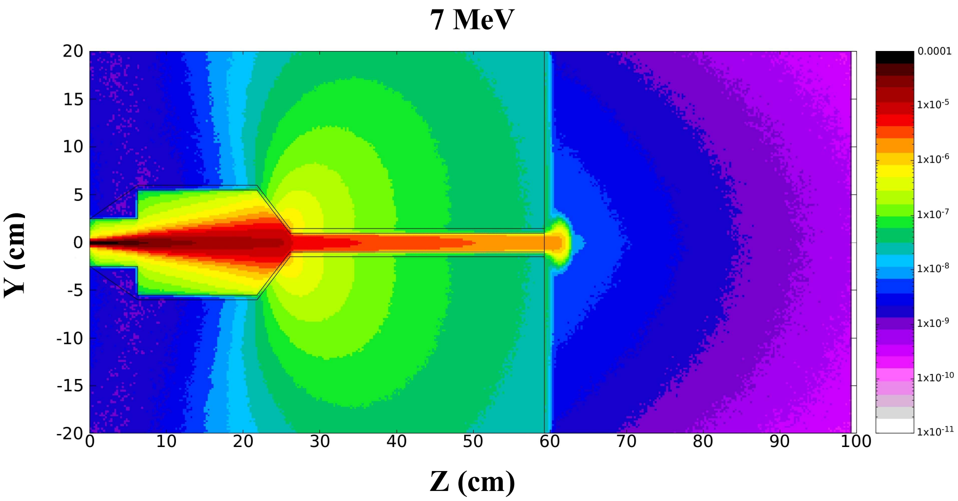

Figure 65. 2D dose distribution for 7 MeV electrons beam for the iron applicator inside a 40x40x40 cm^3 Water phantom.

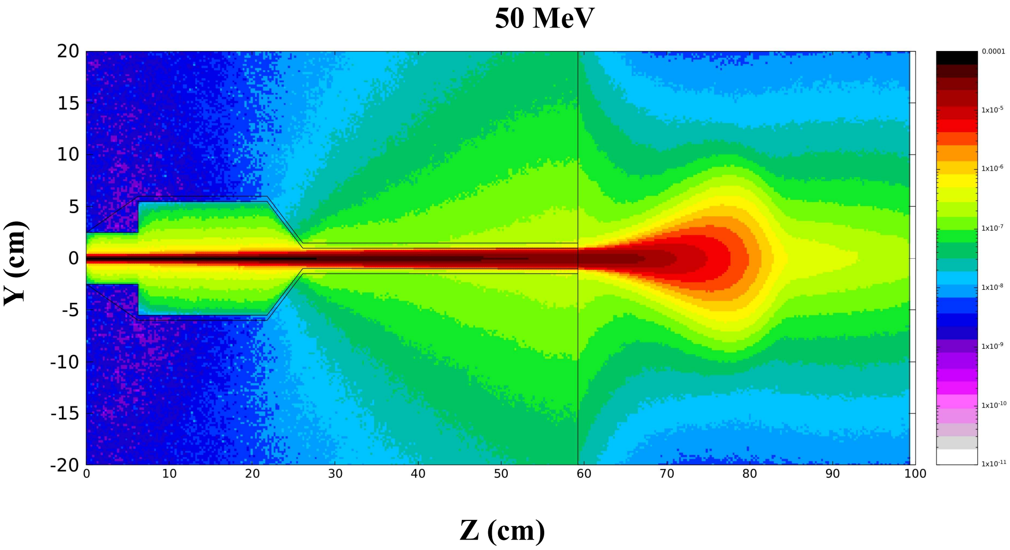

Figure 66. 2D dose distribution for 50 MeV electrons beam for the iron applicator inside a 40x40x40 cm^3 Water phantom.

Dose in water for the iron applicator is 4.15 x $10^{-5}\frac{GeV}{g}$ for the 7 MeV and 9.32 x 10^{-4} $\frac{GeV}{g}$ for the 50 MeV electron beam both with uncertainty below 1 %. Dose is bigger in the water than the PMMA phantom, as predicted in the previous chapters. Once again, we can note that copper and iron within the water phantom display comparable dose measurements, with the exact same measurement for the 7 MeV electron beam.

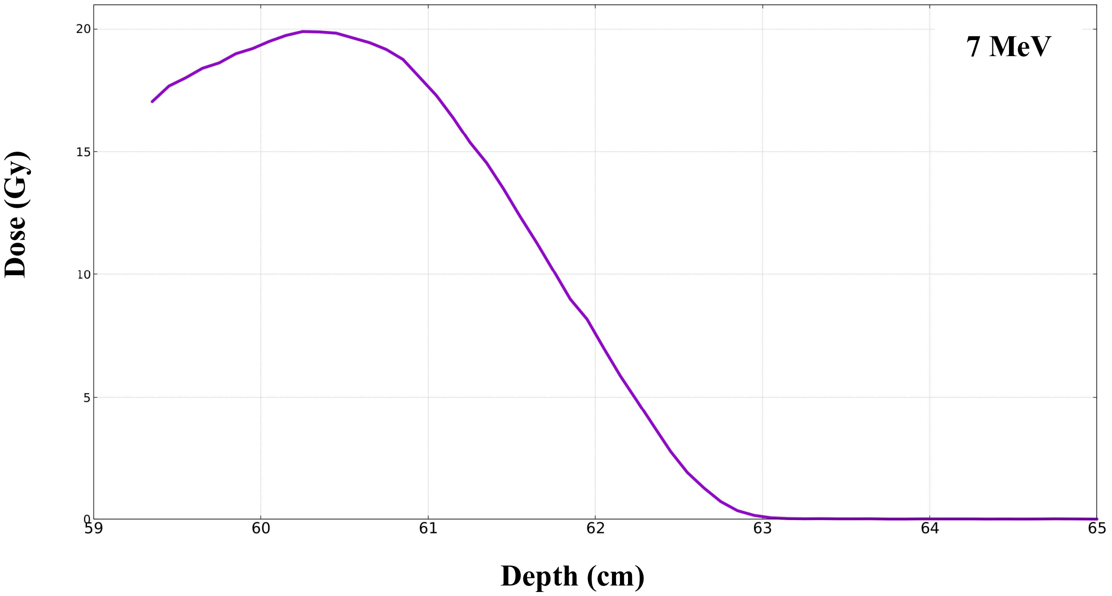

Figure 67. Dose to Depth curve obtained for the 7 MeV electrons beam for the iron applicator inside a 40x40x40 cm^3 Water phantom.

We observe that all the calculations of dose parameters for the iron applicator inside a water phantom (as shown in Table 16) align with the conditions associated with the flash effect.

Table 16. Dose per pulse, instanteneous dose rate and average dose rate measurments, obtained for the 7 MeV electrons beam for the iron applicator inside the Water phantom. The pulse duration is 4 µs and the maximun peak beam current is 120 mA. The average dose rate is calculated with the repetition frequency of 250 Hz.

Energy (MeV)	**Dose per pulse (Gy)**	**Instantaneous Dose rate (Gy/s)**	**Average Dose Rate (Gy/s)**
7	19.9	4.98×10^6	4975

From the 2D dose distribution plots for all the applicator materials, it can be deduced that, the selection of materials with higher atomic numbers for the electron applicator can lead to the creation of a more collimated beam.

Also, the Dose to Depth and PDD figures of the central axis of the beam revealed no significant differences, despite alternations made to the applicator materials.

In the following plots we study how changes in applicator materials affect the dose distribution within the entire treatment field.

Capturing how dose changes occur not only along the central axis but also across the entire treatment field, is especially significant when changing applicator materials as it can influence scatter and attenuation patterns. By making these plots we can obtain how these changes impact dose penetration, dose build-up and dose fall off within the entire phantom. We can also ensure that dose delivery remains consistent and predictable throughout the treatment field.

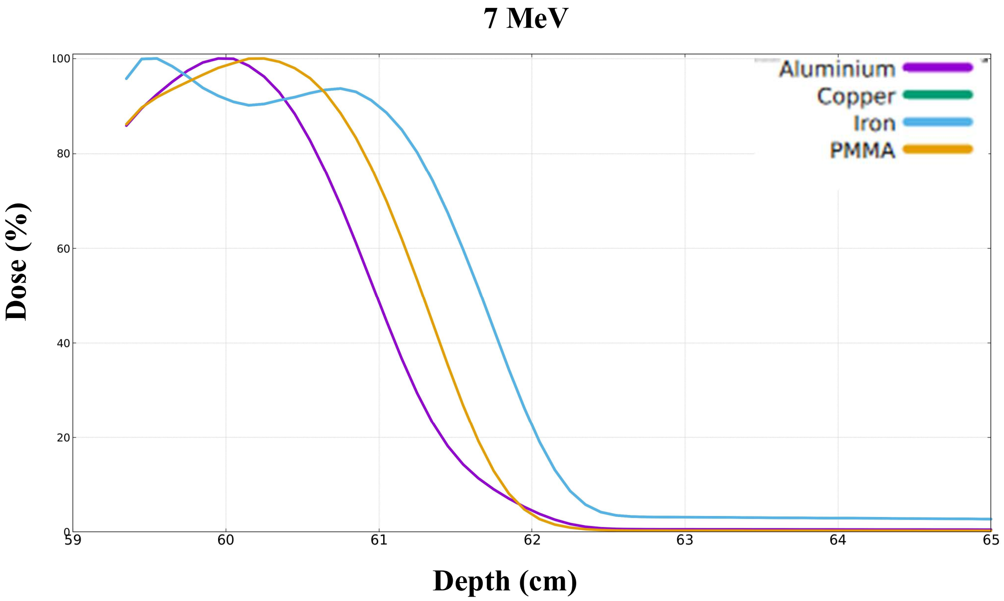

Figure 68. Comparative figure of dose distribution across the whole phantom for a 7 MeV electrons beam inside 40x40x40 cm^3 PMMA phantom, for the aluminium (purple line), copper (green line), iron (blue line) and PMMA (orange line) applicator. Copper and Iron appear to have the same plots (blue line) due to their close atomic number.

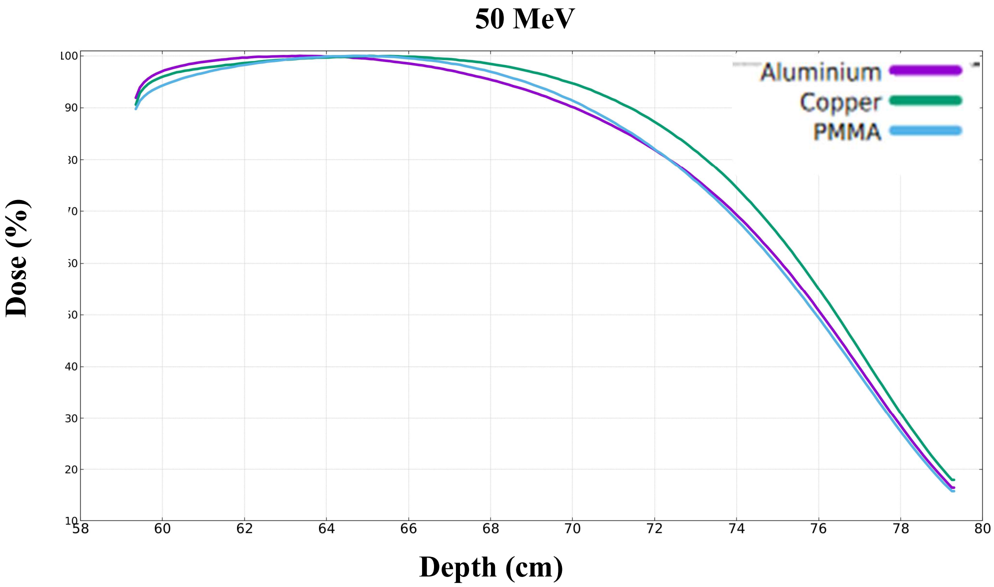

Figure 69. Comparative figure of dose distribution across the whole phantom for a 50 MeV electrons beam inside a 40x40x40 cm^3 PMMA phantom, for the aluminium (purple line), copper and iron (both in green line) and PMMA (blue line) applicator.

Following figures (Figure 69, 70, 71 and 72) present the dose profiles of the 7 and 50 MeV electron beams for different applicator materials for both PMMA and water phantoms. The main difference is that in heavier materials the curve drops closer to 0 %.

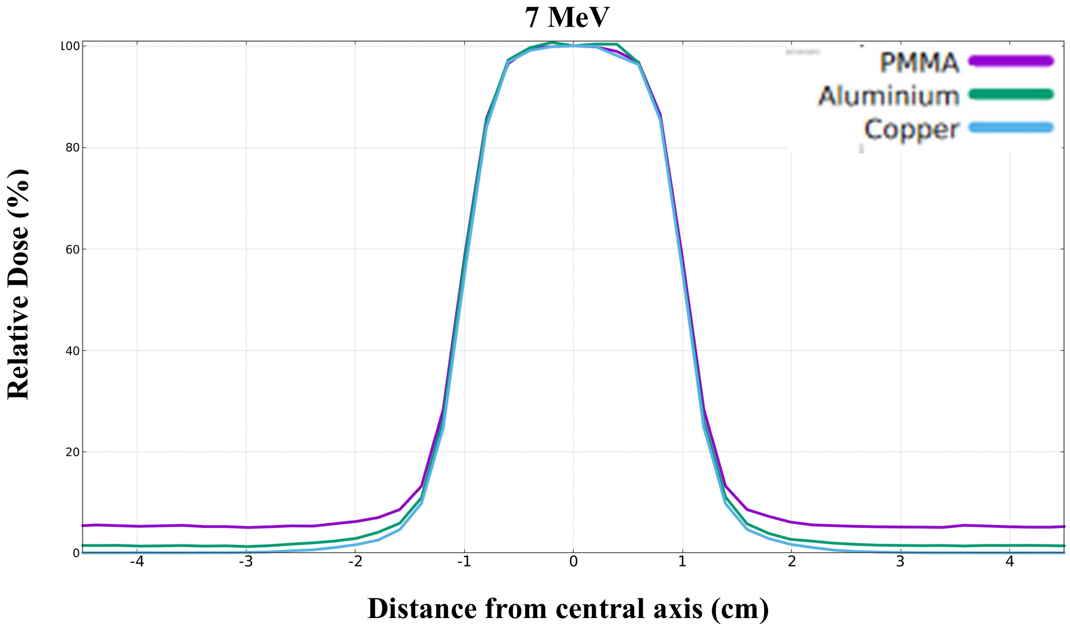

Figure 70. Comparative plot of the dose profile in the PMMA phantom obtained for the PMMA (purple line), Aluminium (green line), Copper and Iron (both in blue line) applicator.

The figure shows the profiles obtained at the depth of maximun dose value (R100) for a 7 MeV electron beam.

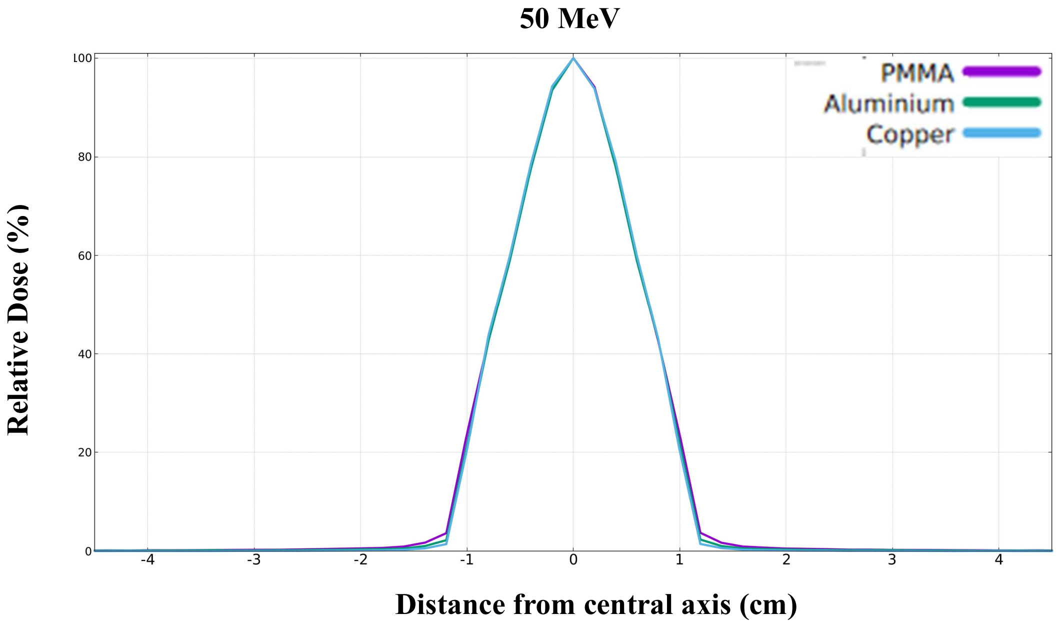

Figure 71. Comparative plot of the dose profile in the PMMA phantom obtained for the PMMA (purple line), Aluminium (green line), Copper and iron (both in blue line) applicator. The figure shows the profiles obtained at the depth of maximun dose value (R100) for a 50 MeV electron beam.

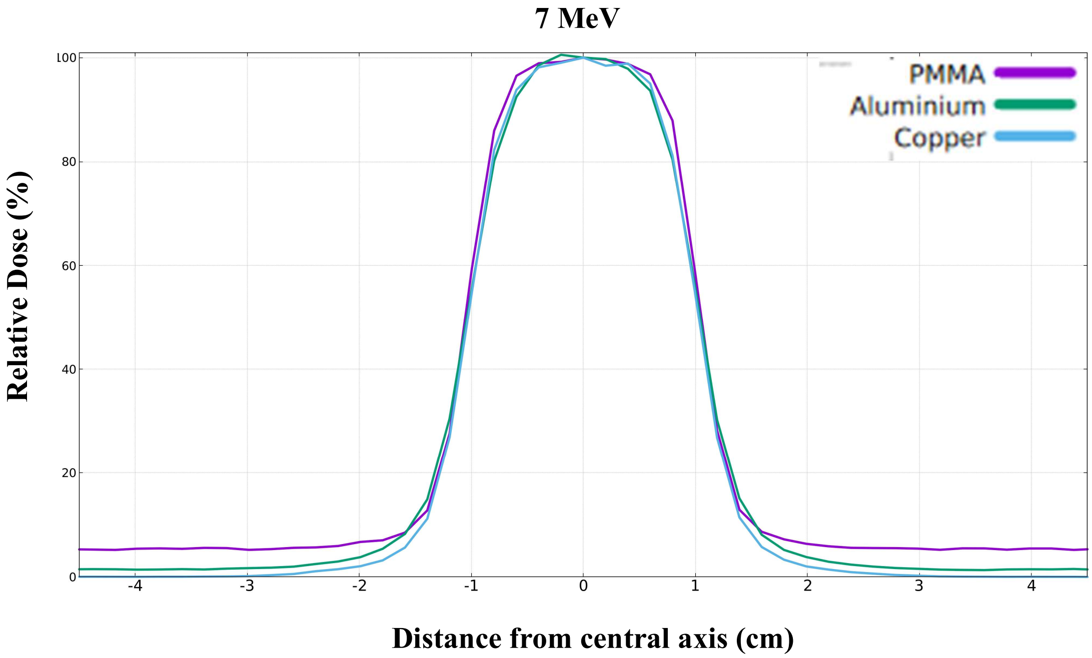

Figure 72. Comparative plot of the dose profile in the Water phantom obtained for the PMMA (purple line), Aluminium (green line), Copper and iron (both in blue line) applicator. The figure shows the profiles obtained at the depth of maximun dose value (R100) for a 7 MeV electron beam.

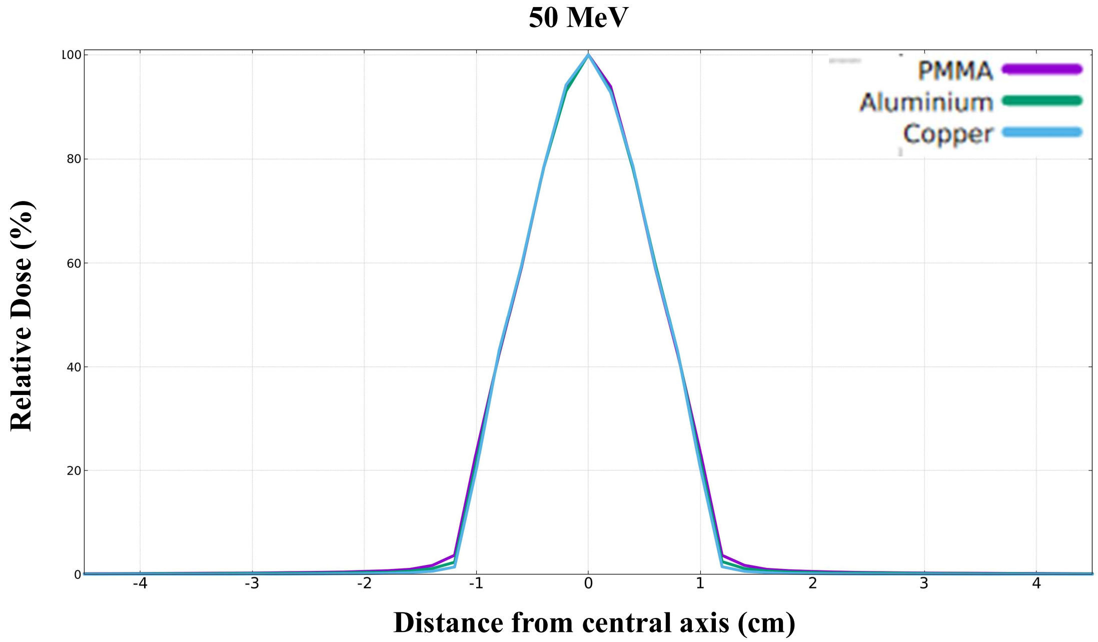

Figure 73. Comparative plot of the dose profile in the Water phantom obtained for the PMMA (purple line), Aluminium (green line), Copper and Iron (both in blue line) applicator. The figure shows the profiles obtained at the depth of maximun dose value (R100) for a 50 MeV electrons beam.

In the subsequent tables (Tables 17, 18, 19 and 20), all the valuable data collected in this research about Flash RT are presented, both before and after normalization.

Table 17. Flash effect conditions for all applicator materials inside the PMMA and Water phantom for the 7 ***MeV*** *electrons beam.*

Materials		**Dose per pulse (Gy)**	**Instantaneous Dose Rate (Gy/s)**	**Average Dose Rate (Gy/s)**
Applicator	**Phantom**			
PMMA	**PMMA**	20.7	5.18×10^{6}	5175
Aluminium	**PMMA**	20.3	5.08×10^{6}	5068
Copper	**PMMA**	19.6	4.90×10^{6}	4900
Iron	**PMMA**	19.6	4.90×10^{6}	4900
PMMA	**Water**	21.0	5.25×10^{6}	5250
Aluminium	**Water**	20.6	5.15×10^{6}	5150
Copper	**Water**	19.9	4.98×10^{6}	4975
Iron	**Water**	19.9	4.98×10^{6}	4975

Table 18. Measurements of the maximum dose of the central axis of vthe beam for different materials inside a 40x40x40 cm^{3} *PMMA and Water phantom (uncertainty below 1 %), without any process of the data (output of dose scoring in Fluka).*

Materials		**Max. Dose ($\frac{GeV}{g}$)**	
Applicator	**Phantom**	**7 MeV**	**50 MeV**
PMMA	**PMMA**	4.31×10^{-5}	8.95×10^{-4}
Aluminium	**PMMA**	4.22×10^{-5}	9.05×10^{-4}
Copper	**PMMA**	4.08×10^{-5}	9.06×10^{-4}
Iron	**PMMA**	4.08×10^{-5}	9.10×10^{-4}
PMMA	**Water**	4.38×10^{-5}	9.23×10^{-4}
Aluminium	**Water**	4.29×10^{-5}	9.38×10^{-4}
Copper	**Water**	4.15×10^{-5}	9.38×10^{-4}
Iron	**Water**	4.15×10^{-5}	9.32×10^{-4}

Table 19. Flash effect conditions for all applicator geometries inside the PMMA phantom for the 7 ***MeV*** *electrons beam.*

Applicator Geometry	Dose per pulse (Gy)	Instantaneous Dose Rate (Gy/s)	Average Dose Rate (Gy/s)
A-1	20.7	5.18×10^6	5175
A-2	20.3	5.08×10^6	5075
A-3	17.6	4.40×10^6	4400

Table 20. Measurements of the maximum dose for different applicator geometries inside a PMMA 40x40x40 cm^3 phantom (uncertainty below 1% , without any process of the data (output of dose scoring in Fluka).

Applicator Geometry	Max. Dose ($\frac{GeV}{g}$)	
	7 MeV	**50 MeV**
A - 1	4.31×10^{-5}	8.95×10^{-4}
A - 2	4.22×10^{-5}	8.97×10^{-4}
A - 3	3.66×10^{-5}	8.71×10^{-4}

7. Conclusions

In this study, the electron Flash effect was investigated, using the Fluka simulation package. We explored this phenomenon across a range of electron beam energies and examined the impact of different beam applicators, each with varying material compositions and geometries, with the primary aim of identifying the optimal electron beam characteristics for cancer treatment.

Dose and beam characteristics were calculated for different electron energies (5, 7, 9, 50, 100 MeV) in both PMMA and water phantoms by studying the Percentage Depth Dose (PDD) and dose profile plots. Additionally, a comparison between PMMA and water as phantom materials was made, revealing that PMMA shows great similarities with water at all electron energies.

Furthermore, the applicator geometry was altered by changing the diameters of the second and third cylinders. It was observed that altering the diameter of the second cylinder had no noticeable effect on the dose results or beam characteristics. In contrast, when the diameter of the third cylinder was modified, by examining the beam profile plot of the central axis of the beam, a significant improvement in beam flatness was noted, particularly at lower-energy electron beams, but the measured maximum dose was lower than that of the other geometries.

In addition, changes were made to the applicator materials, including aluminium, copper and iron, in order to evaluate the potential effects of different materials on the dose and beam characteristics of an electron beam, once again in both PMMA and water phantoms. It was determined that, for specific cancer treatments, the selection of materials with higher atomic numbers for the electron applicator can lead to the creation of a more collimated beam. Also, in this study iron and copper produced similar results due to their comparable atomic numbers.

It is noteworthy that all obtained results met the requirements of the FLASH conditions, with an average dose rate $\bar{\dot{D}}$ >100 Gy/s, an in-peak dose-rate of $\dot{D}p > 10^6$, a pulse repetition frequency PRF > 100 Hz and an irradiation time $t_i < 100$ ms.

It is recommended that future experimental studies be conducted to validate the simulation outcomes of this research. These additional investigations will contribute to a more comprehensive understanding of the electron FLASH effect and its potential applications in cancer treatment.

8. Bibliography

[1] Gianfaldoni, S., Gianfaldoni, R., Wollina, U., Lotti, J., Tchernev, G. and Lotti, T. (2017). An Overview on Radiotherapy: From Its History to Its Current Applications in Dermatology. *Open Access Macedonian Journal of Medical Sciences*, [online] 5(4), p.521. doi:https://doi.org/10.3889/oamjms.2017.122.

[2] Huh, H.D. and Kim, S. (2020). History of Radiation Therapy Technology. *Progress in Medical Physics*, 31(3), pp.124–134. doi:https://doi.org/10.14316/pmp.2020.31.3.124.

[3] Tian, X., Liu, K., Hou, Y., Cheng, J. and Zhang, J. (2017). The evolution of proton beam therapy: Current and future status (Review). *Molecular and Clinical Oncology*, 8(1). doi:https://doi.org/10.3892/mco.2017.1499.

[4] Gagnebin, S., Twerenbold, D., Pedroni, E., Meer, D., Zenklusen, S. and Bula, C. (2010). Experimental determination of the absorbed dose to water in a scanned proton beam using a water calorimeter and an ionization chamber. *Nuclear Instruments and Methods in Physics Research Section B: Beam Interactions with Materials and Atoms*, [online] 268(5), pp.524–528. doi:https://doi.org/10.1016/j.nimb.2009.11.010.

[5] Varnava, M., Jun-ichi Saitoh, Tashiro, M., Kubo, N., Okano, N., Kawamura, H. and Ohno, T. (2023). Dose–volume constraints for head-and-neck cancer in carbon ion radiotherapy: A literature review. 12(7), pp.8267–8277. doi:https://doi.org/10.1002/cam4.5641.

[6] Mohamad, O., Sishc, B.J., Saha, J., Pompos, A., Rahimi, A., Story, M.D., Davis, A.J. and Kim, D.W.N. (2017). Carbon Ion Radiotherapy: A Review of Clinical Experiences and Preclinical Research, with an Emphasis on DNA Damage/Repair. *Cancers*, [online] 9(6), p.E66. doi:https://doi.org/10.3390/cancers9060066.

[7] Debowski M, Murphy A, Jones J, et al. Electron therapy. Reference article, Radiopaedia.org (Accessed on 23 Jun 2023) https://doi.org/10.53347/rID-67623

[8] Kokurewicz, K., Brunetti, E., Welsh, G.H., Wiggins, S.M., Boyd, M., Sorensen, A., Chalmers, A.J., Schettino, G., Subiel, A., DesRosiers, C. and Jaroszynski, D.A. (2019). Focused very high-energy electron beams as a novel radiotherapy modality for producing high-dose volumetric elements. *Scientific Reports*, 9(1). doi:https://doi.org/10.1038/s41598-019-46630-w.

[9] Kaiser, A., Eley, J.G., Onyeuku, N.E., Rice, S.R., Wright, C.C., McGovern, N.E., Sank, M., Zhu, M., Vujaskovic, Z., Simone, C.B. and Hussain, A. (2019). Proton Therapy Delivery and Its Clinical Application in Select Solid Tumor Malignancies. *Journal of Visualized Experiments*, (144). doi:https://doi.org/10.3791/58372.

[10] Giuliano, L., Franciosini, G., Palumbo, L., Aggar, L., Dutreix, M., Faillace, L., Favaudon, V., Felici, G., Galante, F., Mostacci, A., Migliorati, M., Pacitti, M., Patriarca, A. and Heinrich, S. (2023). Characterization of Ultra-High-Dose Rate Electron Beams with ElectronFlash Linac. *Applied Sciences*, [online] 13(1), p.631. doi:https://doi.org/10.3390/app13010631.

[11] Montay-Gruel, P., Petersson, K., Jaccard, M., Boivin, G., Germond, J.-F., Petit, B., Doenlen, R., Favaudon, V., François Bochud, Bailat, C., Bourhis, J. and Marie-Catherine Vozenin (2017). Irradiation in a flash: Unique sparing of memory in mice after whole brain irradiation with dose rates above 100 Gy/s. 124(3), pp.365–369. doi:https://doi.org/10.1016/j.radonc.2017.05.003.

[12] Halloran, A. (2015). *LSU Digital Commons Dosimetric Advantages of Personalized Phantoms for Quality Assurance and Research in Radiation Dose Measurements*. [online] Available at: https://digitalcommons.lsu.edu/cgi/viewcontent.cgi?article=2226&context=gradschool_theses

[13] Yadav, N., Singh, M. and Mishra, S.P. (2021). Tissue-equivalent materials used to develop phantoms in radiation dosimetry: A review. *Materials Today: Proceedings*. doi:https://doi.org/10.1016/j.matpr.2021.06.359.

[14] INTERNATIONAL ATOMIC ENERGY AGENCY (2000). *Absorbed Dose Determination in External Beam Radiotherapy An International Code of Practice for Dosimetry Based on Standards of Absorbed Dose to Water*. [online] Vienna. Available at: https://www-pub.iaea.org/MTCD/Publications/PDF/TRS398_scr.pdf.

[15] Strydom, W., Parker, W. and Olivares, M. (n.d.). *Chapter 8 ELECTRON BEAMS: PHYSICAL AND CLINICAL ASPECTS*. [online] Available at: http://www-naweb.iaea.org/nahu/DMRP/documents/Chapter8.pdf.

[16] Podgorsak, E. (n.d.). Chapter 8: Electron Beams: Physical and Clinical Aspects Slide set prepared in 2006. [online] Available at: https://www-naweb.iaea.org/nahu/DMRP/documents/slides/Chapter_08_Electron_beams.pdf.

[17] Raychaudhuri, S. (n.d.). *INTRODUCTION TO MONTE CARLO SIMULATION*. [online] Available at: https://www.informs-sim.org/wsc08papers/012.pdf.

[18] fluka.cern. (n.d.). *About FLUKA | The official CERN FLUKA website*. [online] Available at: https://fluka.cern/about.

[19] fluka.cern. (n.d.). *The Flair Graphical User Interface | The official CERN FLUKA website*. [online] Available at: https://fluka.cern/documentation/running/flair-gui [Accessed 25 Aug. 2023].

Appendix I

Input file for the A-1 applicator using flair.

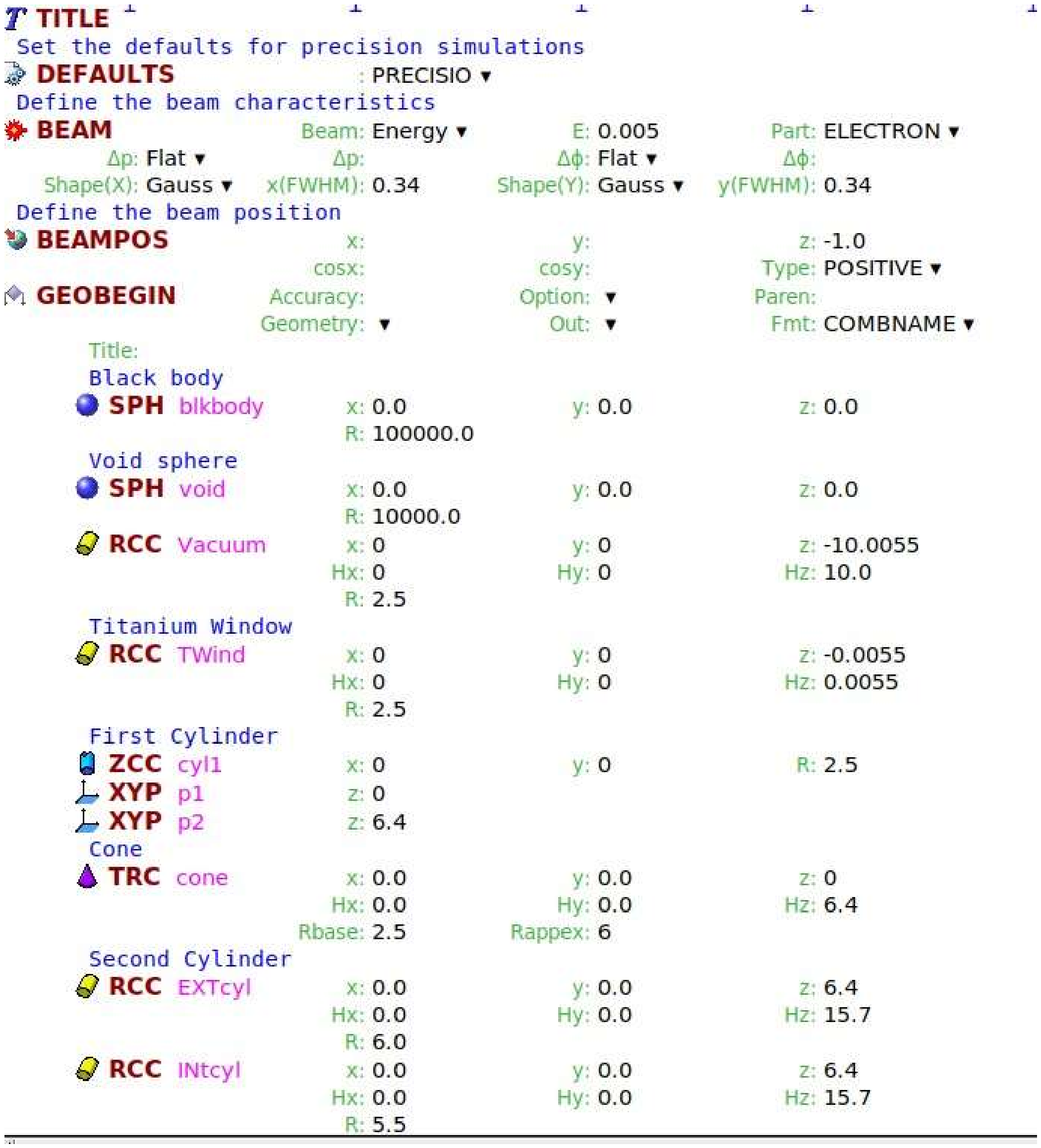

```
TITLE
 Set the defaults for precision simulations
DEFAULTS                          : PRECISIO ▾
 Define the beam characteristics
BEAM               Beam: Energy ▾         E: 0.005         Part: ELECTRON ▾
          Δp: Flat ▾         Δp:          Δϕ: Flat ▾         Δϕ:
    Shape(X): Gauss ▾  x(FWHM): 0.34   Shape(Y): Gauss ▾  y(FWHM): 0.34
 Define the beam position
BEAMPOS                   x:                 y:                z: -1.0
                       cosx:              cosy:             Type: POSITIVE ▾
GEOBEGIN           Accuracy:            Option: ▾          Paren:
                   Geometry: ▾             Out: ▾            Fmt: COMBNAME ▾
      Title:
      Black body
      SPH  blkbody        x: 0.0             y: 0.0            z: 0.0
                          R: 100000.0
      Void sphere
      SPH  void           x: 0.0             y: 0.0            z: 0.0
                          R: 10000.0
      RCC  Vacuum         x: 0               y: 0              z: -10.0055
                         Hx: 0              Hy: 0             Hz: 10.0
                          R: 2.5
      Titanium Window
      RCC  TWind          x: 0               y: 0              z: -0.0055
                         Hx: 0              Hy: 0             Hz: 0.0055
                          R: 2.5
      First Cylinder
      ZCC  cyl1           x: 0               y: 0              R: 2.5
      XYP  p1             z: 0
      XYP  p2             z: 6.4
      Cone
      TRC  cone           x: 0.0             y: 0.0            z: 0
                         Hx: 0.0            Hy: 0.0           Hz: 6.4
                      Rbase: 2.5        Rappex: 6
      Second Cylinder
      RCC  EXTcyl         x: 0.0             y: 0.0            z: 6.4
                         Hx: 0.0            Hy: 0.0           Hz: 15.7
                          R: 6.0
      RCC  INtcyl         x: 0.0             y: 0.0            z: 6.4
                         Hx: 0.0            Hy: 0.0           Hz: 15.7
                          R: 5.5
```

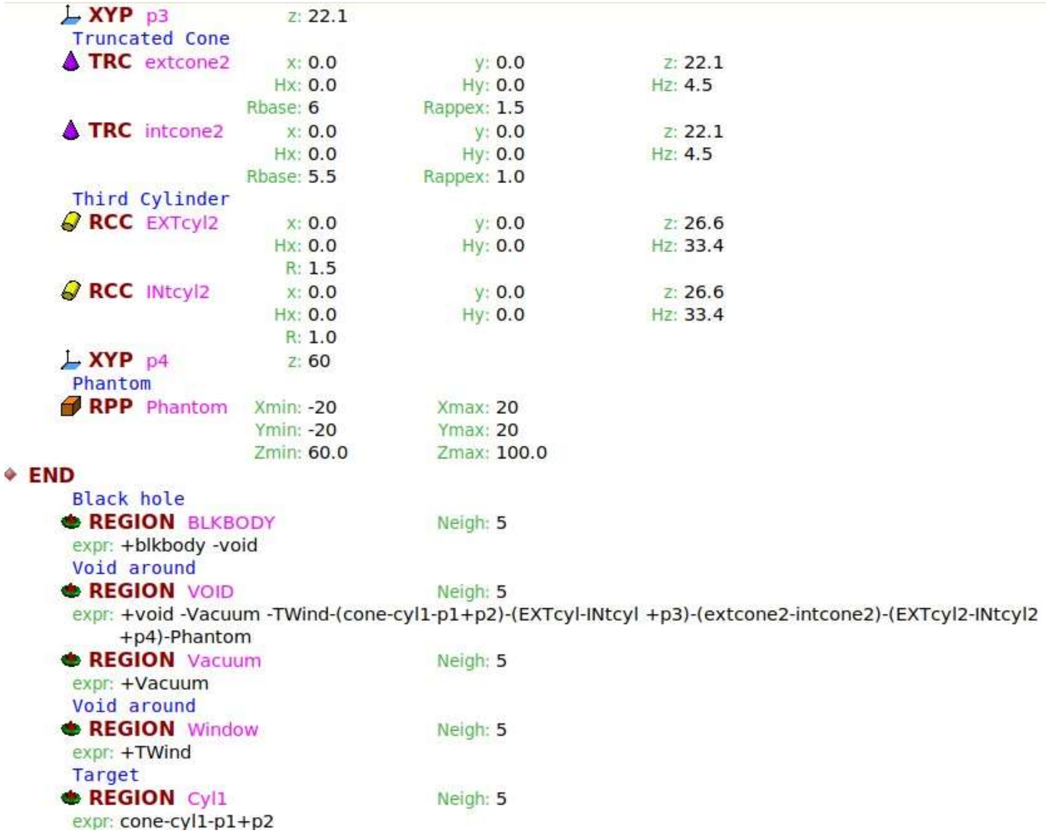

```
    XYP  p3             z: 22.1
    Truncated Cone
    TRC  extcone2       x: 0.0            y: 0.0          z: 22.1
                       Hx: 0.0           Hy: 0.0         Hz: 4.5
                    Rbase: 6         Rappex: 1.5
    TRC  intcone2       x: 0.0            y: 0.0          z: 22.1
                       Hx: 0.0           Hy: 0.0         Hz: 4.5
                    Rbase: 5.5       Rappex: 1.0
    Third Cylinder
    RCC  EXTcyl2        x: 0.0            y: 0.0          z: 26.6
                       Hx: 0.0           Hy: 0.0         Hz: 33.4
                        R: 1.5
    RCC  INtcyl2        x: 0.0            y: 0.0          z: 26.6
                       Hx: 0.0           Hy: 0.0         Hz: 33.4
                        R: 1.0
    XYP  p4             z: 60
    Phantom
    RPP  Phantom     Xmin: -20         Xmax: 20
                     Ymin: -20         Ymax: 20
                     Zmin: 60.0        Zmax: 100.0
END
    Black hole
    REGION BLKBODY                    Neigh: 5
    expr: +blkbody -void
    Void around
    REGION VOID                       Neigh: 5
    expr: +void -Vacuum -TWind-(cone-cyl1-p1+p2)-(EXTcyl-INtcyl +p3)-(extcone2-intcone2)-(EXTcyl2-INtcyl2
          +p4)-Phantom
    REGION Vacuum                     Neigh: 5
    expr: +Vacuum
    Void around
    REGION Window                     Neigh: 5
    expr: +TWind
    Target
    REGION Cyl1                       Neigh: 5
    expr: cone-cyl1-p1+p2
```

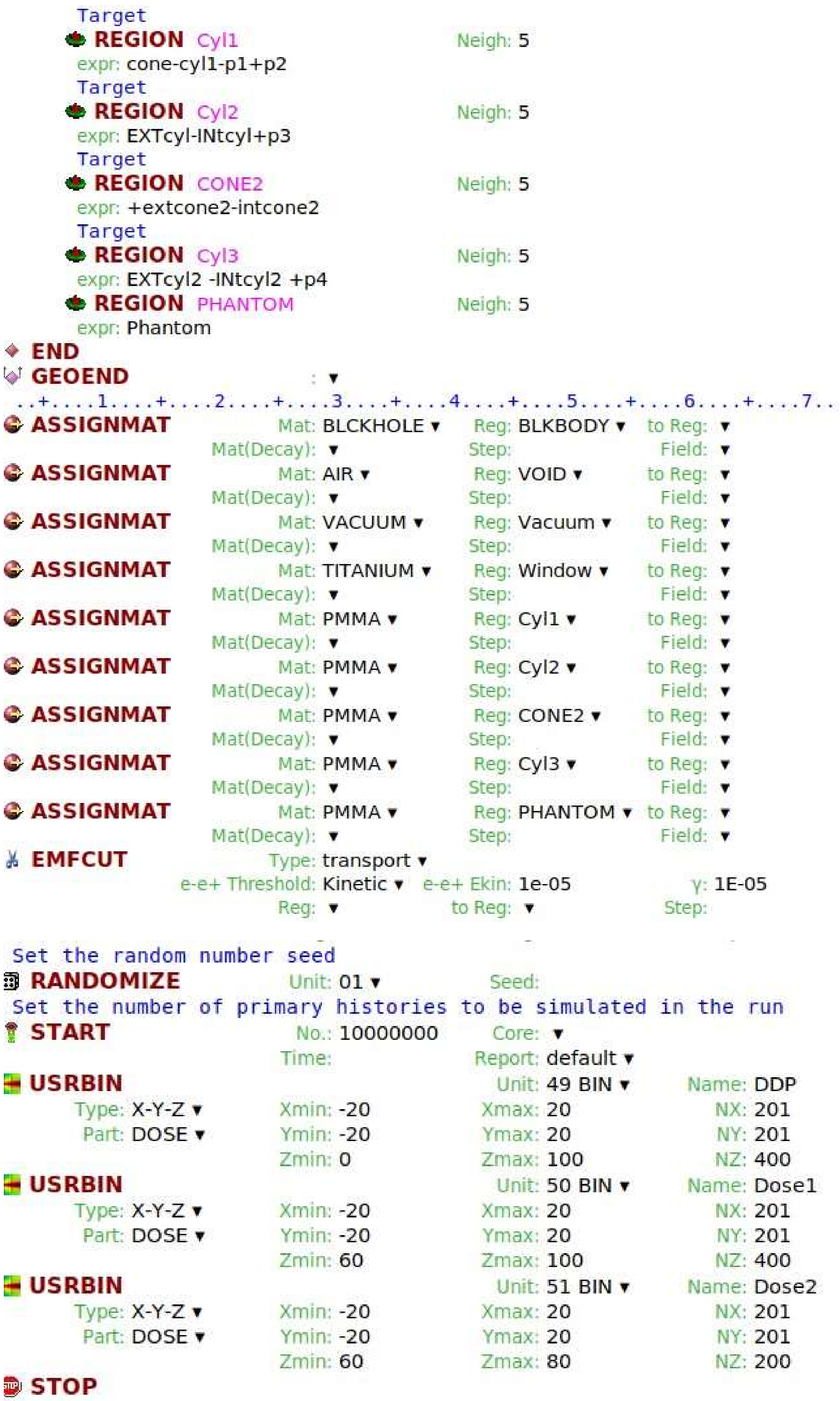

```
      Target
      REGION  Cyl1                     Neigh: 5
      expr: cone-cyl1-p1+p2
      Target
      REGION  Cyl2                     Neigh: 5
      expr: EXTcyl-INtcyl+p3
      Target
      REGION  CONE2                    Neigh: 5
      expr: +extcone2-intcone2
      Target
      REGION  Cyl3                     Neigh: 5
      expr: EXTcyl2 -INtcyl2 +p4
      REGION  PHANTOM                  Neigh: 5
      expr: Phantom
 END
 GEOEND                        : ▾
..+....1....+....2....+....3....+....4....+....5....+....6....+....7..
 ASSIGNMAT         Mat: BLCKHOLE ▾   Reg: BLKBODY ▾  to Reg: ▾
              Mat(Decay): ▾          Step:            Field: ▾
 ASSIGNMAT         Mat: AIR ▾        Reg: VOID ▾     to Reg: ▾
              Mat(Decay): ▾          Step:            Field: ▾
 ASSIGNMAT         Mat: VACUUM ▾     Reg: Vacuum ▾   to Reg: ▾
              Mat(Decay): ▾          Step:            Field: ▾
 ASSIGNMAT         Mat: TITANIUM ▾   Reg: Window ▾   to Reg: ▾
              Mat(Decay): ▾          Step:            Field: ▾
 ASSIGNMAT         Mat: PMMA ▾       Reg: Cyl1 ▾     to Reg: ▾
              Mat(Decay): ▾          Step:            Field: ▾
 ASSIGNMAT         Mat: PMMA ▾       Reg: Cyl2 ▾     to Reg: ▾
              Mat(Decay): ▾          Step:            Field: ▾
 ASSIGNMAT         Mat: PMMA ▾       Reg: CONE2 ▾    to Reg: ▾
              Mat(Decay): ▾          Step:            Field: ▾
 ASSIGNMAT         Mat: PMMA ▾       Reg: Cyl3 ▾     to Reg: ▾
              Mat(Decay): ▾          Step:            Field: ▾
 ASSIGNMAT         Mat: PMMA ▾       Reg: PHANTOM ▾  to Reg: ▾
              Mat(Decay): ▾          Step:            Field: ▾
 EMFCUT           Type: transport ▾
        e-e+ Threshold: Kinetic ▾  e-e+ Ekin: 1e-05         γ: 1E-05
                  Reg: ▾              to Reg: ▾            Step:

 Set the random number seed
 RANDOMIZE          Unit: 01 ▾         Seed:
 Set the number of primary histories to be simulated in the run
 START              No.: 10000000      Core: ▾
                   Time:               Report: default ▾
 USRBIN                                 Unit: 49 BIN ▾    Name: DDP
       Type: X-Y-Z ▾    Xmin: -20       Xmax: 20             NX: 201
       Part: DOSE ▾     Ymin: -20       Ymax: 20             NY: 201
                        Zmin: 0         Zmax: 100            NZ: 400
 USRBIN                                 Unit: 50 BIN ▾    Name: Dose1
       Type: X-Y-Z ▾    Xmin: -20       Xmax: 20             NX: 201
       Part: DOSE ▾     Ymin: -20       Ymax: 20             NY: 201
                        Zmin: 60        Zmax: 100            NZ: 400
 USRBIN                                 Unit: 51 BIN ▾    Name: Dose2
       Type: X-Y-Z ▾    Xmin: -20       Xmax: 20             NX: 201
       Part: DOSE ▾     Ymin: -20       Ymax: 20             NY: 201
                        Zmin: 60        Zmax: 80             NZ: 200
 STOP
```

Output file of Fluka for the 7 MeV electron beam and the A-1 applicator, inside the PMMA phantom.

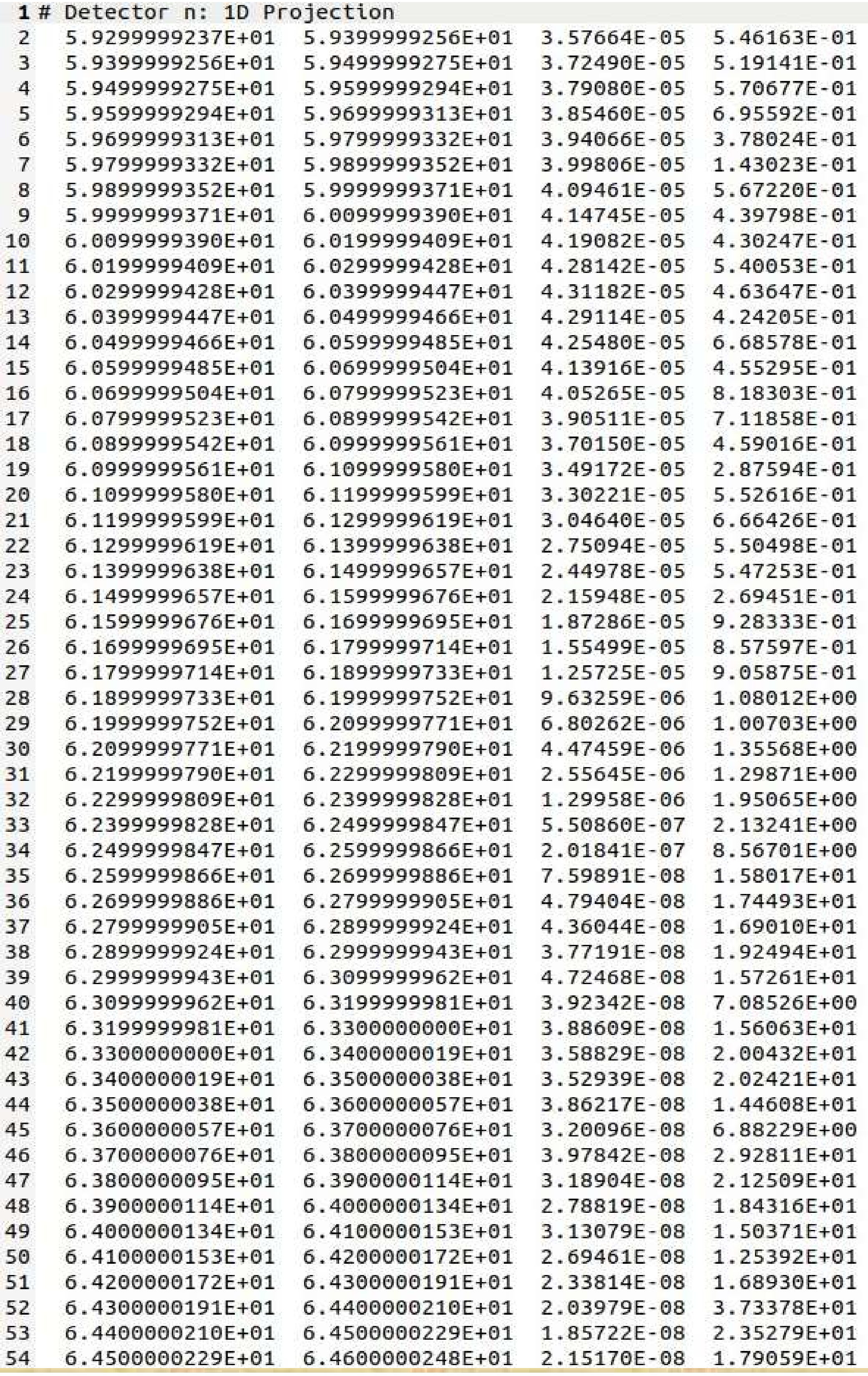

```
# Detector n: 1D Projection
  5.9299999237E+01  5.9399999256E+01  3.57664E-05  5.46163E-01
  5.9399999256E+01  5.9499999275E+01  3.72490E-05  5.19141E-01
  5.9499999275E+01  5.9599999294E+01  3.79080E-05  5.70677E-01
  5.9599999294E+01  5.9699999313E+01  3.85460E-05  6.95592E-01
  5.9699999313E+01  5.9799999332E+01  3.94066E-05  3.78024E-01
  5.9799999332E+01  5.9899999352E+01  3.99806E-05  1.43023E-01
  5.9899999352E+01  5.9999999371E+01  4.09461E-05  5.67220E-01
  5.9999999371E+01  6.0099999390E+01  4.14745E-05  4.39798E-01
  6.0099999390E+01  6.0199999409E+01  4.19082E-05  4.30247E-01
  6.0199999409E+01  6.0299999428E+01  4.28142E-05  5.40053E-01
  6.0299999428E+01  6.0399999447E+01  4.31182E-05  4.63647E-01
  6.0399999447E+01  6.0499999466E+01  4.29114E-05  4.24205E-01
  6.0499999466E+01  6.0599999485E+01  4.25480E-05  6.68578E-01
  6.0599999485E+01  6.0699999504E+01  4.13916E-05  4.55295E-01
  6.0699999504E+01  6.0799999523E+01  4.05265E-05  8.18303E-01
  6.0799999523E+01  6.0899999542E+01  3.90511E-05  7.11858E-01
  6.0899999542E+01  6.0999999561E+01  3.70150E-05  4.59016E-01
  6.0999999561E+01  6.1099999580E+01  3.49172E-05  2.87594E-01
  6.1099999580E+01  6.1199999599E+01  3.30221E-05  5.52616E-01
  6.1199999599E+01  6.1299999619E+01  3.04640E-05  6.66426E-01
  6.1299999619E+01  6.1399999638E+01  2.75094E-05  5.50498E-01
  6.1399999638E+01  6.1499999657E+01  2.44978E-05  5.47253E-01
  6.1499999657E+01  6.1599999676E+01  2.15948E-05  2.69451E-01
  6.1599999676E+01  6.1699999695E+01  1.87286E-05  9.28333E-01
  6.1699999695E+01  6.1799999714E+01  1.55499E-05  8.57597E-01
  6.1799999714E+01  6.1899999733E+01  1.25725E-05  9.05875E-01
  6.1899999733E+01  6.1999999752E+01  9.63259E-06  1.08012E+00
  6.1999999752E+01  6.2099999771E+01  6.80262E-06  1.00703E+00
  6.2099999771E+01  6.2199999790E+01  4.47459E-06  1.35568E+00
  6.2199999790E+01  6.2299999809E+01  2.55645E-06  1.29871E+00
  6.2299999809E+01  6.2399999828E+01  1.29958E-06  1.95065E+00
  6.2399999828E+01  6.2499999847E+01  5.50860E-07  2.13241E+00
  6.2499999847E+01  6.2599999866E+01  2.01841E-07  8.56701E+00
  6.2599999866E+01  6.2699999886E+01  7.59891E-08  1.58017E+01
  6.2699999886E+01  6.2799999905E+01  4.79404E-08  1.74493E+01
  6.2799999905E+01  6.2899999924E+01  4.36044E-08  1.69010E+01
  6.2899999924E+01  6.2999999943E+01  3.77191E-08  1.92494E+01
  6.2999999943E+01  6.3099999962E+01  4.72468E-08  1.57261E+01
  6.3099999962E+01  6.3199999981E+01  3.92342E-08  7.08526E+00
  6.3199999981E+01  6.3300000000E+01  3.88609E-08  1.56063E+01
  6.3300000000E+01  6.3400000019E+01  3.58829E-08  2.00432E+01
  6.3400000019E+01  6.3500000038E+01  3.52939E-08  2.02421E+01
  6.3500000038E+01  6.3600000057E+01  3.86217E-08  1.44608E+01
  6.3600000057E+01  6.3700000076E+01  3.20096E-08  6.88229E+00
  6.3700000076E+01  6.3800000095E+01  3.97842E-08  2.92811E+01
  6.3800000095E+01  6.3900000114E+01  3.18904E-08  2.12509E+01
  6.3900000114E+01  6.4000000134E+01  2.78819E-08  1.84316E+01
  6.4000000134E+01  6.4100000153E+01  3.13079E-08  1.50371E+01
  6.4100000153E+01  6.4200000172E+01  2.69461E-08  1.25392E+01
  6.4200000172E+01  6.4300000191E+01  2.33814E-08  1.68930E+01
  6.4300000191E+01  6.4400000210E+01  2.03979E-08  3.73378E+01
  6.4400000210E+01  6.4500000229E+01  1.85722E-08  2.35279E+01
  6.4500000229E+01  6.4600000248E+01  2.15170E-08  1.79059E+01
```

```
6.4600000248E+01  6.4700000267E+01  1.98050E-08  1.51666E+01
6.4700000267E+01  6.4800000286E+01  2.51413E-08  1.93145E+01
6.4800000286E+01  6.4900000305E+01  2.57473E-08  3.58431E+01
6.4900000305E+01  6.5000000324E+01  2.44578E-08  1.28667E+01
6.5000000324E+01  6.5100000343E+01  2.93769E-08  2.01025E+01
6.5100000343E+01  6.5200000362E+01  2.14662E-08  2.55888E+01
6.5200000362E+01  6.5300000381E+01  1.77465E-08  2.51240E+01
6.5300000381E+01  6.5400000401E+01  2.12095E-08  3.61282E+01
6.5400000401E+01  6.5500000420E+01  1.96515E-08  2.16150E+01
6.5500000420E+01  6.5600000439E+01  2.34841E-08  1.83349E+01
6.5600000439E+01  6.5700000458E+01  2.52809E-08  2.60638E+01
6.5700000458E+01  6.5800000477E+01  2.48050E-08  1.82561E+01
6.5800000477E+01  6.5900000496E+01  1.92487E-08  2.35873E+01
6.5900000496E+01  6.6000000515E+01  1.61950E-08  4.95525E+01
6.6000000515E+01  6.6100000534E+01  1.77707E-08  2.75798E+01
6.6100000534E+01  6.6200000553E+01  9.68805E-09  2.17691E+01
6.6200000553E+01  6.6300000572E+01  1.55722E-08  1.17624E+01
6.6300000572E+01  6.6400000591E+01  1.26021E-08  1.53768E+01
6.6400000591E+01  6.6500000610E+01  2.17627E-08  1.20006E+01
6.6500000610E+01  6.6600000629E+01  2.04208E-08  1.42104E+01
6.6600000629E+01  6.6700000648E+01  1.98031E-08  1.73008E+01
6.6700000648E+01  6.6800000668E+01  1.64601E-08  3.95200E+01
6.6800000668E+01  6.6900000687E+01  2.12046E-08  3.42086E+01
6.6900000687E+01  6.7000000706E+01  1.78971E-08  4.01319E+01
6.7000000706E+01  6.7100000725E+01  1.87573E-08  2.71952E+01
6.7100000725E+01  6.7200000744E+01  9.99467E-09  2.07788E+01
6.7200000744E+01  6.7300000763E+01  1.92506E-08  3.39947E+01
6.7300000763E+01  6.7400000782E+01  1.30124E-08  1.39318E+01
6.7400000782E+01  6.7500000801E+01  1.36493E-08  1.48185E+01
6.7500000801E+01  6.7600000820E+01  1.43400E-08  2.25938E+01
6.7600000820E+01  6.7700000839E+01  1.79465E-08  1.19008E+01
6.7700000839E+01  6.7800000858E+01  9.30270E-09  5.44593E+01
6.7800000858E+01  6.7900000877E+01  1.27912E-08  3.28228E+01
6.7900000877E+01  6.8000000896E+01  1.51116E-08  2.22575E+01
6.8000000896E+01  6.8100000916E+01  1.28976E-08  3.10403E+01
6.8100000916E+01  6.8200000935E+01  7.74107E-09  2.76709E+01
6.8200000935E+01  6.8300000954E+01  8.91612E-09  2.80005E+01
6.8300000954E+01  6.8400000973E+01  9.64474E-09  3.65788E+01
6.8400000973E+01  6.8500000992E+01  4.65065E-09  3.60624E+01
6.8500000992E+01  6.8600001011E+01  1.19012E-08  3.29984E+01
6.8600001011E+01  6.8700001030E+01  1.64106E-08  3.69019E+01
6.8700001030E+01  6.8800001049E+01  1.04959E-08  5.42068E+01
6.8800001049E+01  6.8900001068E+01  1.16518E-08  1.70907E+01
6.8900001068E+01  6.9000001087E+01  8.20874E-09  2.04913E+01
6.9000001087E+01  6.9100001106E+01  7.90007E-09  3.74714E+01
6.9100001106E+01  6.9200001125E+01  8.27296E-09  3.25808E+01
6.9200001125E+01  6.9300001144E+01  2.04311E-08  1.99103E+01
6.9300001144E+01  6.9400001163E+01  1.67126E-08  1.83020E+01
6.9400001163E+01  6.9500001183E+01  1.47428E-08  3.18071E+01
```

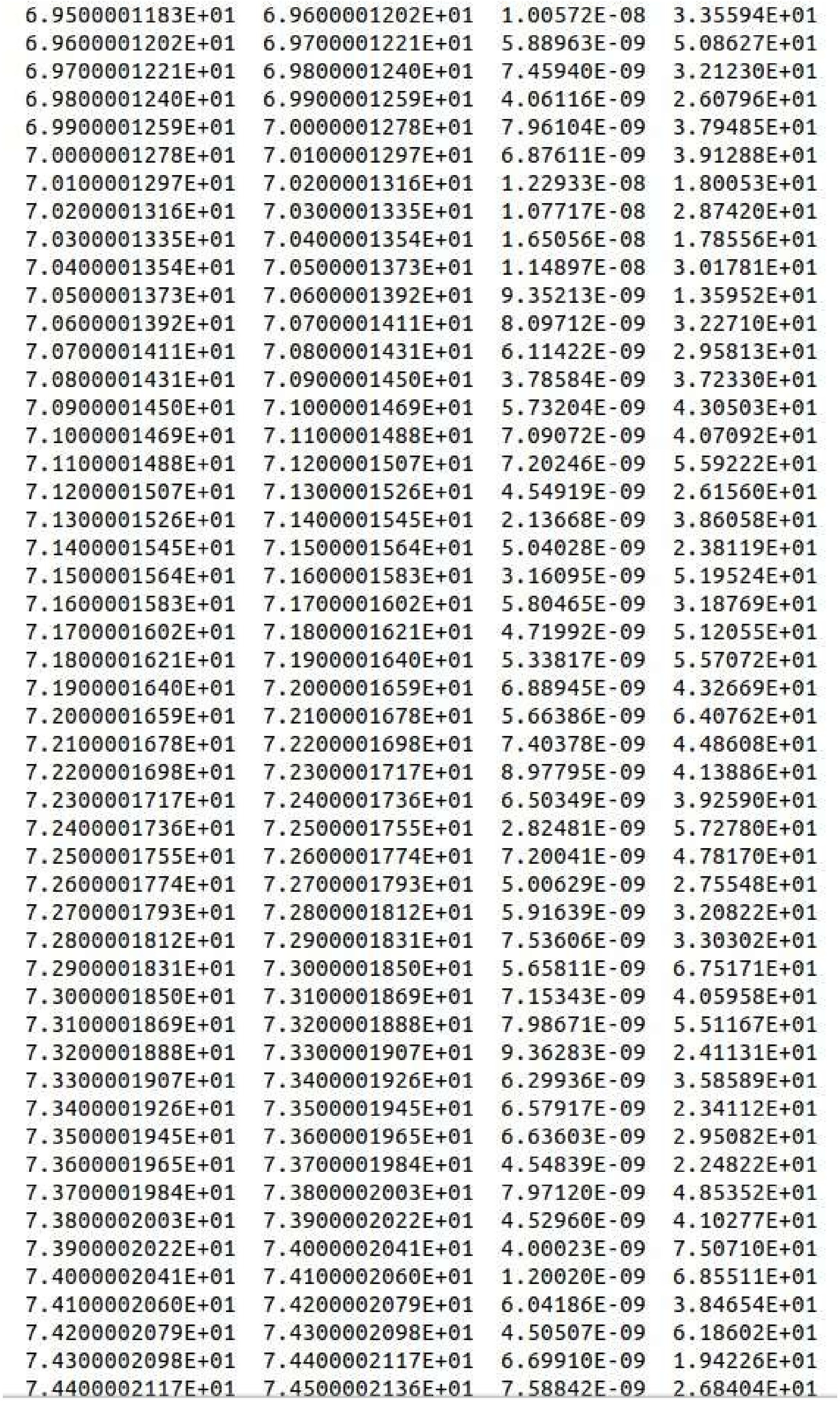

```
6.9500001183E+01  6.9600001202E+01  1.00572E-08  3.35594E+01
6.9600001202E+01  6.9700001221E+01  5.88963E-09  5.08627E+01
6.9700001221E+01  6.9800001240E+01  7.45940E-09  3.21230E+01
6.9800001240E+01  6.9900001259E+01  4.06116E-09  2.60796E+01
6.9900001259E+01  7.0000001278E+01  7.96104E-09  3.79485E+01
7.0000001278E+01  7.0100001297E+01  6.87611E-09  3.91288E+01
7.0100001297E+01  7.0200001316E+01  1.22933E-08  1.80053E+01
7.0200001316E+01  7.0300001335E+01  1.07717E-08  2.87420E+01
7.0300001335E+01  7.0400001354E+01  1.65056E-08  1.78556E+01
7.0400001354E+01  7.0500001373E+01  1.14897E-08  3.01781E+01
7.0500001373E+01  7.0600001392E+01  9.35213E-09  1.35952E+01
7.0600001392E+01  7.0700001411E+01  8.09712E-09  3.22710E+01
7.0700001411E+01  7.0800001431E+01  6.11422E-09  2.95813E+01
7.0800001431E+01  7.0900001450E+01  3.78584E-09  3.72330E+01
7.0900001450E+01  7.1000001469E+01  5.73204E-09  4.30503E+01
7.1000001469E+01  7.1100001488E+01  7.09072E-09  4.07092E+01
7.1100001488E+01  7.1200001507E+01  7.20246E-09  5.59222E+01
7.1200001507E+01  7.1300001526E+01  4.54919E-09  2.61560E+01
7.1300001526E+01  7.1400001545E+01  2.13668E-09  3.86058E+01
7.1400001545E+01  7.1500001564E+01  5.04028E-09  2.38119E+01
7.1500001564E+01  7.1600001583E+01  3.16095E-09  5.19524E+01
7.1600001583E+01  7.1700001602E+01  5.80465E-09  3.18769E+01
7.1700001602E+01  7.1800001621E+01  4.71992E-09  5.12055E+01
7.1800001621E+01  7.1900001640E+01  5.33817E-09  5.57072E+01
7.1900001640E+01  7.2000001659E+01  6.88945E-09  4.32669E+01
7.2000001659E+01  7.2100001678E+01  5.66386E-09  6.40762E+01
7.2100001678E+01  7.2200001698E+01  7.40378E-09  4.48608E+01
7.2200001698E+01  7.2300001717E+01  8.97795E-09  4.13886E+01
7.2300001717E+01  7.2400001736E+01  6.50349E-09  3.92590E+01
7.2400001736E+01  7.2500001755E+01  2.82481E-09  5.72780E+01
7.2500001755E+01  7.2600001774E+01  7.20041E-09  4.78170E+01
7.2600001774E+01  7.2700001793E+01  5.00629E-09  2.75548E+01
7.2700001793E+01  7.2800001812E+01  5.91639E-09  3.20822E+01
7.2800001812E+01  7.2900001831E+01  7.53606E-09  3.30302E+01
7.2900001831E+01  7.3000001850E+01  5.65811E-09  6.75171E+01
7.3000001850E+01  7.3100001869E+01  7.15343E-09  4.05958E+01
7.3100001869E+01  7.3200001888E+01  7.98671E-09  5.51167E+01
7.3200001888E+01  7.3300001907E+01  9.36283E-09  2.41131E+01
7.3300001907E+01  7.3400001926E+01  6.29936E-09  3.58589E+01
7.3400001926E+01  7.3500001945E+01  6.57917E-09  2.34112E+01
7.3500001945E+01  7.3600001965E+01  6.63603E-09  2.95082E+01
7.3600001965E+01  7.3700001984E+01  4.54839E-09  2.24822E+01
7.3700001984E+01  7.3800002003E+01  7.97120E-09  4.85352E+01
7.3800002003E+01  7.3900002022E+01  4.52960E-09  4.10277E+01
7.3900002022E+01  7.4000002041E+01  4.00023E-09  7.50710E+01
7.4000002041E+01  7.4100002060E+01  1.20020E-09  6.85511E+01
7.4100002060E+01  7.4200002079E+01  6.04186E-09  3.84654E+01
7.4200002079E+01  7.4300002098E+01  4.50507E-09  6.18602E+01
7.4300002098E+01  7.4400002117E+01  6.69910E-09  1.94226E+01
7.4400002117E+01  7.4500002136E+01  7.58842E-09  2.68404E+01
```

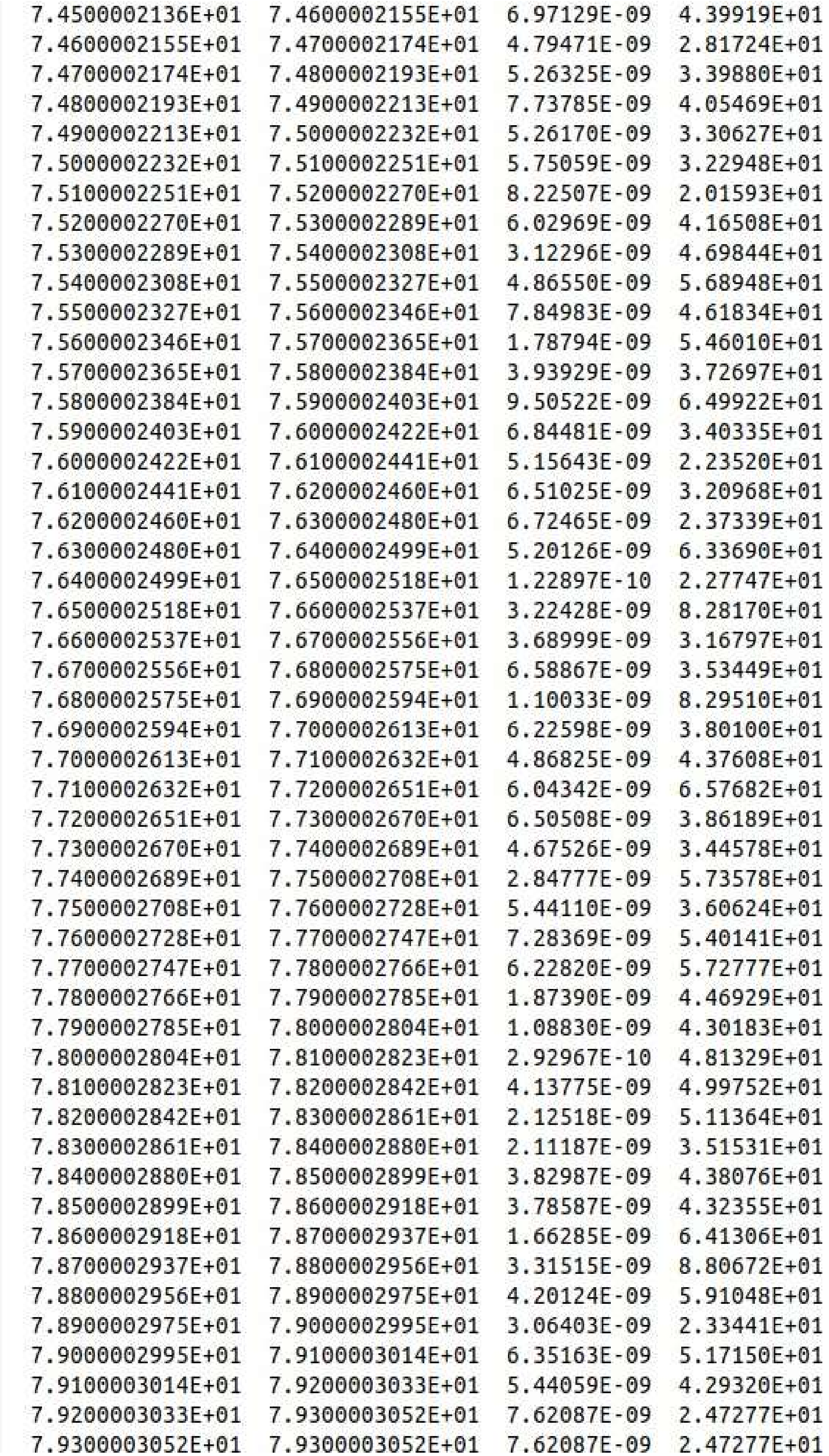

```
7.4500002136E+01  7.4600002155E+01  6.97129E-09  4.39919E+01
7.4600002155E+01  7.4700002174E+01  4.79471E-09  2.81724E+01
7.4700002174E+01  7.4800002193E+01  5.26325E-09  3.39880E+01
7.4800002193E+01  7.4900002213E+01  7.73785E-09  4.05469E+01
7.4900002213E+01  7.5000002232E+01  5.26170E-09  3.30627E+01
7.5000002232E+01  7.5100002251E+01  5.75059E-09  3.22948E+01
7.5100002251E+01  7.5200002270E+01  8.22507E-09  2.01593E+01
7.5200002270E+01  7.5300002289E+01  6.02969E-09  4.16508E+01
7.5300002289E+01  7.5400002308E+01  3.12296E-09  4.69844E+01
7.5400002308E+01  7.5500002327E+01  4.86550E-09  5.68948E+01
7.5500002327E+01  7.5600002346E+01  7.84983E-09  4.61834E+01
7.5600002346E+01  7.5700002365E+01  1.78794E-09  5.46010E+01
7.5700002365E+01  7.5800002384E+01  3.93929E-09  3.72697E+01
7.5800002384E+01  7.5900002403E+01  9.50522E-09  6.49922E+01
7.5900002403E+01  7.6000002422E+01  6.84481E-09  3.40335E+01
7.6000002422E+01  7.6100002441E+01  5.15643E-09  2.23520E+01
7.6100002441E+01  7.6200002460E+01  6.51025E-09  3.20968E+01
7.6200002460E+01  7.6300002480E+01  6.72465E-09  2.37339E+01
7.6300002480E+01  7.6400002499E+01  5.20126E-09  6.33690E+01
7.6400002499E+01  7.6500002518E+01  1.22897E-10  2.27747E+01
7.6500002518E+01  7.6600002537E+01  3.22428E-09  8.28170E+01
7.6600002537E+01  7.6700002556E+01  3.68999E-09  3.16797E+01
7.6700002556E+01  7.6800002575E+01  6.58867E-09  3.53449E+01
7.6800002575E+01  7.6900002594E+01  1.10033E-09  8.29510E+01
7.6900002594E+01  7.7000002613E+01  6.22598E-09  3.80100E+01
7.7000002613E+01  7.7100002632E+01  4.86825E-09  4.37608E+01
7.7100002632E+01  7.7200002651E+01  6.04342E-09  6.57682E+01
7.7200002651E+01  7.7300002670E+01  6.50508E-09  3.86189E+01
7.7300002670E+01  7.7400002689E+01  4.67526E-09  3.44578E+01
7.7400002689E+01  7.7500002708E+01  2.84777E-09  5.73578E+01
7.7500002708E+01  7.7600002728E+01  5.44110E-09  3.60624E+01
7.7600002728E+01  7.7700002747E+01  7.28369E-09  5.40141E+01
7.7700002747E+01  7.7800002766E+01  6.22820E-09  5.72777E+01
7.7800002766E+01  7.7900002785E+01  1.87390E-09  4.46929E+01
7.7900002785E+01  7.8000002804E+01  1.08830E-09  4.30183E+01
7.8000002804E+01  7.8100002823E+01  2.92967E-10  4.81329E+01
7.8100002823E+01  7.8200002842E+01  4.13775E-09  4.99752E+01
7.8200002842E+01  7.8300002861E+01  2.12518E-09  5.11364E+01
7.8300002861E+01  7.8400002880E+01  2.11187E-09  3.51531E+01
7.8400002880E+01  7.8500002899E+01  3.82987E-09  4.38076E+01
7.8500002899E+01  7.8600002918E+01  3.78587E-09  4.32355E+01
7.8600002918E+01  7.8700002937E+01  1.66285E-09  6.41306E+01
7.8700002937E+01  7.8800002956E+01  3.31515E-09  8.80672E+01
7.8800002956E+01  7.8900002975E+01  4.20124E-09  5.91048E+01
7.8900002975E+01  7.9000002995E+01  3.06403E-09  2.33441E+01
7.9000002995E+01  7.9100003014E+01  6.35163E-09  5.17150E+01
7.9100003014E+01  7.9200003033E+01  5.44059E-09  4.29320E+01
7.9200003033E+01  7.9300003052E+01  7.62087E-09  2.47277E+01
7.9300003052E+01  7.9300003052E+01  7.62087E-09  2.47277E+01
```